Measurements of atmospheric CO_2 columns using ground-based FTIR spectra

Zur Erlangung des akademischen Grades eines
DOKTORS DER NATURWISSENSCHAFTEN
Fakultät für Chemie und Biowissenschaften
Karlsruher Institut für Technologie (KIT) - Universitätsbereich

genehmigte

DISSERTATION

von

Susanne Dohe

aus Lengerich (Westf.)

Dekan:	Prof. Dr. P. Roesky
Referent:	Prof. Dr. M. Olzmann
Korreferent:	Prof. Dr. J. Orphal
Tag der mündlichen Prüfung:	20.12.2013

Summary

The investigation of carbon dioxide (CO_2) sources and sinks within the carbon cycle is important in order to understand global climate change. For this task, CO_2 total column amounts determined from ground-based Fourier transform infrared (FTIR) measurements turned out to be well suited. In order to achieve the desired CO_2 total column accuracy of 0.1% which is required to investigate CO_2 sources and sinks, the detection of error sources and their reduction is necessary. In this thesis, which was created at the Institute of Meteorology and Climate Research (IMK), required measures for the reduction of error sources and the improvement of total column accuracies are presented.

A main part is the correction of errors in the interferogram sampling, which induce significant biases in historic retrievals recorded before an exchange of the laser board (2010/2011). A two step scheme is presented, where the laser sampling error is first estimated and in the second step used to correct the whole interferogram. Measurements acquired at Izaña (Canary Islands, Spain) were used to demonstrate the method, where sampling errors of up to 0.5% were determined and reduced to 0.2% after resampling the interferogram. Remaining discrepancies could be attributed to additional changes in interferometer alignment. In the future the proposed method, which has been published in Dohe et al. [2013], will be applied to historic spectra at all sites of the Total Carbon Column Observing Network (TCCON).

In order to ensure the high quality of the retrieved data, X_{CO_2} (X_Y: column-averaged dry air mole fraction of the target gas Y) retrieval results from the IMK-related sites Izaña and Karlsruhe are compared with co-located in situ measurements. The TCCON calibration factor of 0.989 for X_{CO_2} was verified and slight differences in the annual cycle's amplitude can be attributed to the different measurement techniques. In addition, common periods with unusually large X_{CO_2} values were detected for in situ and FTIR measurements at Karlsruhe. A comparison between X_{CO_2} time series of different nearby TCCON sites shows a good agreement, but also indicates slight discrepancies in the annual cycle due to differences in the site's altitudes. In addition, events with unusually high X_{CO_2} values appear at all sites and have to be investigated further.

As high total column accuracies of X_{CO_2} are essential for the use in carbon cycle science or the validation of satellites, the analysis procedure of PROFFIT, a software

for the determination of trace gases out of solar spectra (developed at IMK), was improved. New features like line mixing (LM) or collision induced absorption (CIA) were implemented and an improvement of the solar line list was performed. In addition, the modification of CO_2 air-broadening widths led to an elimination of airmass dependent effects. By means of these changes, the accuracy of 0.05–0.12% for measurements at Karlsruhe was improved by up to 50%.

The impact of several error sources within the retrieval was determined by comparing PROFFIT results with data of the standard TCCON software GFIT. Modifications of the PROFFIT retrieval setup led to a reduction of the bias between PROFFIT and GFIT X_{CO_2} values from 0.42% to 0.03%. These results indicate the successful cross-validation of the two codes, where the use of PROFFIT represents an alternative for the analysis of ground-based FTIR spectra within the TCCON. The intercomparison reveals shortcomings of the GFIT software as well. Airmass dependent effects occur only in GFIT retrievals and are most likely due to the lack of an extended baseline fit in GFIT and the different implementation of CIA. This error needs to be corrected at its source in order to ensure the high quality standard.

Due to the fact that standard TCCON retrievals only provide total column amounts of CO_2, a novel analysis procedure to retrieve vertical CO_2 profiles from TCCON measurements is presented. A comparison between retrieved CO_2 ground values and in situ measurements acquired at Izaña shows a good agreement, where an in situ calibration factor of 1.022 was determined. This factor was verified by the validation of retrieval results with aircraft measurements from Lamont. For all days with a sufficient number of measurements, profile retrieval results and aircraft measurements are in a good agreement. Performed sensitivity studies show that detected unrealistically intraday variabilities of CO_2 profiles are most probably caused by intraday variations of the ground pressure and the temperature profiles. Therefore an extended retrieval strategy has to be set up which might solve this problem. Due to the larger information content compared to total column results, the implementation of the retrieved profiles in models for the investigation of the carbon cycle would be a great advance. In addition, these profiles can also be used as a priori profiles within the standard TCCON analysis, leading to improved total column accuracies.

Zusammenfassung

Die Erforschung der Quellen und Senken von Kohlenstoffdioxid (CO_2) im Kohlenstoffkreislauf ist dringend notwendig um die Ursachen und Folgen des globalen Klimawandels abschätzen zu können. Hierzu sind bodengebundene Fourier-Transformations-Infrarot (FTIR) Gesamtsäulenmessungen besonders geeignet. Um die notwendige Gesamtsäulengenauigkeit von 0.1% zur Bestimmung der Quellen und Senken von CO_2 erreichen zu können, ist die Charakterisierung von Fehlerquellen und deren Korrektur dringend erforderlich. In dieser Arbeit, die am Institut für Meteorologie und Klimaforschung (IMK) durchgeführt wurde, werden notwendige Maßnahmen zur Minimierung von Fehlerquellen und zur Verbesserung der CO_2-Gesamtsäulengenauigkeit vorgestellt.

Ein wesentlicher Teil ist dabei die Korrektur von Samplingfehlern im Interferogramm, die bei der Auswertung von FTIR Messungen zu inkorrekten Ergebnissen führen können. Hierbei sind hauptsächlich Interferogramme betroffen, die vor einem Austausch des Laserboards (2010/2011) aufgenommen wurden. Im Rahmen dieser Arbeit wird eine Methode beschrieben, bei der im ersten Schritt die Quantifizierung des Samplingfehlers erfolgt und daraufhin der bestimmte Fehler im zweiten Schritt zur Korrektur des gesamten Interferograms herangezogen wird. Zum Testen dieser Methode wurden Spektren vom Standort Izaña (Kanarische Inseln, Spanien) herangezogen, wobei Samplingfehler in der Größenordnung von bis zu 0.5% mit Hilfe der in dieser Arbeit vorgeschlagenen Korrektur auf etwa 0.2% reduziert werden konnten. Die verbleibende Abweichung wird vermutlich durch die im Anschluss an den Laserboardaustausch stattgefundene Neujustage des Interferometers hervorgerufen. In Zukunft sollen die fehlerbehafteten Spektren aller Stationen des Total Carbon Column Observing Networks (TCCON) mit der hier vorgestellten und in Dohe et al. [2013] veröffentlichten Methode korrigiert werden.

Um die hohe Qualität der ausgewerteten Daten sicherzustellen, werden die X_{CO_2}-Ergebnisse (X_Y: Säulen gemitteltes molares Mischungsverhältnis des Gases Y in trockener Luft) der IMK Stationen Karlsruhe und Izaña mit in situ Messungen an benachbarten Stationen verglichen. Der TCCON Kalibrierungsfaktor von 0.989 für X_{CO_2} konnte an beiden Stationen verifiziert werden, wobei geringe Unterschiede in der Amplitude des Jahresgangs durch die unterschiedlichen Messtechniken hervorgerufen werden.

Zusätzlich gibt es Perioden in denen sowohl in situ Messungen der Station Schauninsland als auch FTIR Messungen am Standort Karlsuhe erhöhte X_{CO_2}-Werte aufweisen. Der Vergleich der X_{CO_2}-Zeitreihe für Karlsruhe mit Werten von benachbarten TCCON Stationen, zeigt eine gute Übereinstimmung. Geringe Unterschiede im Jahresgang können auf die verschiedenen Höhenlagen der Stationen zurückgeführt werden. Für alle am Vergleich teilnehmenden Standorte sind außerdem Perioden mit ungewöhnlich hohen X_{CO_2}-Werten zu erkennen, deren Ursache anhand von Rückwärtstrajektorien untersucht werden muss.
Da eine hohe Genauigkeit der CO_2-Gesamtsäulen für die Erforschung des Kohlenstoffkreislaufs und die Validierung von Satellitendaten dringend erforderlich ist, wurden Verbesserungen an dem zur Auswertung von Spektren herangezogenen Programm PROFFIT (entwickelt am IMK) vorgenommen. Hierbei wurden sowohl die solaren Liniendaten optimiert als auch neue Funktionen wie line mixing (LM) oder collision induced absorption (CIA) implementiert. Des Weiteren führte die Modifizierung der CO_2-Luftverbreiterungsparameter zu einer Minimierung der Luftmassenabhängigkeiten in der CO_2-Gesamtsäule. Insgesamt konnte die X_{CO_2}-Gesamtsäulengenauigkeit für Messungen in Karlsruhe (0.05–0.12%) anhand der genannten Änderungen um bis zu 50% gesteigert werden.
Zusätzlich konnte durch die Kreuzvalidierung von PROFFIT mit der TCCON Standardsoftware GFIT der Einfluss verschiedener Fehlerquellen innerhalb der Auswertung analysiert werden. Änderungen in der PROFFIT Auswerteroutine führten hierbei zu einer Reduzierung des Unterschieds zwischen PROFFIT und GFIT X_{CO_2}-Ergebnissen von 0.46% auf 0.03%. Die vorgestellten Resultate bestätigen die erfolgreiche Kreuzvalidierung der beiden Codes und erlauben den Schluss, dass PROFFIT eine Alternative für die Auswertung bodengebundener FTIR Spektren innerhalb des TCCON darstellt. Des Weiteren deckte der Vergleich auch Mängel innerhalb der GFIT Software auf. Im Gegensatz zu den mit PROFFIT bestimmten CO_2-Gesamtsäulen, zeigen die mit GFIT ausgewerteten Ergebnisse eine deutliche Luftmassenabhängigkeit, die höchstwahrscheinlich durch die unterschiedliche Implementierung von CIA und/oder das Fehlen eines erweiterten Baseline Fits hervorgerufen wird. Eine Korrektur dieses Effekts ist dringend notwendig, um die innerhalb des TCCON angestrebte Gesamtsäulengenauigkeit von 0.1% erreichen zu können.
Da die TCCON Standardauswertung nur Gesamtsäulen von CO_2 liefert, die keine Informationen über die vertikale Verteilung des Gases enthalten, wird in dieser Arbeit eine Auswertungsstrategie vorgestellt, mit der zusätzlich vertikale CO_2-Profile bestimmt werden können. Ein Vergleich zwischen den aus dem Profil erhaltenen Bodenwerten

und in Izaña durchgeführten in situ Messungen zeigt eine sehr gute Übereinstimmung, wobei ein in situ Kalibrierungsfaktor von 1.022 bestimmt werden konnte. Dieser Faktor konnte durch die Validierung der CO_2-Profilergebnisse mit Flugzeugmessungen über Lamont bestätigt werden. Dabei wurde für alle Tage mit einer ausreichenden Anzahl an TCCON Messungen eine sehr gute Vergleichbarkeit gezeigt. Durchgeführte Sensitivitätsstudien deuten darauf hin, dass die detektierte unrealistisch hohe Variabilität der CO_2-Profile innerhalb eines Tages durch Variationen des Bodendrucks und Änderungen im Temperaturprofil hervorgerufen wird. Um dieses Problem zu lösen, muss eine verbesserte Auswertungsstrategie aufgesetzt werden, in der die genannten Einflüsse berücksichtigt werden. Aufgrund des erhöhten Informationsgehalts der erhaltenen CO_2-Profile gegenüber Gesamtsäulenmessungen wäre deren Einbindung in Modelle zur Untersuchung des Kohlenstoffkreislaufs ein großer Fortschritt. Zusätzlich könnten die gewonnen Profile als a priori-Profile in der TCCON Standardauswertung verwendet werden, was zu einer Verbesserung der Gesamtsäulengenauigkeit führen würde.

Contents

Contents **ix**

Introduction **1**

1 The Earth's atmosphere **3**

1.1 Composition and structure of the atmosphere 3

1.2 The carbon cycle 5

1.2.1 The slow carbon cycle 6

1.2.2 The fast carbon cycle 7

1.2.3 Changes in the carbon cycle 8

1.3 The greenhouse effect 10

1.3.1 The anthropogenic greenhouse effect 13

1.3.2 Greenhouse gases 13

2 Remote sensing in the infrared region **17**

2.1 IR absorption spectroscopy 17

2.1.1 Diatomic molecules 18

2.1.2 Polyatomic molecules 22

2.2 Spectral line shapes 24

2.2.1 Doppler broadening 24

2.2.2 Pressure broadening 25

2.2.3 The Voigt function 26

3 FTIR spectroscopy **27**

3.1 The FTIR spectrometer 27

3.2 The Fourier transformation 28

3.3 FTIR networks 32

3.3.1 NDACC - IRWG Network 33

3.3.2 TCCON Network 33

3.4 IMK-related stations . . . 35
3.4.1 Izaña . . . 35
3.4.2 Karlsruhe . . . 35

4 Analysis of ground-based absorption measurements 37
4.1 Inversion theory . . . 37
4.2 Retrieval software . . . 39
4.3 Spectral windows . . . 40
4.3.1 CO_2 . . . 40
4.3.2 O_2 . . . 41
4.4 Error sources . . . 42
4.5 O_2 as an internal network standard . . . 48

5 Correction of sampling ghosts 49
5.1 Instrumentation at Izaña . . . 50
5.2 Empirical ghost correction . . . 51
5.3 Fundamental TCCON ghost correction . . . 54
5.3.1 Quantification of the sampling error . . . 54
5.3.2 Correction of the sampling error . . . 58
5.4 Conclusions . . . 61

6 TCCON X_{CO_2} data 63
6.1 Comparison with in situ data . . . 63
6.1.1 Izaña . . . 64
6.1.2 Karlsruhe . . . 66
6.2 Intercomparison between nearby TCCON sites . . . 68
6.3 Conclusions . . . 69

7 Optimization of the PROFFIT retrieval setup 71
7.1 Air-broadening width . . . 72
7.2 Implementation of line mixing . . . 75
7.3 Baseline fit and collision induced absorption . . . 77
7.4 Reparametrization of partition functions . . . 82
7.5 Implementation of GFIT a priori profiles . . . 84
7.6 Implementation of GFIT pressure-temperature profiles . . . 87
7.7 Improvement of the solar line list . . . 89
7.8 Implementation of the GFIT O_2 line list . . . 91

7.9 Intercomparison between PROFFIT and GFIT 94
7.10 Air mass dependence 96
7.11 Conclusions 98

8 CO_2 profile retrievals from TCCON spectra 101
8.1 PROFFIT profile retrieval setup 102
8.2 Izaña results 104
8.3 Lamont results 108
8.4 Sensitivity studies 110
8.4.1 Instrumental line shape 112
8.4.2 Ground pressure 113
8.4.3 Temperature 114
8.5 Conclusions 115

9 Summary and Outlook 117

References 121

List of Figures 131

List of Tables 141

Nomenclature 143

Acknowledgement

Introduction

In our days, global climate change is one of the most urgent challenges facing mankind, however it is induced by humans themselves. Industrialization and land use change cause a significant modification of the atmospheric composition leading to major implications like the depletion of stratospheric ozone or global warming. The latter one is continuously boosted by increasing greenhouse gas (GHG) concentrations. Due to its increase from 315 ppm in 1958 to 390 ppm in 2010 (Mauna Loa, Dr. P. Tans, NOAA/ESRL[1] and Dr. R. Keeling, Scripps Institution of Oceanography[2]), carbon dioxide (CO_2) is the major contributor to the anthropogenic greenhouse effect [IPCC, 2007].

In order to understand global climate change and to estimate future effects, the investigation of CO_2 sources and sinks within the carbon cycle is strongly required. For this reason, several measurement programs were initialized being mainly in situ measurements, satellite measurements and ground-based Fourier transform infrared (FTIR) measurements. In contrast to in situ measurements, ground-based FTIR spectrometers and satellites detect total column abundances of CO_2. These are most suitable for inverse modeling of CO_2 and the investigation of the carbon cycle, due to their coverage of a larger number of atmospheric levels and their independence of vertical transport [Chevallier et al., 2011] [Keppel-Aleks et al., 2011].

Because of their global coverage, satellites like the Greenhouse gases Observing Satellite (GOSAT, Morino et al. [2011]), the Orbiting Carbon Observatory II (OCO II, Miller et al. [2007]) and the Carbon monitoring Satellite (CarbonSat, Bovensmann et al. [2010]) were developed. While GOSAT was already started in January 2009, OCO II and CarbonSat are planned to be launched within the next few years.

The Total Carbon Column Observing Network (TCCON) is a worldwide network of high-resolution ground-based FTIR spectrometers measuring solar absorption spectra in the near-infrared (NIR) region. The main goal is to provide accurate total column

[1] www.esrl.noaa.gov/gmd/ccgg/trends/
[2] scrippsco2.ucsd.edu/

amounts of atmospheric trace gases for the validation of satellites [Oshchepkov et al., 2013] and the investigation of the carbon cycle [Keppel-Aleks et al., 2011].
Within the TCCON, the Institute of Meteorology and Climate Research (IMK) at the Karlsruhe Institute of Technology (KIT) operates two high-resolution FTIR spectrometers in Karlsruhe (Germany) at KIT Campus North and in Izaña on Tenerife (Canary Islands, Spain) in collaboration with the Meteorological State Agency of Spain (AEMET). The retrieval of CO_2 total column amounts from ground-based FTIR measurements at Izaña and Karlsruhe is the topic of this work.
For the detection of CO_2 sources and sinks within the carbon cycle a high accuracy is required. Following Olsen and Randerson [2004], the determination of a northern hemispheric sink in the order of 1 GtC/year requires a CO_2 total column accuracy of at least 0.1%. However, due to the fact that current studies indicate an accuracy of about 0.25% [Wunch et al., 2011], the identification of error sources and their correction is strongly required, which is the main part of this thesis.
Chapter 1 to 4 comprise the theoretical basis of this work, including an overview about relevant processes in the Earth's atmosphere, an outline about important aspects of remote sensing in the NIR region, an introduction to the subject of Fourier transform spectroscopy and an overview about the analysis of ground-based infrared (IR) spectra.
Chapter 5 deals with an error source of special relevance for FTIR NIR measurements, namely sampling errors in the recorded interferograms, leading to erroneous total column abundances. In order to improve the accuracy, the quantification of this error and its correction is presented.
In Chapter 6 the retrieved CO_2 time series from the IMK-related sites Karlsruhe and Izaña are shown and compared to co-located in situ measurements and data from other nearby TCCON sites in order to check for consistency.
Chapter 7 describes the stepwise optimization of the analysis procedure within the PROFFIT software (developed at IMK, Hase et al. [2004]), in order to minimize fit residuals and achieve the desired accuracy. In addition, the results are cross-validated against data retrieved with the standard TCCON software GFIT (G. C. Toon, Jet Propulsion Laboratory, United States).
In Chapter 8 a new analysis strategy for retrievals of vertical CO_2 profiles is presented, which aims at improving the retrieval information content and optimizing the column sensitivity, leading to more accurate results.
Chapter 9 summarizes the work and gives an outlook on further research topics.

Chapter 1

The Earth's atmosphere

This chapter introduces relevant aspects and processes of the Earth's atmosphere. In the first Section 1.1, the atmospheric composition and structure is described, with the content being mostly adapted from Fabian [2002] and Kraus [2006]. While Section 1.2 outlines the carbon cycle and its anthropogenic changes, the last section is about the greenhouse effect, its enhancement and important greenhouse gases. The contents of Section 1.2 and 1.3 are mainly based on the latest IPCC report [IPCC, 2007], Riebeek [2011], Le Quéré et al. [2012], Tipler [1994] and Seifritz [1991].

1.1 Composition and structure of the atmosphere

The main constituents of the atmosphere, assuming dry air, are oxygen (O_2, 20.95%), nitrogen (N_2, 78.08%) and the inert gas argon (Ar, 0.93%) with combined 99.96%. However, their impact on today's climate system is negligible on the one hand due to their weak interaction with infrared radiation and on the other hand the absorption of N_2 and O_2 in the ultraviolet (UV) region (<242 and 100 nm respectively) is not important for the lower atmosphere. For the Earth's climate system, the so called trace gases with 0.04% of dry air play a major role, especially the greenhouse gases carbon dioxide (CO_2), ozone (O_3), nitrous oxide (N_2O), methane (CH_4) and the halocarbons. Not included in dry air is water (H_2O), being a major greenhouse gas with variable amounts between 0 and 4%. Since the industrial revolution, human activities led to increasing atmospheric concentrations of most GHGs. Concerning the GHG's distribution in the atmosphere, H_2O and O_3 show the largest variability in space and time. While most of the H_2O is located in the lower atmosphere (troposphere), where it is regulated by the watercycle, O_3 is mainly built photochemically in upper levels but also formed by photosmog reactions at the Earth's surface.

The atmospheric pressure decreases exponentially with height. Following an empirical formula, it is halved every 5 km. The atmosphere's structure is specified through the vertical temperature profile, which depends on the absorbed radiation between short wave UV (100 nm) and near-infrared (3500 nm) with maximum energy flux in the visible region (500 nm). A schematic description of the atmospheric temperature profile is given in Figure 1.1. UV radiation with wavelengths of up to 175 nm is absorbed above

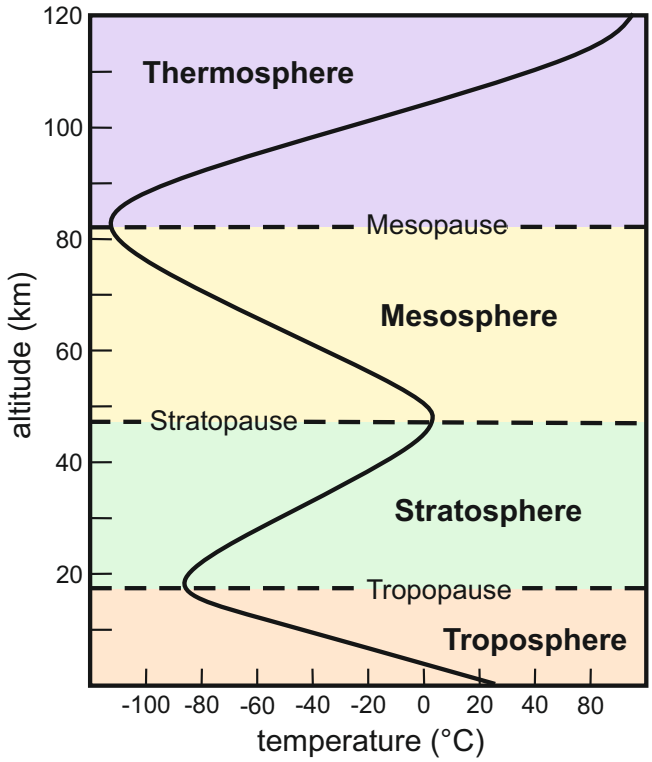

Figure 1.1: The atmosphere can be divided into four parts (troposphere, stratosphere, mesosphere and thermosphere) where the structure is specified through the vertical temperature profile depending on the amount of absorbed radiation (based on Häckel [1999]).

the mesopause (90 km) leading to an ionization and heating of the atmosphere with a temperature rise to 1700 °C at a height of 500 km. This region above the mesopause is called the ionosphere or thermosphere. The remaining UV radiation (175–242 nm) is absorbed in the mesosphere (50–90 km) and the stratosphere (15–50 km) by O_2, which dissociates and builds the ozone layer. The ozone absorbs additional UV radiation (200–340 nm) and also parts of visible light leading to a heating of the stratosphere and mesosphere, where the maximum temperature at the stratopause (50 km) is similar to the Earth's surface temperature. Due to its absorption characteristic, the ozone

layer is a protection from harmful UV radiation.
Concerning the lower atmosphere, the troposphere and the Earth's surface receive the remaining radiation. The long wave part of the radiation (>800 nm) is absorbed by water in the troposphere, while the major part of the radiation (400–800 nm) reaches the surface. As a consequence, it warms up and thereby releases heat to the atmosphere. This is the reason why the temperature decreases with height in the troposphere, with a minimum of -80 °C at the tropopause (10–15 km in temperate zones). The largest part of the Sun's energy discharged at the Earth's surface is used to evaporate water, where the energy is released again by forming clouds. This process is the driving part of the weather.
In the middle atmosphere (stratosphere and mesosphere) many tropospheric gases are photolyzed. While other gases like CO_2, CH_4 or N_2O are able to move through the tropopause, water is freezing out. Although some water is built in the stratosphere by photochemical processes, the produced amount is not sufficient to cause weather phenomena.

1.2 The carbon cycle

Carbon exists in many chemical forms and oxidation states, with the most stable forms on Earth being CO_2 and calcium carbonate ($CaCO_3$). The carbon cycle is the flow of carbon between the natural reservoirs atmosphere, hydrosphere, terrestrial biosphere and lithosphere where processes that release carbon are called sources and processes where carbon is removed are called sinks. If carbon is emitted by one reservoir, another is going to absorb it. A diagram of the carbon cycle is illustrated in Figure 1.2. Natural fluxes between terrestrial biosphere and atmosphere are in the order of 120 GtC/year, exchanges between ocean and atmosphere are about 90 GtC/year and fluxes between land and oceans are relatively small with 1 GtC/year (all values for 1995, IPCC [2007]). For comparison, humans released about 9.3 GtC/year (2002–2011) via fossil fuel burning and land use change into the atmosphere [Le Quéré et al., 2012].
The carbon cycle can be divided into two components: the slow carbon cycle, containing processes with large time scales (millions of years) and the fast carbon cycle containing processes which have usually shorter time scales in the range of days or seasons [Archer et al., 2009].

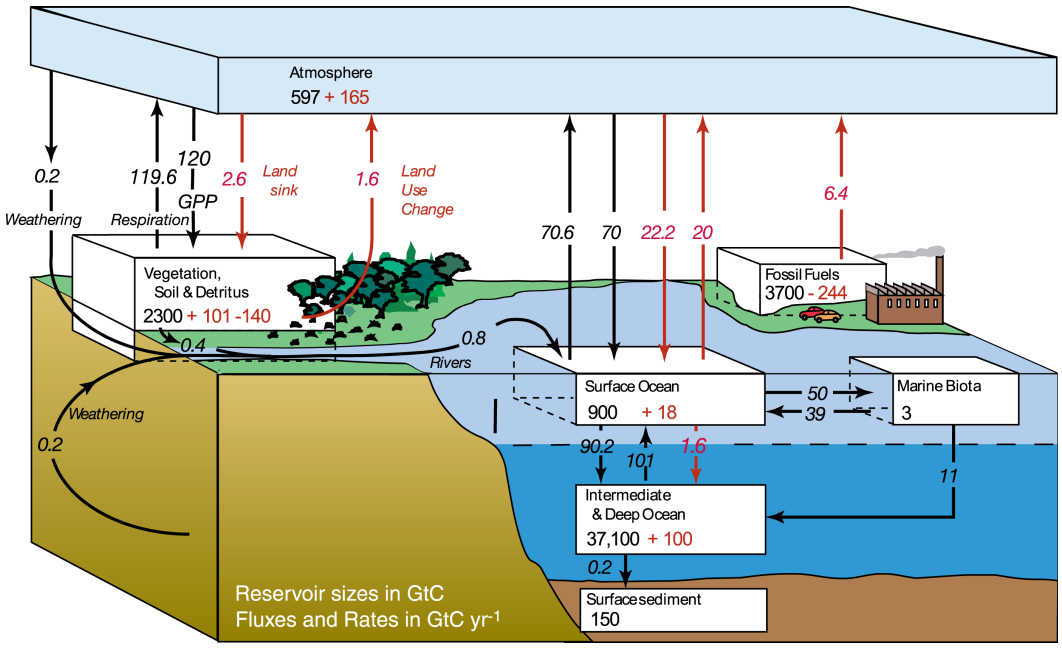

Figure 1.2: A schematic overview of the carbon cycle of the 1990's with main annual fluxes in GtC/year. Pre-industrial fluxes are displayed in black arrows whereas anthropogenic fluxes are shown as red arrows. (Taken from IPCC [2007])

1.2.1 The slow carbon cycle

The exchange of carbon between atmosphere and litosphere starts with rain, where atmospheric carbon combines with water to carbonic acid (H_2CO_3), which reacts and dissolves minerals to their component ions at the Earth's surface via chemical weathering. These ions are carried by rivers into oceans where the calcium ions react with hydrogen carbonate (HCO_3^-) dissolved in water and build calcium carbonate ($CaCO_3$). Most of the ocean's $CaCO_3$ is formed by shell building organisms. If they die, a part of the $CaCO_3$ is deposited along with non calcium containing matter at the ocean's floor and is converted into limestone and fossil fuel, respectively. The whole sea floor is located above moving tectonic plates. If those collide, the sea floor carbon is pushed deeper into the Earth (subduction). Under the extreme heat and pressure the rock melts and CO_2 is released mostly via volcanic eruptions into the atmosphere (0.15–0.26 GtC/year, Gerlach [2011]). In summary the atmosphere's CO_2 concentration is regulated by the balance between the processes weathering, subduction and volcanism, taking many millions of years [Berner, 1998].

In addition, the slow carbon cycle has a slightly faster component, which is the exchange between ocean and atmosphere. In this steady exchange, CO_2 dissolves and

evaporates at the ocean's surface, where the dissolved CO_2 reacts with water to form HCO_3^- and carbonates (CO_3^-), called dissolved inorganic compounds (DIC). Their residence time in surface water is less than a decade [IPCC, 2007], which is also influenced by the exchange between surface and deep ocean water.

1.2.2 The fast carbon cycle

Due to the production of carbohydrates from sunlight and their breakdown to produce energy, plants play a major role in the fast carbon cycle. In the process of photosynthesis, atmospheric CO_2 is absorbed into the plant's cells and combined with sunlight and water to build sugar:

$$6\,CO_2 + 6\,H_2O + \text{energy} \longrightarrow C_6H_{12}O_6 + 6\,O_2\,\cdot \tag{R 1}$$

Concerning the release of carbon back to the atmosphere, four processes are possible: plants burn sugar to get growing energy, animals or humans eat plants to get energy, plants die and decay at the end of a growing season (decomposition) or fire wastes plants. All of these processes lead to the same chemical reaction, called respiration:

$$C_6H_{12}O_6 + 6\,O_2 \longrightarrow 6\,CO_2 + 6\,H_2O + \text{energy}\,\cdot \tag{R 2}$$

In summary the amount of carbon which moves through photosynthesis and respiration per year is about 1000 times larger than the amount of carbon which moves through the slow carbon cycle [IPCC, 2007].
On land, the exchange of carbon with the atmosphere is controlled by the fast carbon cycle in such a way that the growing season of plants can be seen in atmospheric CO_2 fluctuations, which are more pronounced in the northern hemisphere. During a day in the growing season (spring), leaves absorb sunlight and take up CO_2 from the atmosphere. Respiration takes place simultaneously leading to an emission of CO_2. During night photosynthesis stops, whereas respiration continues. This leads to additional intraday fluctuations of CO_2 concentrations between day- and nighttime. In autumn, plants drop their leaves and photosynthesis is no longer possible, while respiration proceeds. As a consequence, CO_2 concentrations increase during winter. The maximum is reached in spring when the plants begin to grow, photosynthesis starts again and CO_2 concentrations decrease until autumn. The annual cycle of CO_2 is illustrated in Figure 1.3.

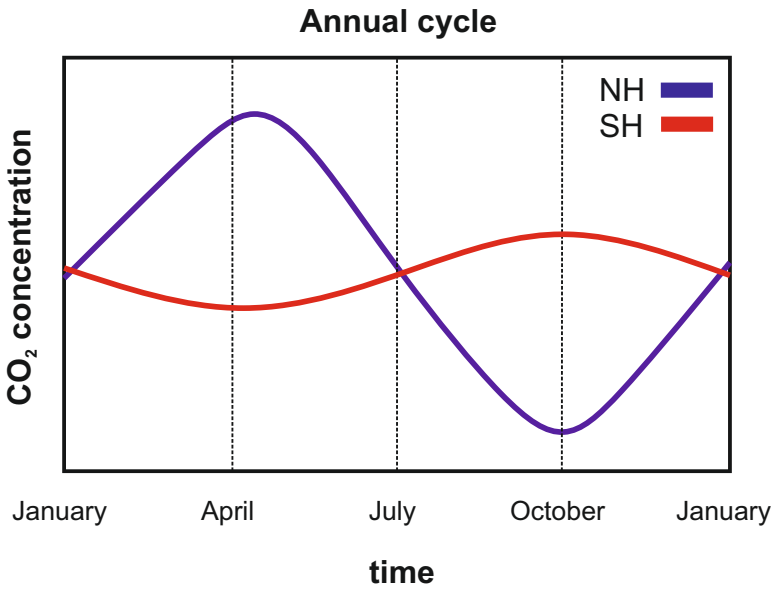

Figure 1.3: A schematic illustration of the annual cycle of CO_2 for the northern hemisphere (NH, blue) and the southern hemisphere (SH, red) with increasing CO_2 values in winter and a maximum in spring. Plants begin to grow, causing a CO_2 decrease with a minimum in autumn, where the cycle starts again. Atmospheric CO_2 fluctuations are more pronounced in the northern hemisphere.

1.2.3 Changes in the carbon cycle

Regarding small time scales, the slow and fast carbon cycles keep relatively constant amounts of CO_2 in atmosphere, land, plants and oceans if they are unaffected. A changing amount of carbon in one reservoir causes a perturbation in the others as well. In the Earth's history, variations in the carbon cycle were induced by climate change, caused by the altering amount of solar energy reaching the Earth. These alterations are mostly due to predictable shifts of the Earth's orbit or to volcanic activities.

In contrast, present changes in the carbon cycle occur in consequence of human activities like burning fossil fuels or land use change. By clearing forests, biomasses which otherwise could have removed CO_2 from the atmosphere to grow, are destroyed and replaced by crops or pastures, absorbing much less CO_2. In addition, the uncovered soil release carbon into the atmosphere. At the present time, the atmospheric carbon content increases by a little less than 1 GtC/year due to deforestation [Le Quéré et al., 2012].

In the absence of human activities, the carbon comprised in fossil fuels would have been released into the atmosphere by volcanic eruptions on large timescales. By burning fossil fuels the exchange of huge carbon amounts from land to the atmosphere is

accelerated leading to a carbon movement from the slow to the fast cycle. In total humans released about 8.3 GtC/year (2002–2011) into the atmosphere via fossil fuel burning [Le Quéré et al., 2012].
The increase of atmospheric CO_2 due to fossil fuel burning and deforestation is shown in Figure 1.4 for Mauna Loa (Hawaii). The measurement program is operated by the Scripps Institution of Oceanography and includes continuous CO_2 measurements from 1958 to present time [Keeling et al., 2005]. Since the start of recording in 1958, the CO_2 concentration increased from 315 ppm to 390 ppm in 2010.

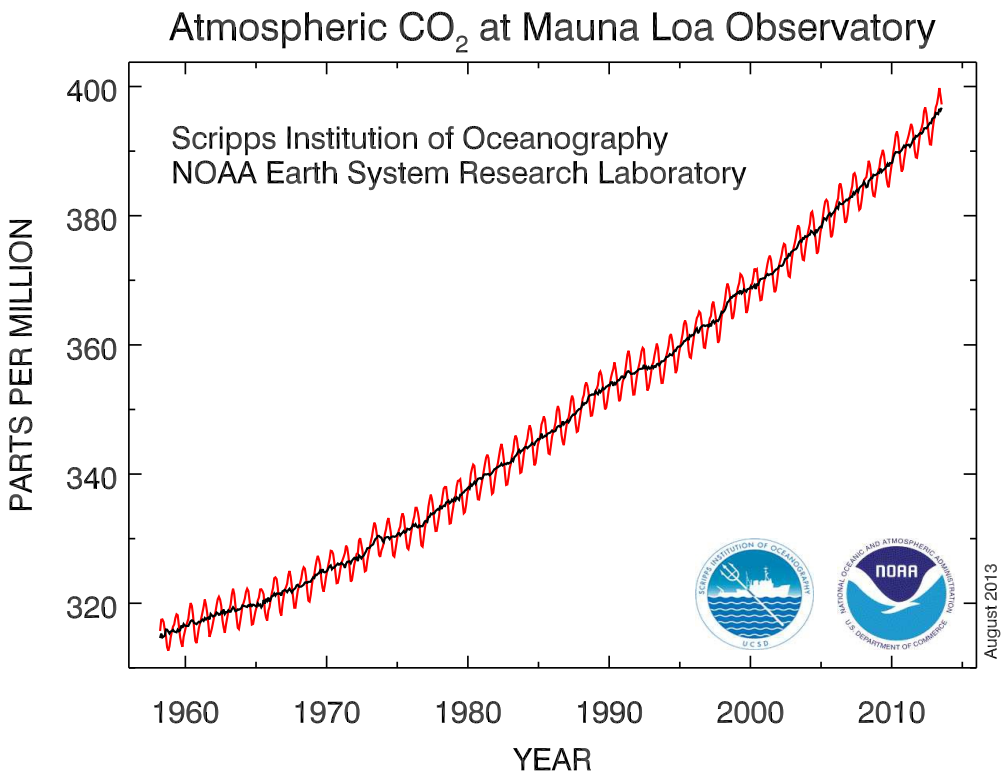

Figure 1.4: Time series of atmospheric CO_2 measurements at Mauna Loa (Hawaii). Since the start of recording in 1958 until 2010, the CO_2 concentration increased by about 75 ppm. (Taken from NOAA/ESRL[3])

Only a part of CO_2 (4.3 GtC/year, 46%) which is emitted by humans remains in the atmosphere [Le Quéré et al., 2012]. The residual extra carbon is taken up by ocean (26%) and land (28%), so that each reservoir is affected by changes in the carbon cycle, where important effects are the increase of atmospheric temperatures and the acidification of the oceans [Le Quéré et al., 2012]. In order to understand global climate

[3] www.esrl.noaa.gov/gmd/ccgg/trends/

change, the changes in the carbon cycle have to be investigated, where FTIR networks contribute by providing precise ground-based measurements of atmospheric CO_2.

1.3 The greenhouse effect

Humans have been living on Earth for millions of years but they started influencing the climate mainly at the time of the industrial revolution (∼1750). Fossil fuel burning and deforestation led to an increase in atmospheric CO_2 concentrations (see Section 1.2.3) accelerating the greenhouse effect and global warming, to which other gases also contribute. As a result, temperatures increase, glaciers melt and the sea level rises.
At the Earth's orbit the solar power flux density is about 1372 W/m^2 and is called the solar constant S. The incoming solar radiant power P for the Earth's cross section (πR_E^2) is:

$$P = \pi R_E^2 S = 175\ PW, \tag{1.1}$$

where R_E=6378 km is the Earth's radius. After dividing by the Earth's surface ($4\pi R_E^2$) a mean day-night value which represents the radiant power for the whole surface is given by:

$$p = \frac{S}{4} = 343\ \frac{W}{m^2}. \tag{1.2}$$

A fraction of the radiation is absorbed at the Earth's surface, increasing its temperature T to about 288 K. In order to keep a constant temperature, absorption and emission need to be balanced. The emission spectrum of a black body can be described by Planck's law:

$$B_\lambda(T) = \frac{2hc^2\lambda^{-5}}{\exp\left(\frac{hc}{\lambda kT}\right) - 1}, \tag{1.3}$$

where h is Planck's constant, λ is the wavelength, k is Boltzmann's constant and c is the speed of light. In the case of the Sun with a temperature of 6000 K, $B_\lambda(T)$ consists of relatively short wavelengths with a radiation maximum at λ_{max}=500 nm, due to Wien's displacement law

$$\lambda_{max} T = b \tag{1.4}$$

with the Wien's displacement constant b. In contrast, the Earth with a temperature of 288 K emits IR light assuming black body spectra.
In the absence of an atmosphere, the determination of the Earth's surface temperature would be very easy, applying Stefan Boltzmann's law:

$$J = \epsilon \sigma T_0^4, \tag{1.5}$$

with the emitted radiation J at temperature T_0, the emissivity ϵ (1 for a black body) and the Stefan Boltzmann's constant σ. Without any radiative interaction between Earth and atmosphere, the radiation balance can be described as:

$$(1 - A)\frac{S}{4} = \epsilon \sigma T_0^4. \tag{1.6}$$

The left hand sided term represents the Sun's radiation received by the Earth multiplied by the absorbed part $(1 - A)$, where $A \sim 30\%$ is the Earth's albedo. The real Earth's surface temperature (288 K) is much larger than the one calculated by means of equation 1.6. Applying values for A, S, ϵ and σ lead to a resulting temperature T_0 of 255 K (-18 °C). The difference of 33 K between T_E and T_0 is caused by the Earth's atmosphere and is called the greenhouse effect, making the Earth habitable. By using a value of ϵ being smaller than one, Equation 1.6 accounts for this effect, which originates to 62% from H_2O, 22% from CO_2 and 16% from other greenhouse gases like CH_4 or N_2O, where the contribution of CO_2 with about 7 K is very large compared to its atmospherical content. A schematic illustration of the natural greenhouse effect is shown in Figure 1.5.
GHGs are transparent for visible light. However they possess strong absorption bands in the IR region, causing an increase of temperature. These absorption bands may overlap for different gases, which results in an overall effect being composed by the effect of each gas. A part of the IR radiation emitted by the Earth's surface is absorbed and re-emitted by GHGs and clouds in all directions, which leads to an increase in surface and low tropospheric temperatures. A spectrum of the solar radiation emitted from Earth compared to one which can be detected at the top of the atmosphere is illustrated in Figure 1.6. The reduction of outgoing radiation is due to the absorption by GHGs in the corresponding region.

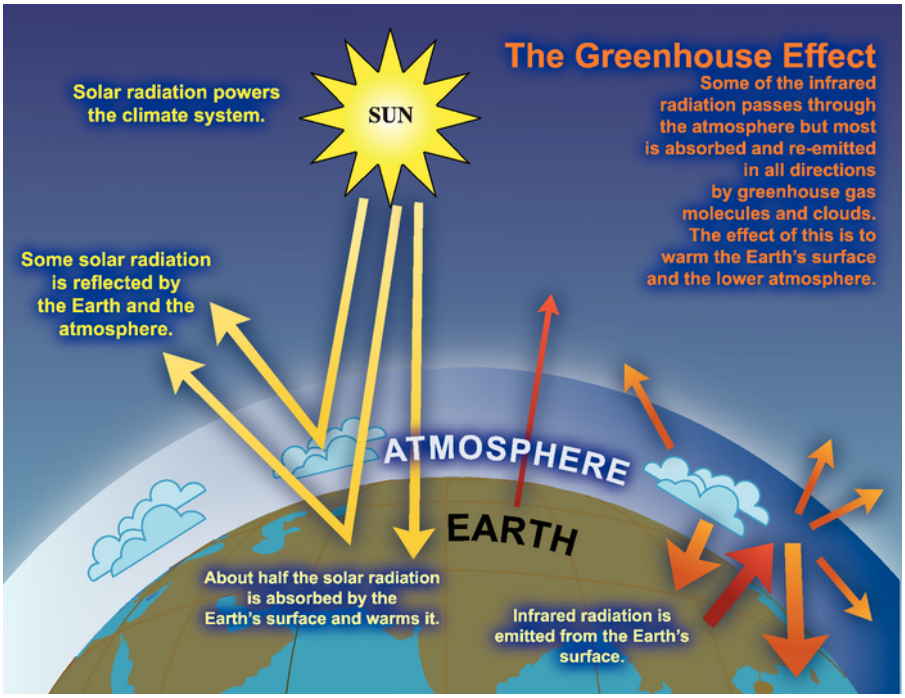

Figure 1.5: The natural greenhouse effect, where infrared radiation from the Earth's surface is absorbed by GHGs, leading to an increase in surface and low tropospheric temperatures. (Taken from IPCC [2007])

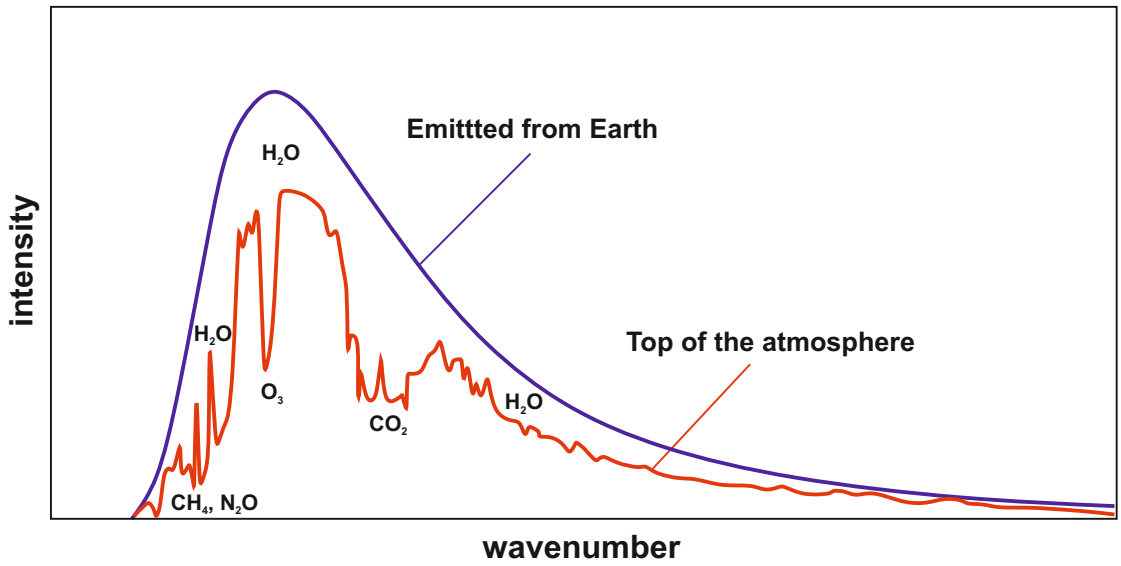

Figure 1.6: A spectrum of the solar radiation emitted from the Earth (blue) compared to the one which can be detected at top of the atmosphere (red). The reduction of outgoing radiation is due to the absorption of GHGs in the corresponding region.

1.3.1 The anthropogenic greenhouse effect

In addition to the natural greenhouse effect, the rise of atmospheric GHG concentrations for the last 250 years causes an extra atmospheric warming, called the anthropogenic or enhanced greenhouse effect.
Since the industrial revolution, CO_2 concentrations raised from 260–280 ppm in 1750 to 379 ppm in 2005 [IPCC, 2007]. The CO_2 growth rate will be doubled within the next 50–100 years, referred to pre-industrial concentrations [IPCC, 2001].
Assuming this doubling of CO_2 while concentrations of all other gases remain constant, the long wave radiation reaching space will be reduced by 4.1 W/m^2 [Schmidt et al., 2010]. To compensate this, the atmosphere gets warmer with a temperature rise of about 1.2 K ($\pm$ 10%) in the troposphere and Earth's surface [IPCC, 2001]. Positive feedbacks, like the increase of tropospheric water vapour, cause an additional warming resulting in an overall effect of 1.5–4.5 K [IPCC, 2001], which is still under investigation. Uncertainties are due to deficient knowledge about the interaction between radiation and clouds.
Supposing an already saturated CO_2 absorption, another increase in atmospheric CO_2 would not have any additional impacts on climate. But this is not the case. While the core of the 15 μm CO_2 band is saturated, the edges of the band remain unsaturated, being the reason for the unproportional but logarithmic behavior of radiative forcing related to an increase of CO_2. Each CO_2 doubling leads to reduced long wave radiation of 4.1 W/m^2, where other GHGs have similar effects causing an additional enhancement of this scenario.

1.3.2 Greenhouse gases

Greenhouse gases are, as the name implies, gases which contribute to the greenhouse effect. Most of the GHGs occur naturally, but concentrations have increased for the last 250 years due to human activities [IPCC, 2007]. They absorb parts of infrared radiation emitted from the Earth's surface leading to an increase in temperature. The contribution to radiative forcing (RF) for each gas is determined by the concentration change in the atmosphere during a certain time period and the effectiveness of disturbing the radiative balance. The four most important in the Kyoto protocol assigned GHGs are CO_2, CH_4, N_2O and the halocarbons, which are described below in more detail.

CO_2

Carbon dioxide is a long-lived GHG with an atmospheric lifetime varying between 5–200 years [IPCC, 2001]. It is soluble in water and a natural component of air with a content of about 400 ppm. The rise in CO_2 concentrations is mainly caused by fossil fuel burning and deforestation, where CO_2 is emitted and its sink (the plants) removed at the same time. However it is also released through natural processes like the decay of biomasses. The atmospheric CO_2 amount rose by about 120 ppm during the last 250 years, and by 19 ppm from 1995 to 2005 [IPCC, 2007]. Its contribution to radiative forcing (1.66 W/m^2) is very large [IPCC, 2007].

CH_4

Methane is the simplest alkane belonging to the group of carbon hydrates and is the major constituent of natural gasoline. In the atmosphere, it occurs only in trace amounts of <2 ppm. Because of its atmospheric lifetime of 12 years and its lower density, it is able to raise to higher atmospheric levels [IPCC, 2001]. The main human sources of CH_4 are agriculture, natural gas distribution and landfills, where there are also natural sources (e.g. wetland or unfreezing permafrost). Atmospheric CH_4 concentrations rose from 700 ppb in 1750 [Flückiger et al., 2002] to 1775 ppb in 2005 [IPCC, 2007], where in the period between 1999–2006 concentrations remained at the same level and started to increase again in 2007 [Dlugokencky et al., 2009]. The reason for this behavior is still under investigation but supposed to be connected with the removement of CH_4 by the reaction with the photochemically built OH-radical [IPCC, 2007]. Methane has a RF value of 0.48 W/m^2 [IPCC, 2007].

N_2O

Nitrous oxide is a water soluble, transparent gas belonging to the group of nitrogen oxides, where it is the main source of NO and NO_2. It has an atmospheric lifetime of 114 years, with sources in fertilization and fossil fuel burning [IPCC, 2001]. In nature it is also released from soils and oceans. Since pre-industrial time, N_2O concentrations increased from 270 ppb in 1750 to 319 ppb in 2005 [IPCC, 2007]. N_2O has the fourth largest RF value (0.16 W/m^2) among the long-lived GHGs [IPCC, 2007].

Halocarbons

Halocarbons consist, as the name implies, of carbon and at least one of the halogens. They include the chlorofluorocarbons (CFCs), hydrochlorofluorocarbons (HCFCs) and

hydrofluorocarbons (HFCs) and are very stable with atmospheric lifetimes in the range of 1.4–1700 years [IPCC, 2007]. Since most of the other GHGs are unwanted minor products, halocarbons are produced selectively as refrigeration agents or for other industrial applications. By reason of the potential to take part in ozone destruction, the consumption and production of CFCs and HCFCs is forbidden since 1989 (Montreal Protocol). Due to the fact that HFCs do not destroy stratospheric ozone, they are not controlled by the Montreal Protocol and are the major substitutes for CFCs and HCFCs. However they are major GHGs with RF values of about 0.25 W/m^2 and show increasing concentrations (10–15% per year) during the last few years [Velders et al., 2012]. In constrast, CFCs and HCFCs are already decreasing, but this process is very slow due to their large atmospheric lifetimes [IPCC, 2007].

Chapter 2

Remote sensing in the infrared region

This chapter outlines the fundamentals of remote sensing in the IR region. The formation of rotational-vibrational spectra is described in Section 2.1, first for diatomic molecules like carbon monoxide (CO) and hydrochloric acid (HCl) and later also for polyatomic molecules like CO_2, which is of special interest for this thesis. Section 2.2 is about spectral line shapes, which are used to determine vertical profiles of CO_2 in Chapter 8. The content of this chapter is mainly based on Atkins [2001], Griffiths and de Haseth [2007], Demtröder [2005] and Kramer [2007] where more detailed information can be found.

2.1 IR absorption spectroscopy

Infrared absorption spectroscopy deals with the interaction between infrared radiation and molecules, resulting in a change of the molecule's vibrational and rotational states due to absorption or emission. Concerning the atmosphere, its main components N_2 and O_2 are weak absorbers in the IR region, while trace gases like CO_2, H_2O or CH_4 are effective absorbers, leading to an increase of the Earth's temperature (greenhouse effect see Section 1.3). Absorption of IR radiation is only possible if molecules have the ability to change their dipole moment during transition, which is the selection rule for IR absorption spectroscopy. For convenience, this section will first deal with the formation of IR spectra of diatomic molecules like HCl or CO, whereas CO_2 is discussed at the end of this section.

2.1.1 Diatomic molecules

Assuming a harmonic oscillation, the vibrational energy levels of a diatomic molecule, consisting of atoms with masses m_1 and m_2, can be described as:

$$E_v = \left(v + \frac{1}{2}\right)\frac{h}{2\pi}\omega \quad \text{with} \quad v = 0, 1, 2, ... \quad \text{and} \quad \omega = \left(\frac{k_f}{\mu}\right)^{\frac{1}{2}}, \tag{2.1}$$

where $\mu = \frac{m_1 m_2}{m_1 + m_2}$ is the reduced mass, k_f the force constant and ω the angular frequency. These energy levels are quantized denoted by the vibrational quantum number v. Expressed by means of wavenumbers $\tilde{\nu}$ the so called vibrational terms G are given by:

$$G(v) = \left(v + \frac{1}{2}\right)\tilde{\nu} \tag{2.2}$$

with

$$\tilde{\nu} = \frac{\omega}{2\pi c}. \tag{2.3}$$

The general quantum mechanical selection rule for the vibrational quantum number v results from the analysis of the transition dipole moment and the harmonic oscillator's wave functions:

$$\Delta v = \pm 1, \tag{2.4}$$

where $\Delta v = +1$ means absorption and $\Delta v = -1$ emission of radiation. At room temperature, kT is about one order of magnitude smaller than the energy difference between typical vibrational levels and nearly all molecules are located in the ground state. Therefore, the most important transition is the one from $v = 0$ to $v = 1$.
This simple approach is not completely correct, because it is based on a harmonic potential, which is not a good approximation for all distances between atoms. Dissociation would not be possible and atoms located at the same place would have a finite energy. Therefore, in the case of highly excited molecules, an anharmonic potential is used, which is wider for higher energy levels with smaller distances between the vibrational states (Figure 2.1). Using the Morse potential, an expression for the anharmonic vibrational terms can be described with:

$$G(v) = \left(v + \frac{1}{2}\right)\tilde{\nu} - \left(v + \frac{1}{2}\right)^2 x_{eq}\tilde{\nu} \quad \text{with} \quad x_{eq} = \frac{\tilde{\nu}}{4D_e}, \tag{2.5}$$

where x_{eq} is the anharmonicity constant and D_{eq} the depth of the potential. The first part of Equation 2.5 describes the harmonic behavior, while the second part is due to the anharmonicity. Compared to harmonic vibrational energy levels, Δv is now allowed to be larger than ± 1.

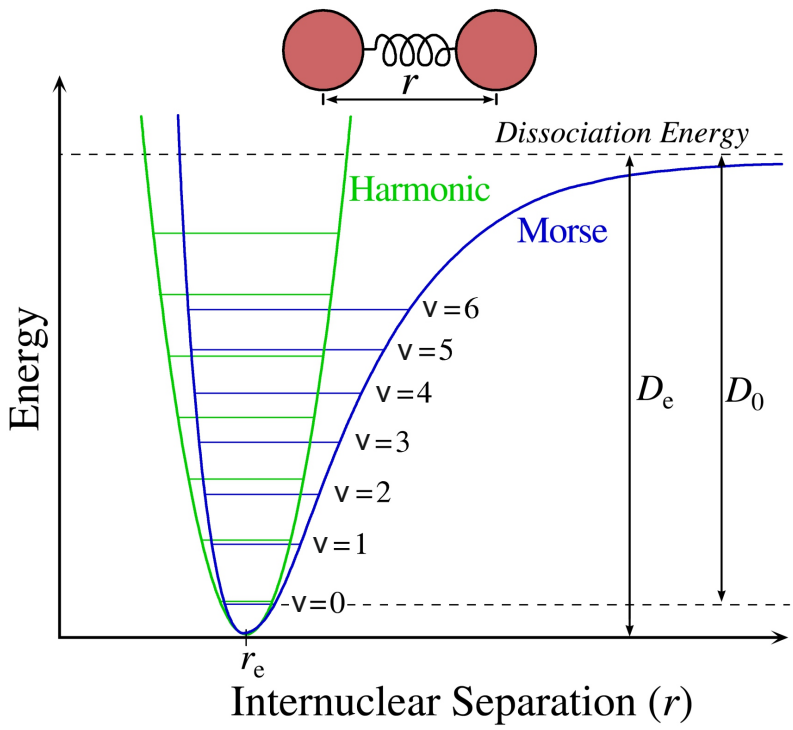

Figure 2.1: Comparison between harmonic and anharmonic oscillations (Morse potential), where the latter one is wider for higher energy levels with smaller distances between vibrational states v. (Taken from Wikipedia[4])

If a highly resolved vibrational spectrum is recorded in the gas phase, every single vibrational transition gives rise to many nearby lines, forming a band. The line's distances are in the order of 10 cm^{-1} and result from additional rotational transitions, which occur simultaneously and are described in the following.
Assuming a rigid rotor, where rotations can only occur around one axis perpendicular to the molecule's axis (this is the case for CO or HCl), the angular momentum around the molecule's axis is 0. The resultant rotational terms are:

$$F(J) = BJ(J+1) \quad \text{with} \quad J = 0, 1, 2, ... \quad \text{and} \quad B = \frac{h^2}{8\pi^2\Theta}, \tag{2.6}$$

[4]http://de.wikipedia.org

where B is the rotational constant, J the rotational quantum number, and $\Theta = \mu R^2$ the moment of inertia (R: bond length of the molecule). However this model is an approach, where the centrifugal force is neglected. In reality, molecules are affected by this force, causing a change in their moment of inertia. In case of a diatomic molecule, the bond is stretched, the moment of inertia gets larger leading to a smaller rotational constant. Compared to the rigid rotor model, rotational energy levels move closer together. The resultant rotational terms, including the centrifugal force are:

$$F(J) = BJ(J+1) - D_J J^2 (J+1)^2 \quad \text{with} \quad D_J = \frac{4B^3}{\tilde{\nu}^2}, \tag{2.7}$$

with the centrifugal distortion constant D_J.
For a linear molecule, the selection rule for the rotational quantum number is:

$$\Delta J = \pm 1, \tag{2.8}$$

where $\Delta J = +1$ stands for absorption and $\Delta J = -1$ for emission. The special case $\Delta J = 0$ is only allowed for molecules with angular momentums in parallel to their symmetry axis.
The structure of a combined rotational-vibrational spectrum of a diatomic molecule can be described with the rotational-vibrational term S:

$$S(v, J) = G(v) + F(J). \tag{2.9}$$

Neglecting anharmonicity and centrifugal forces, S can be written as:

$$S(v, J) = \left(v + \frac{1}{2}\right)\tilde{\nu} + BJ(J+1). \tag{2.10}$$

The required energy for transitions between the molecule's initial and final state is provided by absorbed photons, where vibrational transitions need more energy than the rotational ones. An energy level scheme illustrating the possible transitions is given in Figure 2.2.
During vibrational transitions between v and $v+1$, J changes by ± 1 (and in special cases by 0), leading to absorption lines which can be divided into three different groups, called the branches of a spectrum:

- Transitions from v to $v+1$ with $\Delta J = -1$ build the P-branch and span smaller energy differences with increasing J.

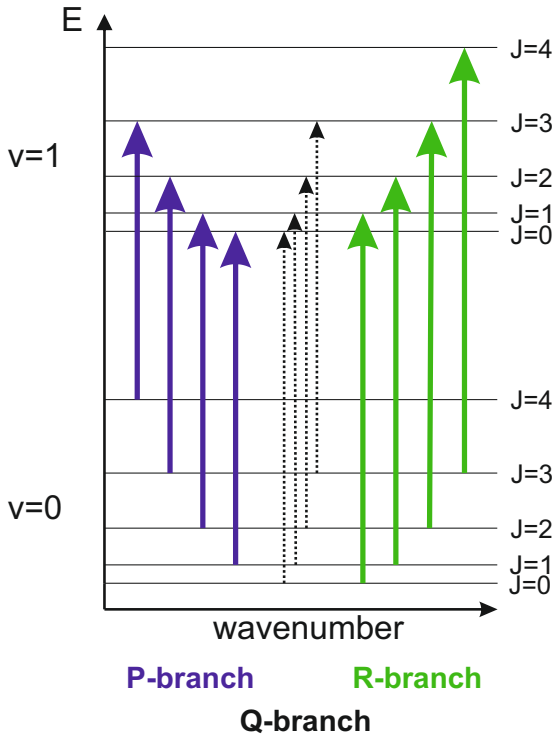

Figure 2.2: Possible transitions between v and $v+1$ causing P-, R- and Q-branch. Transitions with $\Delta J = -1$ build the P-branch, whereas $\Delta J = +1$ transitions build the R-branch. The Q-branch in between is due to pure vibrational transitions and only allowed for molecules with angular momentums in parallel to their symmetry axis.

- Transitions from v to $v+1$ with $\Delta J = +1$ build the R-branch and span larger energy differences with increasing J.
- Transitions from v to $v+1$ with $\Delta J = 0$ build the Q-branch in between the P- and the R-branch. These are pure vibrational transitions.

In Figure 2.3, a resulting spectral band of HBr is shown, where P- and R-branches are clearly visible. In addition to the appearance of different branches, line intensities vary for different J, caused by different populations N_i of states i following Boltzmann's statistic:

$$\frac{N_J}{N_0} = (2J+1)\, e^{\frac{-h\nu}{kT}}, \tag{2.11}$$

where $2J+1$ is the degeneracy of a rotational energy level and ν the frequency. Line intensities increase from the middle of the band to outer parts due to an increasing J in the dominating term $2J+1$. At marginal parts of the band line intensities decrease

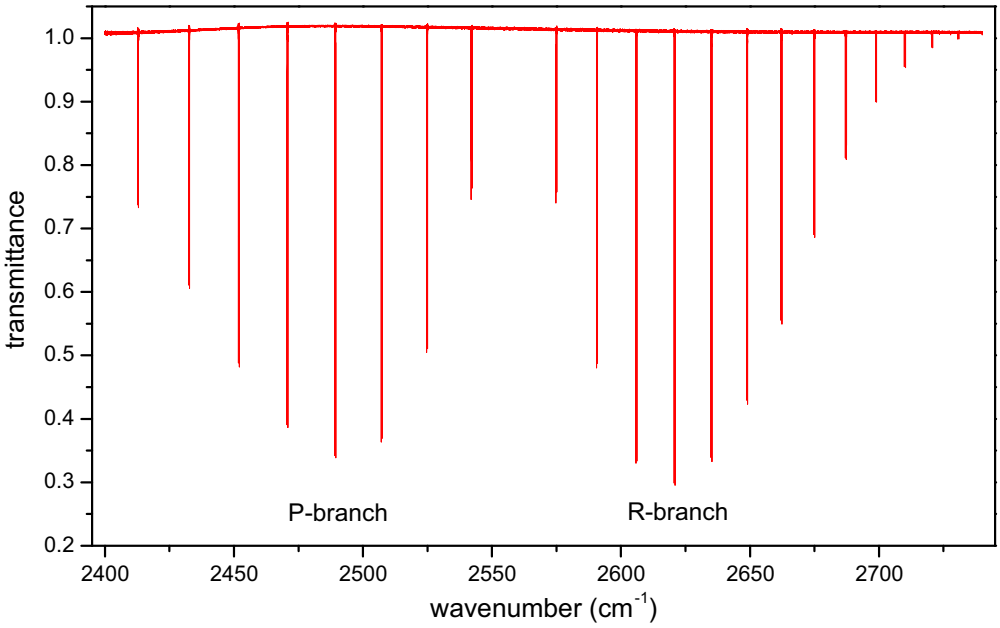

Figure 2.3: Transmittance spectrum of HBr recorded with a Bruker 120HR at Kiruna (Sweden), where P- and R-branches are clearly visible.

with increasing J because thermal distribution of the molecular states ($e^{\frac{-h\nu}{kT}}$) becomes more important and higher energetic states cannot be filled.

2.1.2 Polyatomic molecules

Spectra of polyatomic molecules like CO_2 are much more complicated. A nonlinear molecule with N atoms contains $3N$ degrees of freedom (DOF) due to its motion in 3 dimensions, where 3 out of them are needed for center of mass motion and another 3 for rotation resulting in $3N$-6 vibrational DOFs. In contrast, a linear molecule contains $3N$-5 vibrational DOFs due to only 2 rotational DOFs. A resultant spectrum of a polyatomic molecule therefore also consists of linear combinations of these vibrational modes.

Accordingly the linear CO_2 molecule with 3 atoms (N=3) consists of $3N$-5=4 vibrational DOFs. These different vibrational modes with their corresponding wavenumbers are displayed in Figure 2.5. In contrast to the asymmetric stretching vibration and both bending vibrations, which are IR active, the symmetric stretching vibration is IR inactive because of the unchanged dipole moment. Concerning stretching vibrations, ΔJ is not allowed to be 0, due to the changing dipole moment in parallel to the molecule's axis. This is not the case for bending vibrations, which remove the molecule's linearity

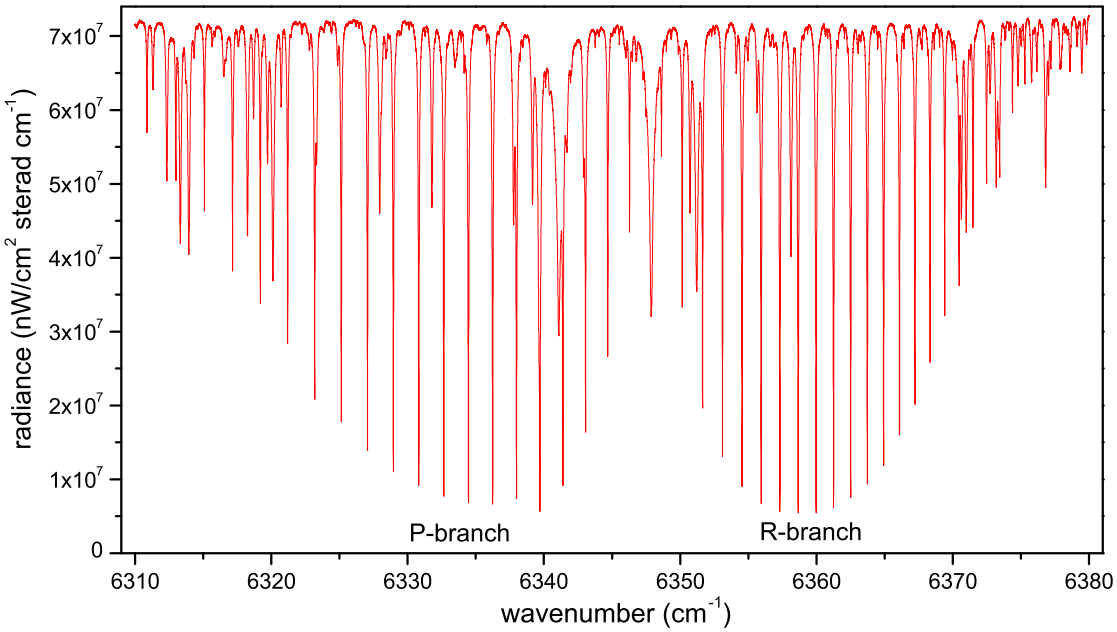

Figure 2.4: IR absorption spectrum of CO_2 recorded with the Bruker 125HR at Karlsruhe. Spectral lines are due to combinations of different vibrational modes: $2\tilde{\nu}_1+2\tilde{\nu}_2+\tilde{\nu}_3$ (see Figure 2.5).

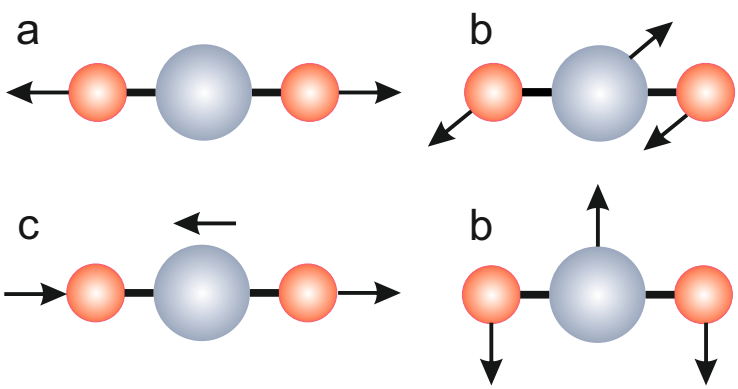

Figure 2.5: The four vibrational modes of a linear triatomic molecule like CO_2, where the symmetric stretching vibration (a) is IR inactive. The corresponding spectral lines are $\tilde{\nu}_1$=1388 cm^{-1} (a, symmetric stretching), $\tilde{\nu}_2$=667 cm^{-1} (b, bending) and $\tilde{\nu}_3$=2349 cm^{-1} (c, asymmetric stretching)[Atkins, 2001].

resulting in a dipole moment change perpendicular to the molecule's axis. Since this Ph.D. thesis mainly deals with CO_2, the structure of a resulting CO_2 band is shown in Figure 2.4, where spectral lines are due to combinations of different vibrational modes.

2.2 Spectral line shapes

Absorption lines in rotational-vibrational spectra are not infinitesimally narrow. Different velocity components and interactions between molecules lead to line broadening, where the fundamental source is the natural line broadening, resulting from the finite lifetime of the excited states. Natural line broadening has a Lorentz line shape, where typical values of $\Delta\tilde{\nu}$ are approximately 10^{-8} cm^{-1} [Hase, 2000]. Compared to other effects (Doppler broadening or pressure broadening) this value can be neglected for atmospheric conditions.

2.2.1 Doppler broadening

Doppler broadening occurs due to the Doppler effect caused by the thermic motion of molecules. If such a molecule moves with velocity v_x in the observer's direction and emits radiation with the angular frequency ω_0, the radiation reaching the observer is then shifted to ω:

$$\omega = \omega_0 \left(1 + \frac{v_x}{c}\right). \tag{2.12}$$

Assuming a local thermic equilibrium, the velocity distribution is given by the Maxwell distribution. The number of atoms per volume unit $\mathrm{n}(v_x)\, dv_x$ with velocity component v_x in the range of v_x to $v_x + dv_x$ is given by:

$$n\left(v_x\right) dv_x = \frac{N}{v_w\sqrt{\pi}} \exp\left(-\frac{v_x}{v_w}\right)^2 dv_x, \tag{2.13}$$

with the most likely velocity v_w:

$$v_w = \sqrt{\frac{2kT}{m}} \tag{2.14}$$

and the total number of molecules per volume unit N. On the basis of Equation (2.12) the number of atoms whose absorption (or emission) take place in the range between ω and $\omega + d\omega$ is described by:

$$n\left(\omega\right) d\omega = \frac{cN}{\omega_0 v_w\sqrt{\pi}} \exp\left(-\frac{c\left(\omega - \omega_0\right)}{\omega_0 v_w}\right)^2 d\omega. \tag{2.15}$$

In consequence, Doppler broadened spectral lines have the following shape of a Gaussian distribution:

$$f_D(\omega) = \frac{c}{\omega_0 v_w \sqrt{\pi}} \exp\left(-\left(\frac{c(\omega-\omega_0)}{\omega_0 v_w}\right)^2\right). \tag{2.16}$$

The full width at half maximum is frequency dependent:

$$\Delta\omega_D = 2\sqrt{\ln 2}\omega_0 \frac{v_w}{c}, \tag{2.17}$$

and by means of Equation (2.14):

$$\Delta\omega_D = \frac{\omega_0}{c}\sqrt{\frac{8kT\ln 2}{m}}. \tag{2.18}$$

$\Delta\omega_D$ increases with rising temperatures, since the velocity distribution of the molecules is broadened. Typical values for $\Delta\tilde{\nu}_D = \frac{\Delta\nu}{c} = \frac{\Delta\omega_D}{2\pi c}$ are in the region of $3 \cdot 10^{-3}$ cm^{-1} (CO band at 2100 cm^{-1} and 270 K, Hase [2000]).

2.2.2 Pressure broadening

Pressure broadening occurs due to collisions of molecules, causing a shortened lifetime of excited states and broadened line shapes. The higher the number density of molecules, the larger is the probability of a collision. This means that pressure broadening has a larger effect on lower atmospheric levels than on higher ones. The resulting lines have, just like the natural broadened ones, a Lorentzian shape:

$$f_P(\nu) = \frac{1}{\sqrt{\pi}} \frac{\Delta\nu_P}{(\nu-\nu_0)^2 + \Delta\nu_P^2}. \tag{2.19}$$

With the mean time $\tau_{coll} = \frac{\sqrt{mkT}}{4\sqrt{\pi}d^2 p}$ between two collisions, the full width at half maximum caused by pressure broadening can be described as:

$$\Delta\nu_P = \frac{1}{2\pi\tau_{coll}} \sim p. \tag{2.20}$$

$\Delta\nu_P$ is proportional to pressure p and increases exponentially with height. Typical values for pressure broadened lines are in the region of $\Delta\tilde{\nu}_P = 4 \cdot 10^{-2}$ cm^{-1} (at 1 bar, Kramer [2007]).

2.2.3 The Voigt function

Both Doppler- and pressure broadening have to be taken into account to describe the shape of an atmospheric spectral line. Therefore the Voigt profile is the convolution of a Gaussian with a Lorentzian function:

$$f(\nu) = \int_{-\infty}^{+\infty} f_P(\nu') f_D(\nu - \nu') d\nu'. \tag{2.21}$$

Concerning the atmosphere, $\Delta\nu_D$ decreases with height from the ground to the tropopause, where it starts to increase again due to rising temperatures in the stratosphere. In contrast, $\Delta\nu_P$ is proportional to p, causing an exponential decrease with height. To summarize, pressure broadening is the dominating effect for lower levels (troposphere to middle stratosphere), whereas Doppler broadening is more important for higher levels (middle stratosphere and upwards). At an altitude of 31 km Doppler and pressure broadening effects are of the same order (1000 cm^{-1} O_3 band, Kramer [2007]).

Chapter 3

FTIR spectroscopy

Fourier transform infrared spectroscopy is one of the most important techniques for remote sensing of GHGs. The principle and setup of an FTIR spectrometer is described in Section 3.1. Section 3.2 deals with the conversion of recorded interferograms into spectra by means of FT, where the content is mainly based on Beer [1992] and Griffiths and de Haseth [2007]. Two different FTIR networks are introduced in Section 3.3, while the last part of this chapter (Section 3.4) is about the IMK-related sites Izaña and Karlsruhe.

3.1 The FTIR spectrometer

In general, FTIR spectroscopy is a two beam interferometry on the basis of a Michelson interferometer, being the heart of the spectrometer (Figure 3.1). In case of ground-based atmospheric measurements, the Sun is the light source and the absorption during its path through the atmosphere is measured. The Sun's radiation is captured by the solar tracker on top of the container and is reflected by two movable mirrors downwards into the container. After passing three fixed mirrors, the light is focused on the input field stop, ensuring that only light of the solar disc's center is considered. This is controlled by a camera based system (Camtracker, Gisi et al. [2011]). Inside the spectrometer, the radiation reaches the beamsplitter and is divided into two beams. One of them is reflected by a fixed mirror, whereas the other one is reflected by a moving mirror. Both beams recombine at the beamsplitter, where the optical path difference x depends on the position of the movable mirror. The beam passes several other optical components and is finally focused on the detector, which determines the intensity as a function of the optical path difference, where the resulting AC part of the signal is called an interferogram.

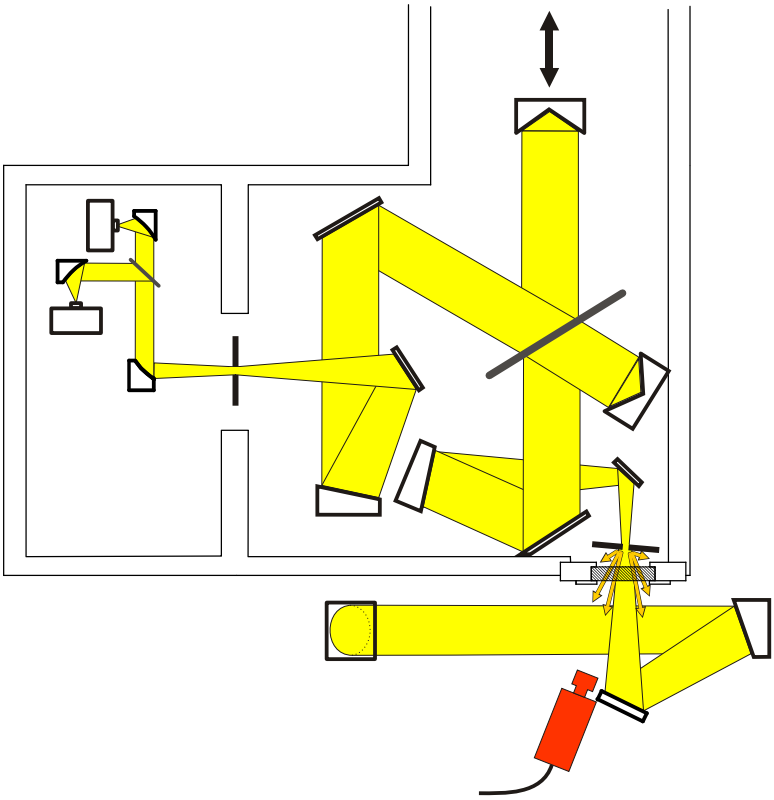

Figure 3.1: Schematic illustration of the FTIR spectrometer (top view) used within this work. (Taken from Gisi et al. [2011])

For an arbitrary large x, the resulting interferogram would contain all the spectral information. Since this is not the case, the information content is limited causing a finite resolution. A single mode helium-neon (HeNe) laser is additionally used to exactly determine the optical path difference. The laser beam has the same light path as the sunlight and each zero crossing of the laser's interferogram represents a sampling point. To improve the signal to noise ratio, two or more scans are combined for each measurement.
Compared to a scanning monochromator, one of the most important advantages of FTIR spectroscopy is the saved time due to the simultaneous detection of all wavelengths (Felgett's advantage).

3.2 The Fourier transformation

In general, the principle of Fourier transformation (FT) is used for the analysis of measurement signals. Concerning FTIR spectroscopy, the received intensity of the

beam as a function of optical path difference x can be converted into a spectrum. Considering a monochromatic source of light, the two interfered wave trains show a phase difference depending on x. The beams interfere constructive if x is a multiple of the wavelength λ:

$$x = n\lambda \quad \text{with} \quad n = 0, 1, 2, \ ..., \tag{3.1}$$

where the detected intensity is equal to the intensity of the source. In case of destructive interference, x is an uneven multiple of $\frac{\lambda}{2}$:

$$x = \left(n + \frac{1}{2}\right)\lambda \quad \text{with} \quad n = 0, 1, 2, \ ..., \tag{3.2}$$

and the detector records a minimum. Therefore the resulting interferogram $I'(x)$ is a harmonic oscillation and can be described as a cosine-function:

$$I'(x) = I(\tilde{\nu})\left(1 + \cos\left(2\pi\tilde{\nu}x\right)\right) \quad \text{with} \quad \tilde{\nu} = \frac{1}{\lambda}. \tag{3.3}$$

If the light of the source is not monochromatic but contains many wavenumbers (as the Sun), the correct intensity is given by integration over all wavenumbers:

$$I(x) = \int_{-\infty}^{\infty} I(\tilde{\nu})\left(1 + \cos\left(2\pi\tilde{\nu}x\right)\right) d\tilde{\nu} \tag{3.4}$$

$$= \int_{-\infty}^{\infty} I(\tilde{\nu})\, d\tilde{\nu} + \int_{-\infty}^{\infty} I(\tilde{\nu}) \cos\left(2\pi\tilde{\nu}x\right) d\tilde{\nu} \tag{3.5}$$

$$= I_{DC}(x) + I_{AC}(x). \tag{3.6}$$

The resulting interferogram $I(x)$ can be divided into a constant term (I_{DC}) and a modulated one (I_{AC}), where the last mentioned term is more important and in general called the interferogram. Equation (3.5) is only valid assuming the spectrum to be symmetric around the origin. If this is the case, also negative values are allowed for the integration variable. The interferogram is the Fourier transform of the spectrum $I(\tilde{\nu})$, which can be calculated on the basis of a FT:

$$I(\tilde{\nu}) = \int_{-\infty}^{\infty} I_{AC}(x)\, cos\left(2\pi\tilde{\nu}x\right) dx. \tag{3.7}$$

Equations (3.5) and (3.7) are only valid for continuous recorded interferograms. This is not the case for FTIR spectrometers where the sampling frequency is limited and

sampling occurs at a limited number of x values with equal distances Δx. As already described in Section 3.1 the precise sampling is achieved with coupling a HeNe reference laser into the spectrometer.
For discrete and equally spaced values of Δx, the discrete Fourier transformation (DFT) has to be applied:

$$I_{AC}\left(n\Delta x\right) = \frac{1}{\sqrt{N}} \sum_{m=0}^{N-1} I\left(m\Delta\tilde{\nu}\right) \exp\left(-i2\pi\frac{nm}{N}\right) \tag{3.8}$$

$$I\left(m\Delta\tilde{\nu}\right) = \frac{1}{\sqrt{N}} \sum_{n=0}^{N-1} I_{AC}\left(n\Delta x\right) \exp\left(-i2\pi\frac{nm}{N}\right), \tag{3.9}$$

with the number N of discrete, equally spaced measuring points. The previous used continuous variables x and $\tilde{\nu}$ are now replaced by $n\Delta x$ and $m\Delta\tilde{\nu}$ respectively. In the spectrum, the distance $\Delta\tilde{\nu}$ is linked with Δx via:

$$\Delta\tilde{\nu} = \frac{1}{N\Delta x}. \tag{3.10}$$

Therefore, the resolution is inversely proportional to the greatest possible path difference OPD_{max}. The spectrum is not allowed to contain frequencies larger than the so called Nyquist-frequency:

$$\tilde{\nu}_{Nyquist} = \tilde{\nu}_{max} - \tilde{\nu}_{min} = \frac{1}{2\Delta x} \tag{3.11}$$

due to the discrete sampling of the interferogram. The smaller Δx the larger is the detectable region. $\tilde{\nu}_{max}$ and $\tilde{\nu}_{min}$ limit the spectrometer's spectral range and are called high folding limit (HFL) and low folding limit (LFL). If the detector determines frequencies outside of $\tilde{\nu}_{Nyquist}$, the resulting spectrum cannot be created by DFT. As a consequence, these spectral contributions are folded back into the observed region, leading to a distortion of the spectrum, which is called aliasing. Due to the recording of spectra up to 10000 cm^{-1} and the reference laser's wavelength of 632.988 nm, the HFL is set to 15798 cm^{-1}, where the interferogram is sampled on every zero crossing of the reference laser's interferogram.
In practice, the analysis on the basis of DFT with Equations (3.8) and (3.9) is rarely used, due to $2N^2$ required arithmetic operations, which need a lot of time. Therefore the fast Fourier transformation (FFT, Cooley and Tukey [1965]) is utilized, needing only $3N\log_2 N$ arithmetic operations but requiring the number of sampling points to be a power of 2.

Apodization and instrumental line shape

Due to the limited path of the mirror, the interferogram is truncated at OPD_{max}, leading to spectral artifacts which have to be eliminated. The interferogram's truncation can be described mathematically as the multiplication of an infinite interferogram $I_\infty(x)$ with a boxcar function $B(x)$ which is 1 for $|x| \leq \mathrm{OPD}_{max}$ and 0 for $|x| > \mathrm{OPD}_{max}$:

$$I_{AC}(x) = I_\infty(x) \cdot B(x). \tag{3.12}$$

The measured spectrum $I(\tilde{\nu})$ is the convolution of the Fourier transforms of $I_\infty(x)$ and $B(x)$, where the Fourier transform $C(\tilde{\nu})$ of $B(x)$ is the following sinc-function:

$$C(\tilde{\nu}) = \frac{\sin(2\pi\ \mathrm{OPD}_{max}\ \tilde{\nu})}{2\pi\tilde{\nu}\ OPD_{max}} = \mathrm{sinc}(2\pi\tilde{\nu}\ \mathrm{OPD}_{max}). \tag{3.13}$$

The width of the sinc-function defines the spectral resolution, where the full width at half maximum (FWHM) of $C(\tilde{\nu})$ is $\frac{0.6035}{\mathrm{OPD}_{max}}$.
However the sinc-function has other important effects, namely negative side lobes leading to unrealistic values in the measured spectrum. In order to avoid this effect, the interferogram can be modified by means of the Boxcar function's multiplication with another function (e.g. Gaussian or triangle). This method is called apodization, causing reduced side lobes as well as a reduced spectral resolution (Figure 3.2). Due to different definitions of two separated peaks in a spectrum, the resolution cannot be defined explicitly. In this work a common Fourier transform spectrometer (FTS) resolution of

$$\Delta\tilde{\nu} = \frac{0.9}{\mathrm{OPD}_{max}} \tag{3.14}$$

is defined. An overview of different apodization functions is given in Figure 3.2.
The sinc-function (Equation 3.13) is also called the instrumental line shape (ILS), being a measure of how the spectrometer deforms a sharp spectral line. Due to misalignments, the real ILS might be asymmetric or might have a smaller amplitude than the ideal one, which has to be considered within the retrieval. Therefore, the ILS has to be monitored regularly by using gas cell measurements (common are HCl or N_2O). To do so, the cell is positioned into the light path of a black body (about 1000 °C). With the software LINEFIT [Hase et al., 1999] [Hase, 2012a], the instrument specific ILS is calculated by comparing the measured line shape with the theoretical one.

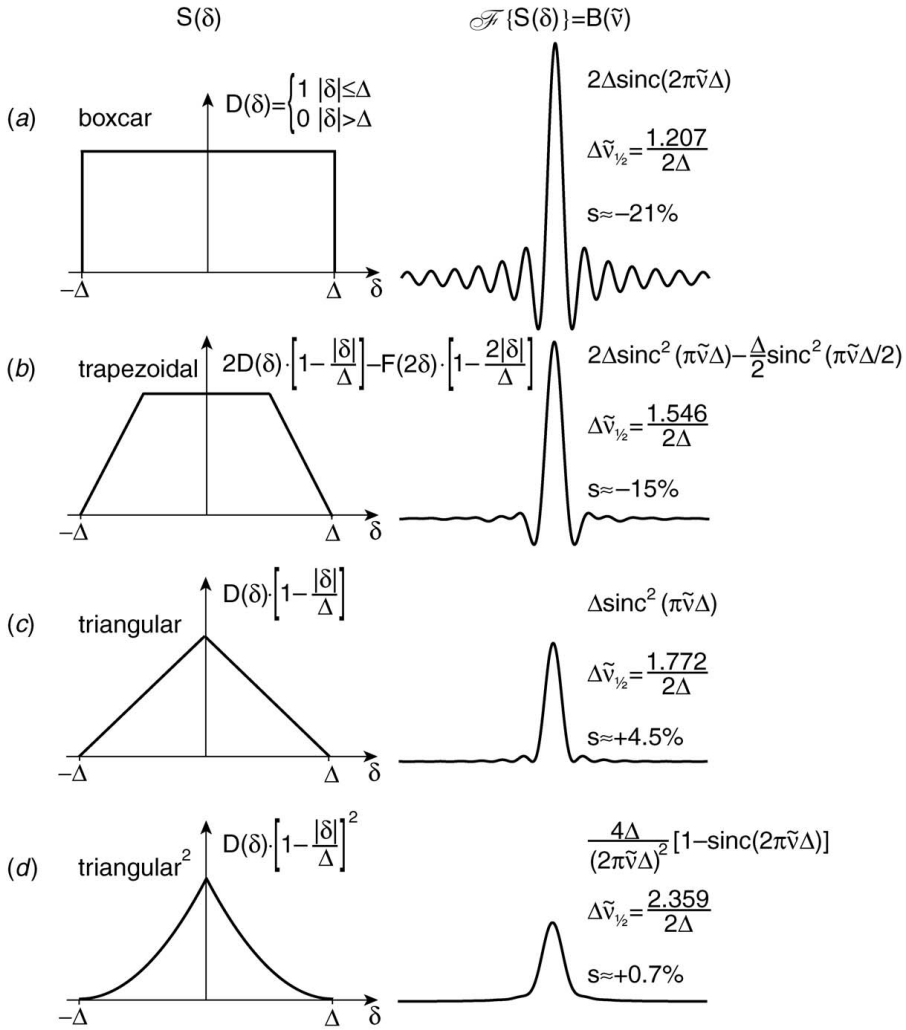

Figure 3.2: An Overview of different apodization functions: a) boxcar b) trapezoidal c) triangular and d) triangular^2. (Taken from Griffiths and de Haseth [2007])

3.3 FTIR networks

Ground-based FTIR measurements are available at various sites around the world for determining atmospheric trace gas concentrations and investigating climate change. Most of these sites take part in FTIR networks to ensure a network wide quality standard concerning both measurements and data analysis. The retrieved results are stored on a network database being available for public access. Below, the two most important FTIR networks which are the Infrared Working Group (IRWG) of the Network for the Detection of Atmospheric Composition Change (NDACC) and the Total Carbon Column Observing Network (TCCON) are described in more detail.

3.3.1 NDACC - IRWG Network

Over 20 FTIR sites worldwide participate in the Infrared Working Group of the NDACC, analyzing ground-based atmospheric absorption spectra in the mid-infrared (MIR) region. These spectra are used to retrieve concentrations of the atmospheric trace gases O_3, HNO_3, HCl, HF, CO, N_2O, CH_4, HCN, C_2H_6 and $ClONO_2$.

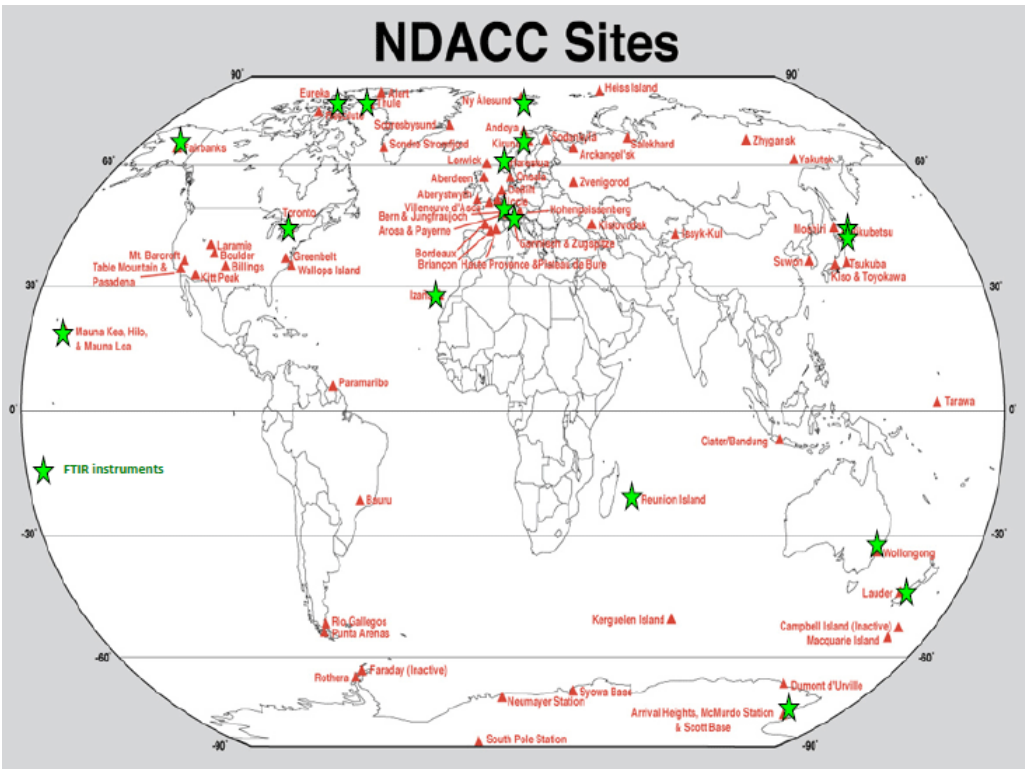

Figure 3.3: Map of worldwide NDACC stations (red), where NDACC – IRWG sites are shown as green stars. (Taken from the NDACC web page[5])

The network's goal is to record and understand the chemical and physical state of the upper troposphere and the stratosphere [Hannigan, 2011]. Since the first data have already been retrieved in 1978 (Kitt Peak, USA), the network's data are suitable to investigate long term trends of important trace gases like ozone.

3.3.2 TCCON Network

The TCCON was established in 2004 to retrieve precise and accurate total column amounts of atmospheric trace gases like CO_2, CH_4, N_2O and CO from ground-based

[5]http://www.ndsc.ncep.noaa.gov/

solar absorption spectra in the NIR region [Toon et al., 2009] [Wunch et al., 2010] [Wunch et al., 2011]. In comparison to the MIR spectral region, which provides strong signatures of the radiative most important GHGs CO_2 and CH_4, the weaker NIR combination and overtone absorption bands of these gases are more useful [Wunch et al., 2011]. Meanwhile there are 19 TCCON stations worldwide, with gaps in South America, Africa and Asia. Some of the TCCON sites have in situ measurements nearby, which can be used for comparison and calibration.

Figure 3.4: Map of worldwide TCCON stations. Operational sites are shown with red dots whereas blue squares belong to future sites. (Taken from the TCCON web page[6])

The main goals of the network are to provide a strictly controlled dataset for the validation of satellites like GOSAT or OCO-II (will be launched in 2014), to improve and understand the carbon cycle and to provide a transfer standard between satellite and surface in situ measurements. Requirements for a membership are:

- the same instrumentation (Bruker 125HR), data acquisition and instrumental settings
- common data processing and software (GFIT)
- calibration onto the World Meteorological Organization's (WMO) gas scale (aircraft campaigns).

To achieve the last requirement, TCCON measurements are compared with in situ profiles, recorded in the framework of aircraft campaigns. The total column accuracy

[6]http://www.tccon.caltech.edu/

requirements within the TCCON are very strict with 0.1%, which is exactly the accuracy required to detect an interhemispheric flux difference of 1 GtC/year [Olsen and Randerson, 2004].

3.4 IMK-related stations

Three FTS are operated by the ground-based FTIR group at the KIT, Institute of Meteorology and Climate Research (IMK), which are located in Karlsruhe (Germany), Kiruna (Sweden) and Izaña (Tenerife, Spain). Additional two FTS are run in cooperation with partners in Addis Ababa (Ethiopia) and Altzomoni (Mexico). Whereas the sites Kiruna and Izaña have already joined the NDACC many years ago (1996 and 1999 respectively), the Addis Ababa, Altzomoni and Karlsruhe sites are planned to become part of the network within the next years. Due to their relevance for this Ph.D. thesis, the IMK-related TCCON sites Izaña and Karlsruhe will be described in more detail.

3.4.1 Izaña

The Izaña Atmospheric Research Center is a subtropical high mountain observatory on Tenerife (28.3 °N, 16.5 °W, Canary Islands, Spain) located at 2370 m altitude over a temperature inversion layer, acting as a natural barrier for local pollution. The site provides an extensive measurement program, which includes both in situ (within the Global Atmospheric Watch, GAW[7]) and ground-based FTS measurements. The latter were started in the late 1990s in collaboration between the Meteorological State Agency of Spain (AEMET) and KIT. The FTS program is involved in both NDACC (since 1999) and TCCON (since 2007), where the TCCON measurements are acquired with a Bruker 125HR containing a room temperature indium gallium arsenide (InGaAs) detector. The spectrometer is housed in a climatized 20 ft container.

3.4.2 Karlsruhe

The TCCON site Karlsruhe is located at KIT Campus North (49.1 °N, 8.5 °E, Germany), 110 m above sea level in between the other TCCON sites Orleans (France) and Bialystok (Poland). A climatized 20 ft container with a Bruker 125HR inside has been set up in the end of 2009, which is prepared for automatization. Although the

[7] http://www.wmo.int/pages/prog/arep/gaw/gaw_home_en.html

(a) Bruker 125HR inside the climatized container in Karlsruhe.

(b) Izaña 20 ft measurement container

Figure 3.5: Pictures of the spectrometer (Karlsruhe) and the measurement container (Izaña).

Karlsruhe site is only a member of the TCCON, measurements in the MIR are available, too. A dichroic filter reflects one part of the beam (NIR) to the InGaAs detector, whereas the other part is transmitted and reaches the MIR indium antimonide (InSb) detector. This allows to measure spectra in the MIR and NIR simultaneously. Because of the flat terrain, the Karlsruhe site is favorable for validating satellite data.

Chapter 4

Analysis of ground-based absorption measurements

In order to retrieve GHG concentrations, FTIR spectra have to be analyzed by means of the inversion theory, which is described in Section 4.1 based on Rodgers [2000] and Hase [2000]. In Section 4.2 different retrieval programs are introduced, while Section 4.3 is about the applied spectral windows for CO_2 and O_2. The last two Sections 4.4 and 4.5 deal with possible error sources such as erroneous solar zenith angles or periodic sampling errors (adapted from Dohe et al. [2013]) and the reduction of systematic errors by using O_2 as an internal network standard.

4.1 Inversion theory

By means of inverse calculations it is possible to derive vertical gas profiles from ground-based FTIR spectra. This is done by using only small parts of the spectrum, so called microwindows (MW), containing spectral lines of the target gas. The advantage of this procedure is a reduction of calculation time on the one hand, and the absence of additional disturbing lines from other gases on the other hand.
The inverse method starts with a forward calculation, assuming known vertical profiles, called first guess profiles. With the use of the forward model, a synthetic spectrum $\vec{S}_{in}$ can be described as a function of the state vector $\vec{f}$:

$$\vec{S}_{in} = \vec{S}\left(\vec{f}\right), \tag{4.1}$$

where $\vec{f}$ represents parameters like pressure, temperature or the volume mixing ratio (VMR), which influence the spectrum. In this regard, the assumption of discrete

values for these parameters, actually being continuous functions of place, is already a simplification. Based on the forward model, the partial derivatives of the spectrum with respect to the state vector can be described with the Jacobean matrix **A**:

$$\mathbf{A}_{mn}(f) = \frac{\delta S_{in}(k_m)}{\delta f_n}. \tag{4.2}$$

If $m<n$ Equation 4.2 is described as underconstrained due to more unknowns than measurements, whereas the case of $m>n$ is called overconstrained.
The measurable spectrum for modified $\vec{f}$ values can be determined by using the spectrum for $\vec{f_0}$ and the corresponding derivatives:

$$\vec{S}_{in}\left(\vec{f_0} + \delta\vec{f}\right) = \vec{S}_{in} + \mathbf{A}\delta\vec{f}, \tag{4.3}$$

where $\delta\vec{f}=\vec{f}-\vec{f_0}$. In the next step, the received spectra are compared to the measured ones with the aim of minimizing the difference $\Delta\vec{S}=\vec{S}_{mes}-\vec{S}_{in}$. This difference at each wavenumber can be assigned through **A** to the different gases. The start profile is changed and used for the next forward calculation. Due to nonlinearity, several iterations are necessary. The linear solution to minimize $\left|\Delta\vec{S}\right|^2$ for the $i+1$-th iteration step is given by:

$$\vec{f}^{i+1} = \vec{f}^{i} + \left(\mathbf{A}^{i,T}\mathbf{A}^{i}\right)^{-1}\mathbf{A}^{i,T}\Delta\vec{S}^{i} = \left(\mathbf{A}^{i,T}\mathbf{A}^{i}\right)^{-1}\mathbf{A}^{i,T}\left(\Delta\vec{S}^{i} + \mathbf{A}^{i}\vec{f}^{i}\right). \tag{4.4}$$

In case of ground-based measurements, the information content for the inversion of trace gas profiles is too small, leading to undetermined, oscillating profiles. To eliminate this ambiguity, additional conditions are imposed, which is called regularization. Within this work, the inversion program PROFFIT [Hase et al., 2004] is used to derive vertical gas profiles. It provides the opportunity to choose between two ways of regularization: optimal estimation [Rodgers, 1976] and the Tikhonov-Phillips method [Tikhonov, 1963] [Phillips, 1962], where only the latter one was applied in this thesis and will therefore be described further.
In this method two additional constraints of the form $\mathbf{B}\vec{S}=\mathbf{B}\vec{f_0}$ can be imposed where the term

$$\left|\Delta\vec{S}\right|^2 + \gamma^2\left|\mathbf{B}\left(\vec{f} - \vec{f_0}\right)\right|^2 \tag{4.5}$$

should be minimized. The second part of Equation 4.5 $\left|\mathbf{B}\left(\vec{f} - \vec{f_0}\right)\right|^2$ is weighted with the regularization parameter γ, which can take values between 0 and ∞. In analogy

to (4.4) the linear solution is given by:

$$\vec{f}^{i+1} = \left(\mathbf{A}^{i,T}\mathbf{A}^{i} + \gamma^2\mathbf{B}^T\mathbf{B}\right)^{-1}\left[\mathbf{A}^{i,T}\left(\Delta\vec{S}^{i} + \mathbf{A}^{i}\vec{f}^{i}\right) + \gamma^2\mathbf{B}^T\mathbf{B}\vec{f}_0\right]. \tag{4.6}$$

The regularization parameter has to be chosen in such a way that the regularization is strong enough to avoid unrealistic effects in the determined profile without increasing the residuals.
The appropriate vertical resolution can be described by the resolution matrix $\mathbf{R}$:

$$\mathbf{R} = \left(\mathbf{A}^T\mathbf{A} + \gamma^2\mathbf{B}^T\mathbf{B}\right)^{-1}\mathbf{A}^T\mathbf{A}, \tag{4.7}$$

where the number of degrees of freedom can be determined by the trace of the matrix. PROFFIT allows to choose between an inversion procedure on a linear or a logarithmic scale, where the latter one avoids negative values for the volume mixing ratio. Additionally there is the possibility to do a scaling retrieval in which a given start profile is simply scaled.

4.2 Retrieval software

The most common retrieval programs used for the detection of atmospheric absorption spectra from ground-based measurements are GFIT, SFIT2 and PROFFIT. While GFIT (e.g. Yang et al. [2005]) is the official retrieval code for the analysis of NIR spectra within TCCON, SFIT2 [Rinsland et al., 1998] and PROFFIT are the two codes used for the retrieval of MIR measurements in the NDACC. In this work, PROFFIT is utilized for the analysis of NIR spectra. Since an important part of this thesis is the intercomparison between GFIT and PROFFIT, these retrieval codes are described in more detail.
GFIT and PROFFIT are nonlinear least squares fitting algorithms used to analyze solar absorption spectra on the basis of inversion methods. GFIT was developed by G. Toon at the California Institute of Technology and PROFFIT by F. Hase at KIT. For both codes it is possible to retrieve total column amounts of a variety of gases in different spectral regions simultaneously. In addition to the scaling of the implemented a priori profile (scaling retrieval) which is performed by both codes, PROFFIT is also able to retrieve the vertical gas profile (profile retrieval). Concerning the profile retrieval within PROFFIT it is possible to choose between optimal estimation and the Tikhonov-Phillips method, where for both options an inversion of a linear or a logarithmic scale is provided. More details about PROFFIT can be found in Hase [2000] and Hase et al.

[2004], while the GFIT code is described in Wunch et al. [2011] and Yang et al. [2005].

4.3 Spectral windows

Within the framework of TCCON, the IMK-related sites Izaña and Karlsruhe provide continuous FTIR measurements in the NIR spectral region. On the basis of these measurements, total column amounts of the gases CO_2, CH_4, CO, N_2O, H_2O, HF, HCl, HDO and O_2 are determined. This thesis focuses on retrievals of CO_2. The spectral windows of CO_2 and O_2 are presented below, which are used for the analysis in PROFFIT and GFIT. Those microwindows correspond to the common TCCON analysis, where O_2 is used as an internal network standard to reduce systematic errors.

4.3.1 CO_2

For the analysis of CO_2, two microwindows at 6180–6260 cm^{-1} (Figure 4.1) and 6310–6380 cm^{-1} (Figure 4.2) containing different CO_2 combination bands were used. As interfering species H_2O, HDO and CH_4 need to be considered. The retrieved total column is the mean of the simultaneously analyzed results of each microwindow.

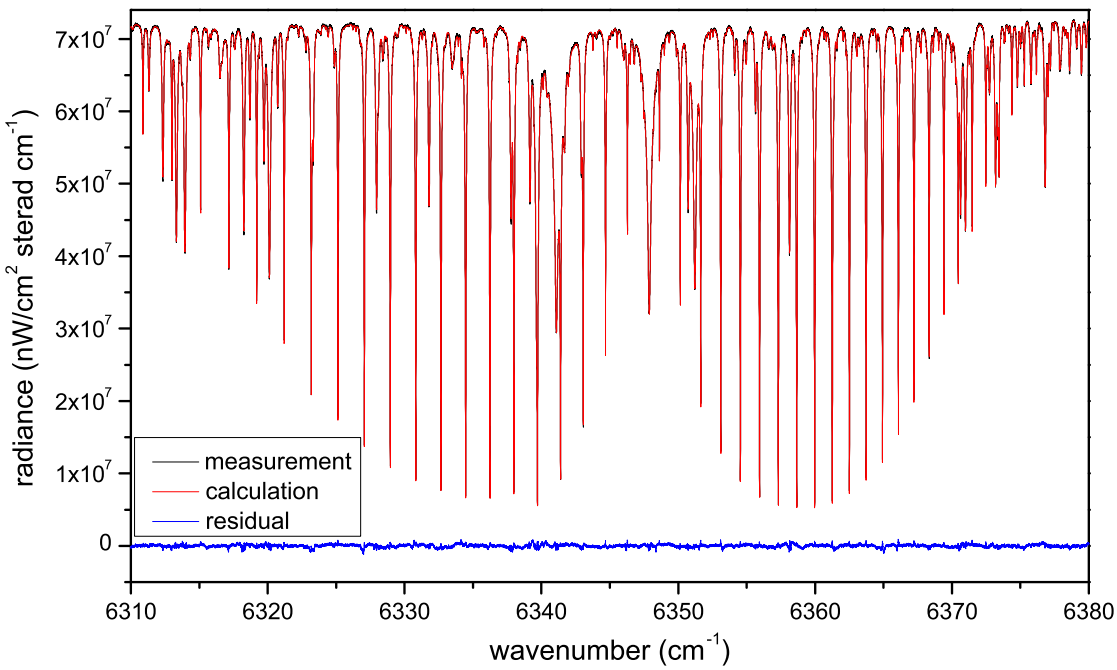

Figure 4.1: One of the CO_2 microwindows (6310–6380 cm^{-1}) used for TCCON data analysis. The measured spectrum is shown in black, the fitted spectrum in red and the residual in blue.

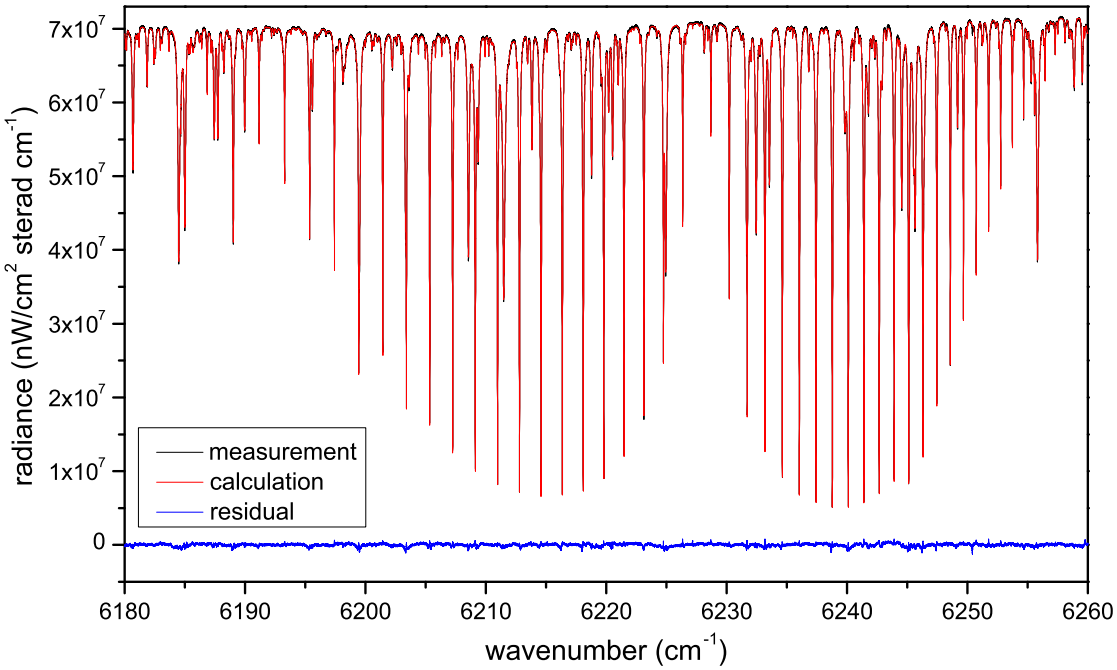

Figure 4.2: Second TCCON microwindow (6180–6260 cm^{-1}) of CO_2 used within this work. The measured spectrum is shown in black, the fitted spectrum in red and the residual in blue.

4.3.2 O_2

As absorption of IR radiation is only possible if molecules have the ability to change their dipole moment during transition, homonuclear diatomic molecules like O_2 or N_2 should not possess rotational-vibrational absorption features in the NIR region. However this is not the case, due to the appearance of several O_2 absorption bands in this region, where the one at 7765–8005 cm^{-1} is used within the TCCON as an internal network standard. It is caused on the one hand by magnetic dipole and electric quadrupole transitions between the ground state ($X^3 \sum_g^-(0,0)$) and the $a^1\Delta g$ state, and on the other hand by collision induced absorption (CIA) [Spiering and van der Zande, 2012]. There are a couple of reasons preferring this band ($a^1\Delta g$-$X^3 \sum_g^-(0,0)$) compared to the more prominent O_2 A-band ($b^1 \sum_g^+$-$X^3 \sum_g^-(0,0)$). One reason is that the O_2 A-band contains much stronger absorption features than the target trace gas signatures, which would lead to systematic errors [Wunch et al., 2011]. The other main absorbers in this microwindow are H_2O and CO_2.

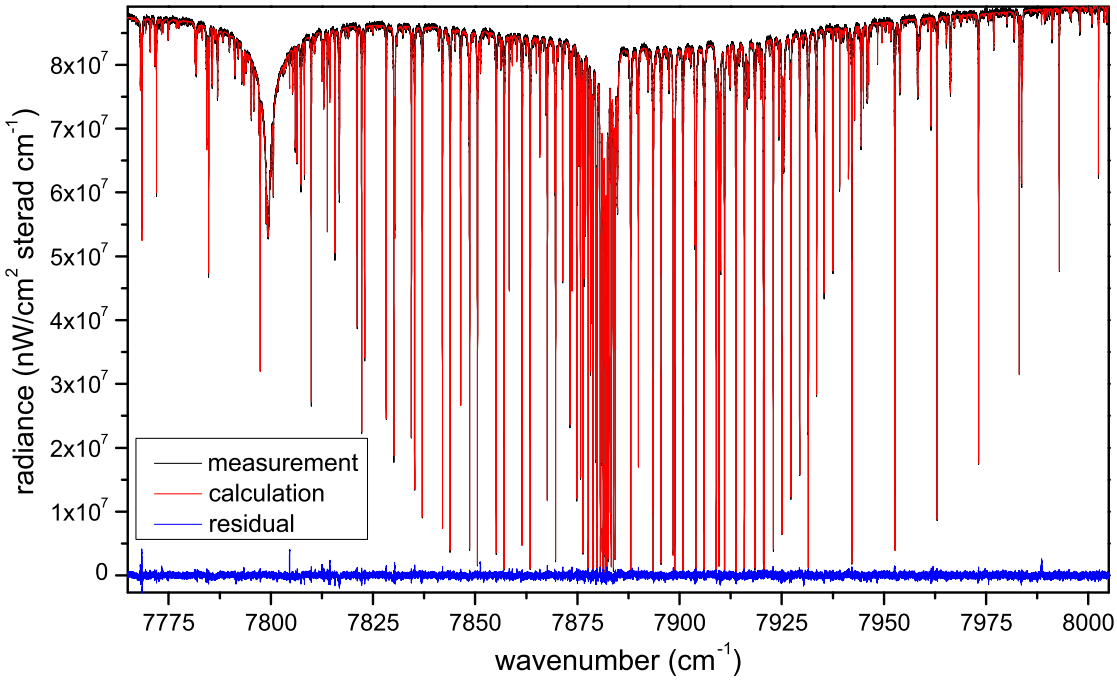

Figure 4.3: O_2 microwindow (7765–8005 cm^{-1}) used within TCCON as an internal network standard. the measured spectrum is shown in black, the fitted spectrum in red and the residual in blue.

4.4 Error sources

The ambition to increase the accuracy of retrieved total column abundances of GHGs needs a strict characterization and reduction of errors. Both systematical and statistical error sources have to be considered while analyzing spectra to prevent erroneous trace gas retrieval results. In this section, an overview of several error sources and their reduction is given.

Spectral noise

The spectral noise leads to errors in the retrieved trace gas concentration. Considering a scaling retrieval the error due to spectral noise E_{SN} can be described with:

$$E_{SN} = \frac{\sigma}{S_0\sqrt{N}}, \tag{4.8}$$

where N is the number of independent spectral grid points within the half width of the spectral line, S_0 the depth of the absorption line and σ the standard deviation of the spectral noise [Hase, 2000]. For CO_2 and O_2 typical values of E_{SN} are in

the region of 0.03%.

Detector nonlinearity

An y-axis offset is usually due to nonlinearity of the detector [Abrams et al., 1994]. The resultant error is given by:

$$E_{OF} = \frac{1}{1 - \frac{\Delta S}{S}}, \tag{4.9}$$

where the ratio $\frac{\Delta S}{S}$ determines the offset in relation to the continuum [Hase, 2000]. For measurements in the NIR spectral region (like in the present work), InSb and InGaAs detectors were used. These detectors work in the linear regime so that E_{OF} can be neglected.

Solar zenith angle

Another important error source is the solar zenith angle (SZA), which has to be well known to determine the air mass between the light source (Sun) and the spectrometer. Considering a tracking range of 0°–80°, the air mass changes by up to 9.6% per degree SZA change. To achieve a total column accuracy of 0.05%, the tracking must have a precision of at least 19 arcsec [Gisi et al., 2011].
Usually there are three reasons leading to erroneous SZAs:

- the suntracker does not track the center of the Sun exactly
- the supposed measurement time differs from the real one due to averaging of spectra.
- the supposed measurement time differs from the real one due to measurement errors.

Concerning the first reason, the camera based system Camtracker [Gisi et al., 2011] was implemented, leading to an increased tracking accuracy (-0.3±0.3 arc s) compared to the formerly used quadrant diode. Regarding the timing error, the measurement duration should not be larger than 3 minutes for sites near the equator, and not larger than 6 minutes for mid-latitude sites. For Karlsruhe NIR spectra, the timing error does not exceed 0.05%.

Instrumental line shape

As already mentioned in Section 3.2, the ILS also leads to uncertainties in the retrieval results. For the Bruker 125HR, which is exclusively used for all TCCON measurements, an ideal ILS is assumed. Nevertheless the ILS is frequently monitored and analyzed via gas cell measurements and the LINEFIT software. Following Hase et al. [2013], a 4% modulation efficiency amplitude change at OPD_{max} leads to a resulting error in the standard TCCON product X_{CO_2} of about 0.035%.

Temperature and pressure profiles

In order to achieve the required high total column accuracy, it is important to know the specific atmospheric pressure and temperature profile (pT profile) for each measurement. Within the common TCCON analysis, model data provided by the National Center for Environmental Prediction (NCEP) are used. NCEP data is available up to 45 km. Above, the US standard atmosphere is used (US-76).
Incorrect temperature profiles lead to errors in the resulting volume mixing ratios due to the temperature dependence of the spectral signatures. Especially in the case of profile retrievals, these errors are non-negligible (see Section 8.4). Concerning the error in temperature, ±1 K is assumed for the troposphere, ±2 K for the stratosphere and above up to ±5 K.
By default, one temperature and pressure profile is used per day within the PROFFIT analysis. Since Gisi [2012] showed that an application of several pT profiles within one day reduces the erroneous intraday decrease in O_2 from 2% to 0.1%, the use of these variable profiles is preferable.

Interfering species

In general, it is hard to evaluate the impact of interfering species on the retrieval due to their unknown vertical distributions and errors in their spectroscopic data. By considering these species as well as solar features within the analysis, errors are minimized. Even the negligence of interfering species leads to only small errors in O_2 (0.47%) and CO_2 (0.005%). Regarding the uncertainties in the solar linelist (see Section 7.7), the resulting error in X_{CO_2} is estimated to be in the order of 0.05%.

Spectroscopic data of target species

The spectroscopic line list used within the analysis is derived from lab measurements, which also include errors. In the present case, modified HITRAN 2008/2009 line lists are used for the retrievals [Rothman et al., 2009]. Errors of the CO_2 air-broadening widths, which were in the order of 3%, have been corrected within this work (see Section 7.1). The resulting error in the retrieved total column corresponds to the accuracy of the line strength, depending on the gas and its spectral signature.

Source intensity variations

For ground-based measurements, clear sky days without any variations of solar intensity are an exception. In the presence of clouds, the interferogram's amplitude is reduced, leading to a distortion of the spectrum and therefore erroneous gas retrieval results. With the help of the so called DC-correction, these effects can be corrected [Keppel-Aleks et al., 2007]. This highly efficient correction scheme is described in more detail by Gisi [2012] and gives rise to a reduced scattering in gas retrieval results by a factor of 10.

Periodic sampling errors

Errors in interferogram sampling can introduce significant biases in the resulting trace gas retrievals. As the correction of these sampling errors is a main component of this Ph.D. thesis, their origin and effects will be described in more detail.
Interferograms recorded with FTIR spectrometers need to be sampled very accurately as a function of optical path difference to avoid artificial spectral lines (ghosts) after FT. To ensure this precise sampling, a frequency stabilized, single-mode HeNe reference laser is fed into the spectrometer. The zero crossings of the laser interferogram serve as reference for the sampling of the infrared signal. The original measurement signal of the reference laser is actually a cosine oscillation. If the construction of the mean intensity level is erroneous, a sampling error pattern of alternating narrow and wide distances will result (see Figure 4.4).
Following Guelachvili [1981], the spectrum of monochromatic light derived from an interferogram with periodic sampling error ϵ of frequency β and amplitude ϵ_0,

$$\epsilon = \epsilon_0 \sin(2\pi\beta x) \tag{4.10}$$

is given by:

$$B(\sigma) = J_0(2\pi\sigma_0\epsilon_0)\int_0^{x_m} \sin(2\pi\sigma_0\, x)\sin(2\pi\sigma\, x)\; d\,x$$
$$+\sum_{k=1}^{\infty} J_k(2\pi\sigma_0\epsilon_0)\int_0^{x_m}[\sin(2\pi(\sigma_0+k\beta)\,x)$$
$$+(-1)^k\sin(2\pi(\sigma_0-k\beta)\,x)]\sin(2\pi\sigma\, x)\; dx, \tag{4.11}$$

where x is the OPD, σ_0 is the frequency of the incident light and J_k are Bessels functions for integers $k = 1, 2, ..., n$. The $k = 0$ term describes the incident radiation modified by the instrument response function for finite maximum optical path difference x_m. If $\epsilon_0 \neq 0$ the intensity of the parent line is scaled by the factor $J_0 \sin(2\pi\sigma_0\epsilon_0)$ which is less than one. Similar features with intensities proportional to $J_1 \sin(2\pi\sigma_0\epsilon_0)$, $J_2 \sin(2\pi\sigma_0\epsilon_0)$, ... $J_n \sin(2\pi\sigma_0\epsilon_0)$ appear at $\sigma_0 \pm \beta$, $\pm 2\beta$, ..., $\pm n\beta$.
β depends on the sampling rate per laser wavelength, which is determined by the high folding limit for the measurements. In the case of TCCON measurements, the

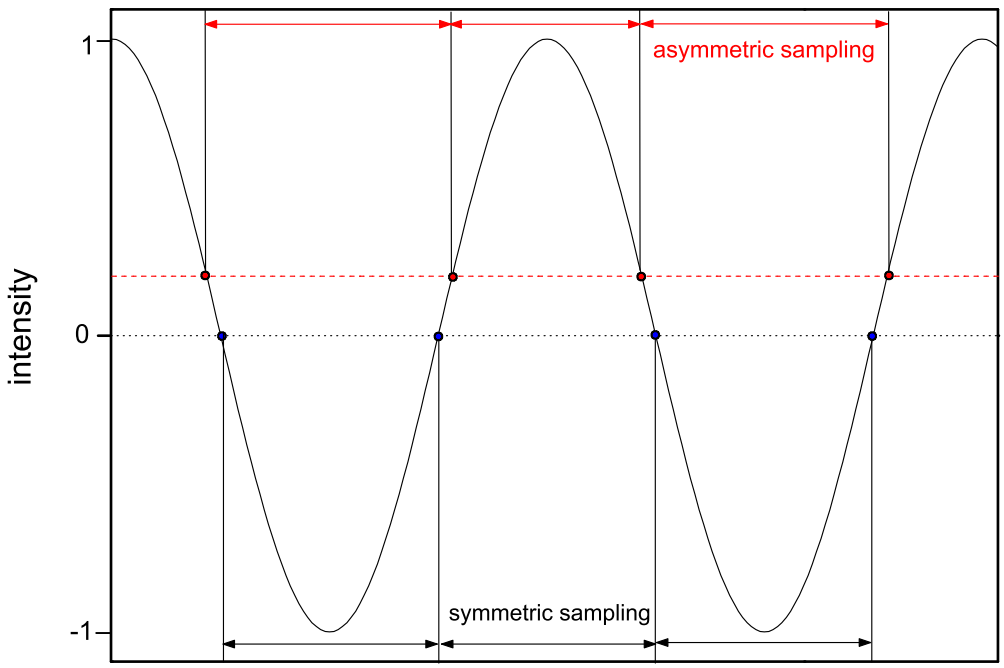

Figure 4.4: An interferogram of the reference laser. The zero crossings are taken as reference for the measurement-sampling which is ideally symmetric (black arrows). Due to an erroneous determination of the mean intensity level, a zero offset occurs, which gives rise to an asymmetric sampling (red arrows). As a consequence phase ghosts arise, which are superimposed to the spectrum. (Taken from Dohe et al. [2013])

HFL is set to 15798 cm^{-1} and the laser interferogram is sampled on every zero crossing. Thus β=15798 cm^{-1} and ghosts occurring at $\sigma_0 \pm 15798$ cm^{-1} are both aliased to 15798-σ_0 cm^{-1}. A schematic illustration of the ghost effect is shown in Figure 4.5.
Note FTIR measurements in the MIR as acquired by the NDACC are not affected by this error. In this spectral region a high folding limit of 7899 cm^{-1} or less is applied. The sampling is performed only at each rising zero crossing of the laser interferogram and an error in the evaluation of the mean laser intensity level does not generate an alternating sampling pattern.
In summary, a periodic sampling error leads to distortions of the true spectrum. Line strengths are modified and the spectrum zero levels become spuriously nonzero. These distortions can and do lead to significant retrieval biases in the case of TCCON measurements. They must be corrected at the source, by resampling the interferograms, which is shown in Chapter 5.

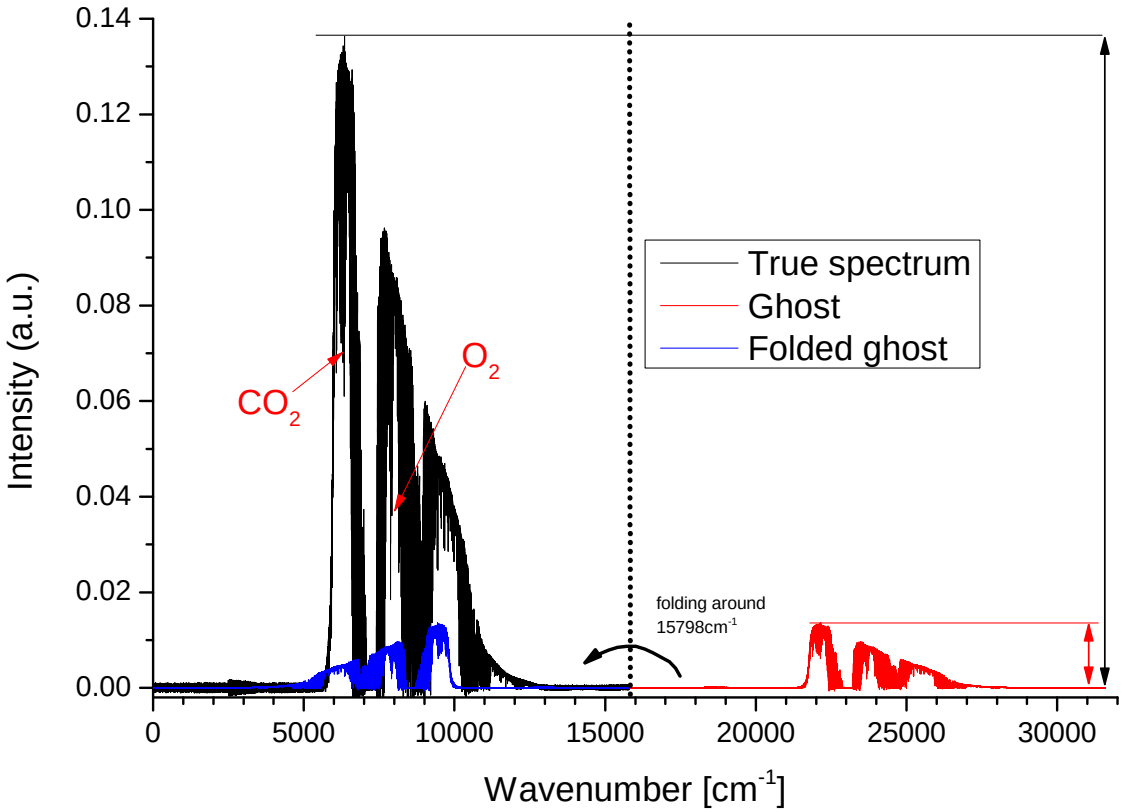

Figure 4.5: Schematic illustration of the ghost effect. Occurent ghosts (red) are folded around 15798 cm^{-1}, leading to a ghost spectrum which is the sum of the folded ghosts (blue) and the true spectrum (black). (Taken from Gisi [2012])

4.5 O_2 as an internal network standard

The ambition of an increasing accuracy of atmospheric total column results necessitates the minimization of the aforementioned error sources. As described before, this is done by applying specific corrections like the DC-correction for solar intensity variations or the characterization of the ILS with the help of gas cell measurements and the software LINEFIT. Another important method to minimize errors will be described within this section, which is the use of O_2 as an internal network standard [Wunch et al., 2011].
The retrieved total column C of the target trace gas Y is converted into the column averaged dry air mole fraction (DMF) by dividing by the total column of dry air C_{dryair}:

$$X_Y = \frac{C_Y}{C_{dryair}}. \tag{4.12}$$

In general, there are two different methods to determine C_{dryair}. The first option is the determination on the basis of the ground pressure p_{gr} and the total column of water C_{H_2O}:

$$C_{dryair} = \frac{p_{gr}}{g \cdot m_{dryair}} - C_{H_2O}\frac{m_{H_2O}}{m_{dryair}}, \tag{4.13}$$

where m is the mean molecular mass and g the gravity acceleration. The other method to determine C_{dryair} is to detect the total column of O_2 and divide by the DMF of O_2 which is assumed to be constant:

$$C_{dryair} = \frac{C_{O_2}}{0.2095}. \tag{4.14}$$

The latter option of determining C_{dryair} is used within this thesis because of its advantages compared to the other method. The most important one is that systematic errors which are common to target and O_2 column retrievals (e.g. tracker pointing errors, ILS errors, zero level offsets) are compensated in this ratio.
By combining Equations 4.12 and 4.14, the DMF can be described with:

$$X_Y = 0.2095\frac{C_Y}{C_{O_2}}. \tag{4.15}$$

An important error which cannot be corrected within this method is the sampling error of the interferogram. Because the laser sampling error (LSE) is more pronounced for O_2 than for other gases, it does not cancel out in X_Y. Therefore it is important to apply an additional correction of the LSE, which is described in the following chapter.

Chapter 5

Correction of sampling ghosts

As already described in Chapter 4, we are concerned with an error source which is of special relevance for NIR FTIR measurements, namely periodic errors in the x-axis locations where the interferogram is discretely sampled. As a result of missampling, a fraction of the input spectral signal is assigned to an incorrect frequency, generating a ghost spectrum, which can overlap with and perturb the original spectrum, leading to errors in retrieved column abundances.

Messerschmidt et al. [2010] showed that the interferogram sampling in earlier versions of the Bruker 125HR laser sampling board does not control ghost amplitudes in the NIR to the level of accuracy required for TCCON work. Typical magnitudes of the errors in X_{CO_2} and O_2 column retrievals encountered in practice are 0.1-0.5%, corresponding to 0.3–2 ppm for X_{CO_2} [Messerschmidt et al., 2010] [Messerschmidt et al., 2011]. The FTIR spectrometer manufacturer Bruker Optics (Ettlingen, Germany) subsequently developed an improved laser sampling unit which offers the accuracy required by TCCON, and which has been installed in 2010/2011 in all TCCON spectrometers. However, the post-correction of historic TCCON measurements still remains a particular problem, because the laser sampling error varies from instrument to instrument and is also expected to change through time (e.g. on instrument intervention, change in measurement sample rate or laser power/amplitude changes) at any given site. Messerschmidt et al. [2010] proposed an empirical ghost correction scheme which is based on (1) the determination of the ghost-to-parent intensity ratio (GPR) using narrowband lamp spectra and (2) an empirical determination of the variation of the column-averaged DMF X_Y of the target gas Y as a function of the GPR. However, there are several reasons the scheme described by Messerschmidt et al. [2010] cannot be applied satisfactorily in practice to historical TCCON time series. Firstly, the retrieval bias depends on the sign and magnitude of the sampling error, but only the latter can

be determined from the lamp GPR measurement. Secondly, a site-independent relationship between X_Y and GPR cannot generally be assumed, due to differences in the instrument spectral response and/or differences in the absorber line-of-sight (LOS) abundances (which impact both the magnitude of the aliased ghost signatures and the retrieval sensitivity to these artifacts). Thirdly, no TCCON site has a set of narrow-band filter lamp spectra acquired through time which would enable changes in the sampling error on instrument intervention to be adequately characterized (even if the sign of the sampling error and the retrieval sensitivity could be adequately determined).
This chapter is about the ghost correction of historic measurements, where parts of the chapter have been adopted from the publication of Dohe et al. [2013]. Concerning the IMK-related TCCON sites Izaña and Karlsruhe, only the early Izaña measurements (2007-2011) are affected by ghosts. The Karlsruhe FTIR spectrometer was installed in 2010 and shows only negligible ghost effects. Therefore the developed correction methods are demonstrated using time series of measurements acquired at the Izaña TCCON site.
The following section describes the instrumentation and instrument history of the Izaña Bruker 125HR. Section 5.2 deals with an empirical post-correction while Section 5.3 introduces the developed fundamental ghost correction scheme for TCCON in more detail, which includes the quantification of the LSE and the resampling of the interferogram. Section 5.4 concludes the study.

5.1 Instrumentation at Izaña

The Izaña TCCON measurements are acquired with the Bruker 125HR spectrometer, using a DC-enabled room temperature InGaAs detector with a resolution of 0.02 cm^{-1} (OPD$_{max}$=45 cm) and a high folding limit of 15798 cm^{-1}. Izaña NIR interferograms are recorded using the Optics User Software (OPUS) version 6.5 provided by Bruker. Izaña datasets presented in this chapter have been analyzed in a self-consistent manner using software developed at KIT by F. Hase, M. Gisi and M. Schneider to determine the sampling error (ghost4.exe) and resample and transform interferograms to spectra. Retrievals were performed with the PROFFIT software.
An overview of the Izaña instrument history is given in Table 5.1. At installation (January 2005) the spectrometer had the original ECL02 laser board, where the LSE could not be minimized and was a function of sample rate (scanner velocity). In June 2008 the instrument was realigned and the interferogram recording mode was changed from AC to DC. The electrical low-pass filter was changed in March 2009. In November

Date	Intervention
January 2005	Installation of the Bruker 125HR with ECL02
June 2008	Realignment and recording mode change from AC to DC
March 2009	Change of electrical low-pass filter setting
November 2009	Installation of ECL03 and optical long-pass filter
January–March 2010	Very cold temperatures inside the container and loss of power
May 2010	Change of electrical low-pass filter setting
November 2010	Installation of ECL04, realignment

Table 5.1: The Izaña instrument history with important interventions from January 2005 to November 2010.

2009 the laser board was replaced by an ECL03 board (LSE was minimized at 40 kHz) and an optical long-pass filter was installed. At version ECL03 a potentiometer was introduced enabling the LSE to be minimized for a given sample rate (sampling errors at other sample rates remained significant). After some problems due to loss of power, very cold temperatures inside the container (January–March 2010) and the change of the electrical low-pass filter (May 2010), the new ECL04 laser board and v02 diodes were installed in November 2010 and the LSE was eliminated for all practical purposes in routine TCCON measurements. The interferometer was also realigned at this time. All Izaña measurements in the considered period were acquired with a 40 kHz sample rate.

5.2 Empirical ghost correction

As already mentioned in this chapter, the Izaña measurements which were recorded before the laser board exchange in 2010 are affected by ghosts and need to be corrected. The empirical ghost correction proposed by Messerschmidt et al. [2010] is not applicable, because there is no set of narrow band lamp spectra available at Izaña. However, to provide a usable dataset without ghost effects, an empirical ghost correction has been developed within this work.

In this method, the retrieved total column amounts undergo a correction whereas in the fundamental TCCON ghost correction (see Section 5.3) the error is minimized at its origin (which is the interferogram). First of all the amount of missampling for each measurement has to be determined. This can be done by regarding the ratio of the O_2 column (C_{O_2}) and the ground pressure (p_{gr}), where usually the H_2O column also has

to be taken into account. For Izaña the atmospheric H_2O content is negligible because of the site's high altitude. In the absence of ghosts, the ratio is expected to be constant with time, due to the correlation between C_{O_2} and p_{gr}. In the presence of LSEs, the records of retrieved C_{O_2} are biased, whereas p_{gr} remains unaffected. This leads to stepwise changes in C_{O_2}/p_{gr} with time due to instrumental interventions. Other measurement and retrieval error sources (timing errors, pointing errors and ILS) can introduce changes in C_{O_2}/p_{gr} as well, so C_{O_2}/p_{gr} can only be utilized to characterize the LSE history if these other factors are controlled well enough. Significant effort has been invested at Izaña to ensure a high degree of instrumental stability, including the development of the camera controlled high precision solar tracker system Camtracker, and regular monitoring of the ILS by LINEFIT analysis of low pressure HCl, HBr, and N_2O cell spectra.

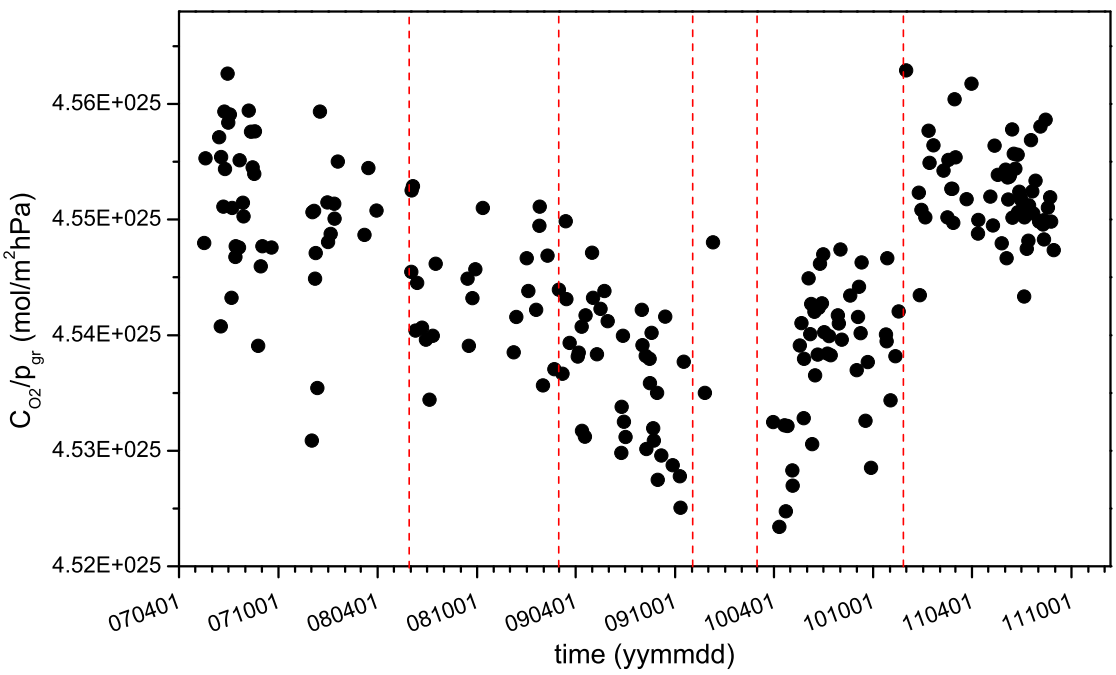

Figure 5.1: Izaña 125HR time series of daily mean C_{O_2}/p_{gr} from 2007 to 2011 for uncorrected measurements. The beginning of new sub-periods due to instrumental interventions or breakdowns (see Table 5.1) are indicated with red vertical dashed lines.

The C_{O_2}/p_{gr} time series for the Izaña 125HR from May 2007 to September 2011 is illustrated in Figure 5.1. The LSE is assumed to be stable on shorter timescales and jumps occur only on instrument interventions (e.g. realignments, electrical low-pass filter change; see Table 5.1), which are indicated with vertical red dashed lines. The

time series shows six individual periods with different C_{O_2}/p_{gr} attributed to instrument interventions, where the values of the last period (December 2010–September 2011) are assumed to be ghost free due to the laser board exchange at the end of 2010.
In order to correct the data, different part wise correction factors are applied, leading to a nearly constant time series of C_{O_2}/p_{gr}. To determine the values of these factors, the mean of C_{O_2}/p_{gr} for each period is compared to the mean of the last part, which is assumed to be true. At the end the detected values of the correction factors are applied to the respective periods.
The results of the empirical ghost correction for Izaña are shown in Figure 5.2. The corrected time series of C_{O_2}/p_{gr} is nearly constant, where the value of C_{O_2}/p_{gr} is increased by up to 0.5%, which will also implicate effects in X_{CO_2}.
In summary this method leads to a reduction of the LSE effect and an increasing accuracy of the data compared to the raw, erroneous data. However, within this method the LSE is only estimated with an insufficient accuracy for TCCON requirements. Therefore another more fundamental ghost correction scheme is required, correcting the error at its source. This fundamental TCCON ghost correction, which is a main part of this work, is described more detailed in the following section.

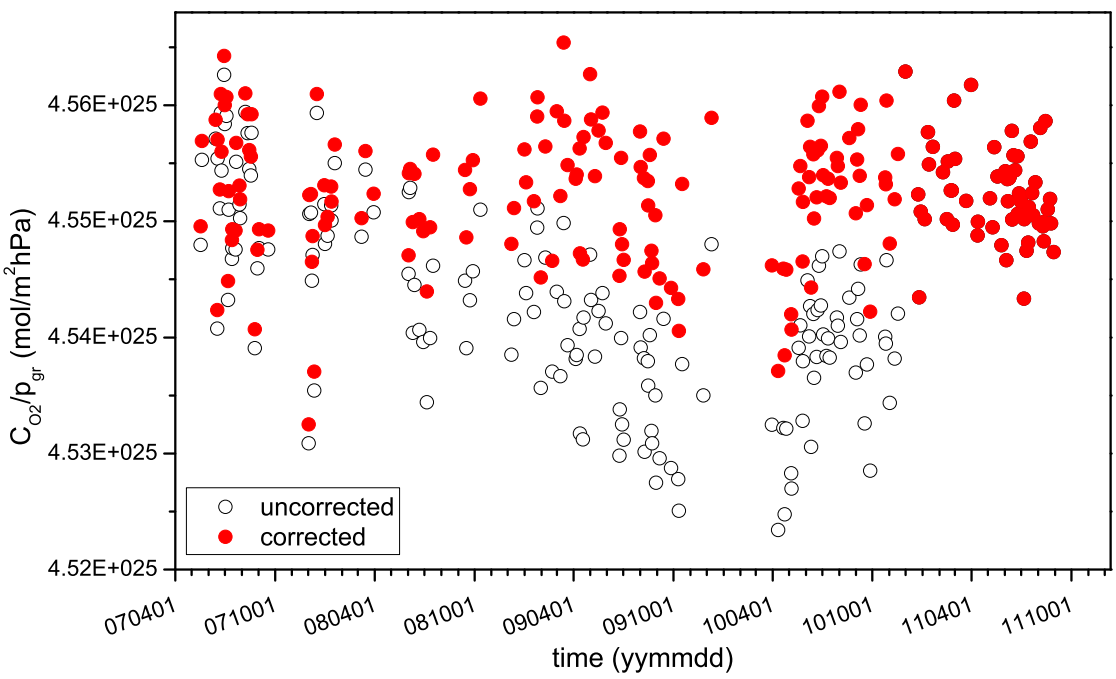

Figure 5.2: Izaña 125HR time series of daily mean C_{O_2}/p_{gr} from 2007 to 2011 for uncorrected (black rings) and corrected (red dots) data. After correction, the time series is nearly constant, where C_{O_2}/p_{gr} increased by up to 0.5%.

5.3 Fundamental TCCON ghost correction

The fundamental TCCON ghost correction procedure [Dohe et al., 2013], was developed at KIT in collaboration with the National Institute of Water and Atmospheric Research in New Zealand and consists of two steps: the quantification of the sampling error (Section 5.3.1) and the correction of the sampling error by resampling the interferogram (Section 5.3.2).

5.3.1 Quantification of the sampling error

Interferogram resampling

In the interferogram resampling method we seek to determine the sampling shift which minimizes the magnitude of the signal intensity in selected, fully absorbed regions of the solar spectrum. In this study we use the 7290–7360 cm^{-1} interval in most of the cases, which is shown in Figure 5.3.

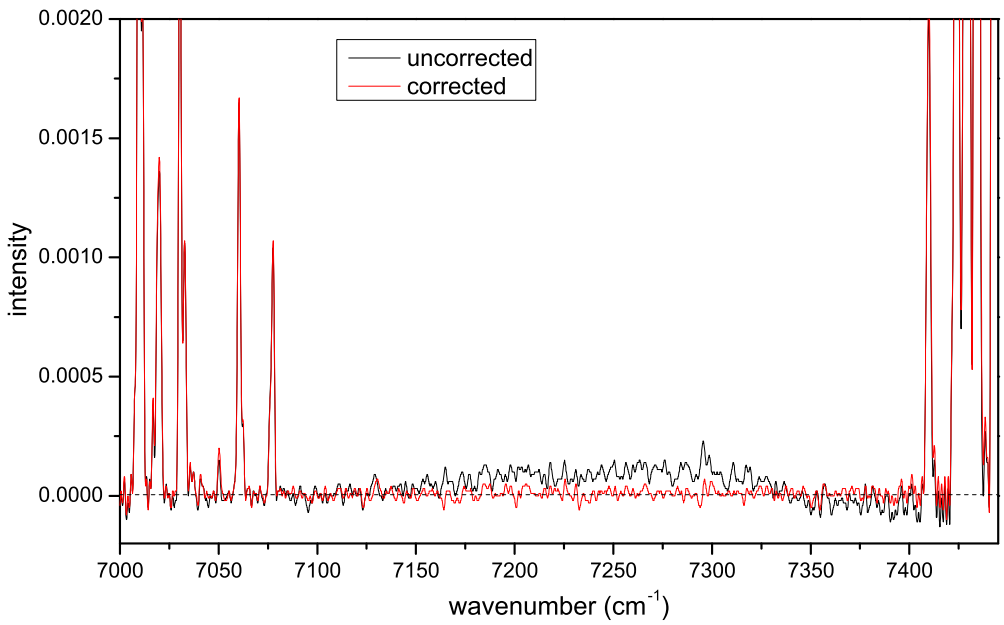

Figure 5.3: The opaque region of the solar spectrum between 7290 and 7360 cm^{-1} used in the resampling analysis. The mean intensity in the modulus spectrum is reduced when the ghost correction is applied (black: uncorrected, red: corrected). (Taken from Dohe et al. [2013])

It is essentially opaque for slant H_2O column abundance of $>5 \cdot 10^{22}$ molecules/cm^2 (generally satisfied at large solar zenith angles) and the associated aliased ghost interval

at 8440–8510 cm^{-1} (HFL=15798 cm^{-1}) has appreciable signal levels. Izaña is unique among the TCCON sites due to its high altitude, and often the 7290–7360 cm^{-1} microwindow is not saturated. Therefore a second microwindow (10900–11300 cm^{-1}) is used in addition to the 7290–7360 cm^{-1} one to determine the LSE time series. The common Izaña measurement procedure is the recording of three single-sided forward and reverse scans, which are averaged after FT. The sampling error is determined using the double-sided interferogram section around the center burst. A set of probable sampling errors Δx_i is defined. For each Δx_i the odd sample points of the interferogram are shifted and the interferogram is interpolated to the shifted sample locations using a sinc-interpolation. The FT of the resampled interferogram is then taken and the mean absolute signal intensity ($\sum |B(\sigma)|$) in the selected spectral window (7290–7360 cm^{-1} or 10900–11300 cm^{-1}) is evaluated. The signal intensity is tabulated as a function of Δx, and the shift which minimizes the mean absolute signal intensity is the LSE used subsequently to correct the full interferogram. The procedure is performed separately for the forward and reverse scans to allow for differences in magnitude as well as in sign between LSE of the two scan directions. Example output from a resampling test for the 7290–7360 cm^{-1} microwindow is shown in Figure 5.4. Here and throughout this thesis, the sampling error is expressed as a fraction of the sampling interval.

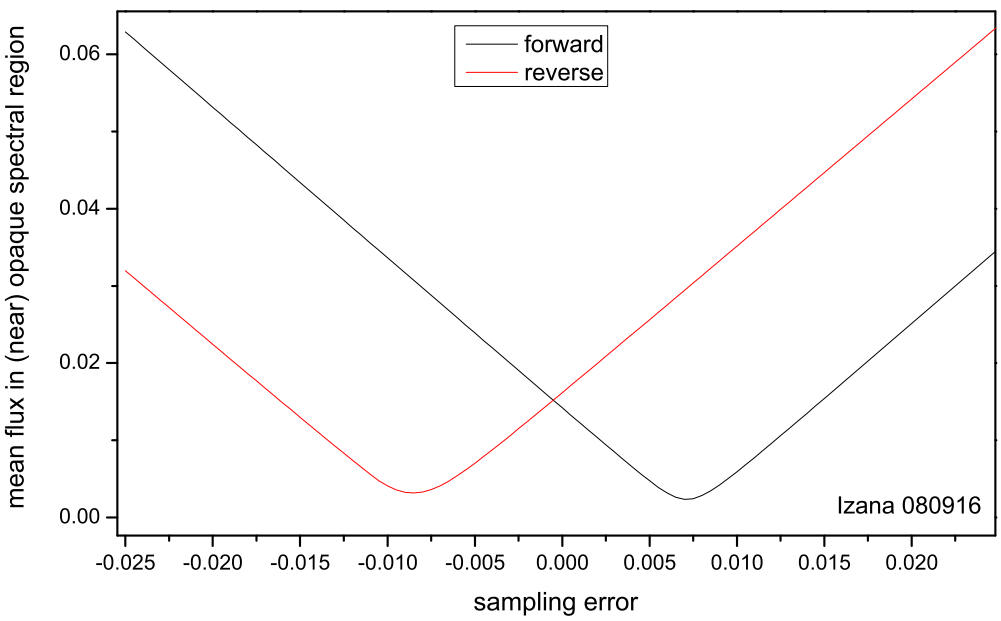

Figure 5.4: The mean flux in the (near) opaque spectral region for the spectral window 7290-7360 cm^{-1} as a function of LSE. The scanner velocity of v=40 kHz introduces a significant missampling for forward and reverse scans. (Taken from Dohe et al. [2013])

As noted above, the interferogram sampling points are classified into even and odd points. The phase of the laser interferogram changes by π with a one point indexing shift, and the inferred LSE is of opposite sign. The classification or indexing used to derive the LSE must therefore be consistent with the indexing used when applying the LSE to correct interferograms. Although the laser fringe counting of the Bruker spectrometer is performed in quadrature and therefore assures that the sampling number of a physical point is conserved, this assignment is lost during re-initialization of the scanner or if the spectrometer is switched off. On the other hand, the true physical location of the infrared beam zero path difference (ZPD) constructive interference maxima (center burst peak) and the phase of the laser interferogram are expected to remain constant through scanner reinitialization etc. For this reason, it is preferable for our purpose to reference the sample indexing to the center burst peak position. However, the center burst of a real interferogram is not perfectly symmetric. The shapes of forward and backward center bursts differ due to small time delays between IR and laser signal processing chains which depend on scanner speed, optical bandpass and electrical filter settings. So it can happen that the even/odd referencing differs for forward and reverse scans and may switch upon instrumental intervention.

In its current implementation the resampling LSE estimate is based on the minimization of the mean absolute signal intensity in an opaque section of the atmospheric spectrum. This assumes that detector nonlinearity is negligible or has been corrected prior to the LSE estimation procedure. The current implementation also assumes that the LSE determined at the position around the interferogram center bursts are representative for the whole high-resolution interferogram. This assumption is probably not fully verified, so some high-resolution artifacts of the original ghosts might still exist. However, it would be difficult to characterize these tiny artifacts and to use them for an improved correction scheme (in which the LSE would become a function of optical path difference), because the offset introduced by the ghosts is significantly lower than the noise level of the high-resolution spectrum.

One known source of short term variability in the LSE is not addressed by the current implementation of the resampling methodology: the LSE can vary at very low pressure (<0.5 hPa) due to heating of the electronic components of the laser board (ECL03; Sussmann et al. [2011]). In this case, the LSE must be determined at higher temporal resolution if possible. Where this is not possible, affected historical data should not be used for TCCON analysis, or should be flagged as ghost affected. The temperature dependence of the LSE can be neglected for measurements at the IMK-related sites Izaña and Karlsruhe, where spectrometers are operated at ambient pressure.

Derivation of the LSE time series

In order to establish a time series of LSE estimates for a given site, we assume that the LSE is stable or slowly varying on timescales of days to weeks, but allow for possible, discontinuous changes in the LSE during instrument intervention (depending on the nature of the intervention). Interferograms are selected which were acquired in cloud free conditions at large solar zenith angles to ensure the optical opacity of the chosen microwindow. In the case of Izaña, 28 days with clear sky conditions were selected. For every day, measurements with large SZA were co-added (co-add sample size $\geq$4 interferograms) and the LSE was determined using the resampling algorithm on co-added interferograms. In the case of only few measurements with large SZA on a single day, measurements of several days were co-added and the same LSE value is reported for each of these days.

Izaña LSE time series

The LSE time series for the Izaña 125HR from September 2008 to October 2011 is illustrated in Figure 5.5, where the LSE of the 40 kHz measurements were determined by using the regions 7290–7360 cm^{-1} (in most of the cases) and 10900–11300 cm^{-1} (the results for these two microwindows are shown with different symbols in Figure 5.5). The beginning of new sub-periods with different LSEs due to instrumental interventions or breakdowns are indicated with vertical dashed lines. The values of the LSE (forward, reverse) are determined from the mean estimated LSE of each period. The first resampling results of the solar data acquired with the original ECL02 laser board from September 2008 to March 2009 show large LSE estimates of about (0.0094, -0.0068). The electrical low-pass filter change in March 2009 did not influence the LSE, whereas the laser board exchange (ECL03 laser board) and red-filter installation in November/December 2009 reduced the LSE to (0.0046, -0.0036). The next stepwise changes in the LSE are evident for instrument interventions due to loss of power and very cold temperatures (<0°C) in the container (January–March 2010) and the electrical low-pass filter change in May 2010. We see a clear contrast between the LSE estimates for the ECL02/ECL03 and ECL04 board, which was installed with v02 diodes in November 2010. Since that installation the magnitude of the LSE has remained at (0.0020, -0.0001), where the residual LSE might be due to perturbations of the zero baseline that we clearly see for forward scans, and changes in interferometer alignment.

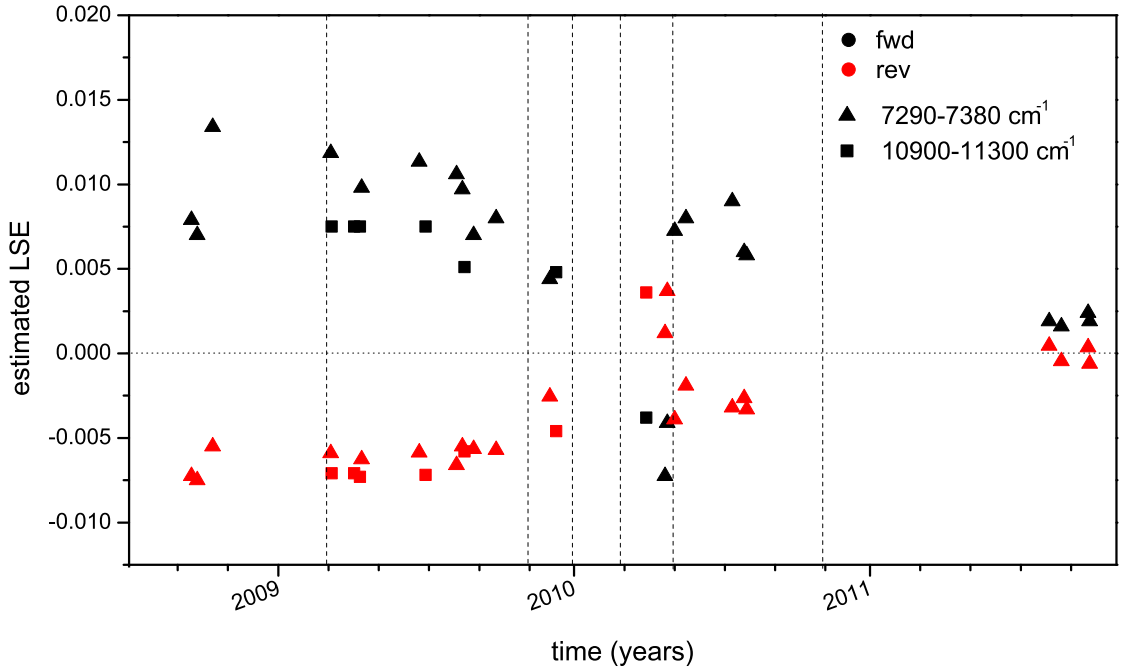

Figure 5.5: Izaña LSE time series from 2008–2011 analyzed using the regions 7290–7360 cm^{-1}(triangles) and 10900-11300 cm^{-1}(squares). Forward (black) and reverse scans (red) vary in magnitude and sign. The beginning of new sub-periods with different LSEs due to instrumental interventions or breakdowns (see Table 5.1) are indicated with vertical dashed lines. (Taken from Dohe et al. [2013])

5.3.2 Correction of the sampling error

The LSE time series is evaluated to define the most suitable temporal description of the LSE to apply to all measurements acquired at the given site. Typically this will be a piecewise linear function with a constant LSE for stable periods between instrument interventions. Each full resolution interferogram is corrected based on the LSE estimate for the given day. The odd sample points of the full resolution interferogram are shifted and the interferogram is resampled using a sinc-interpolation. The resampled interferogram is transformed (FT) and retrievals are performed for the resultant, ghost-corrected spectrum.

Izaña X_{CO_2} and X_{air} time series

To characterize the contribution of O_2 retrieval errors in a way that is readily understood, the variable X_{air} is used within TCCON. X_{air} is the column averaged dry air

mole fraction of dry air and similar to C_{O_2}/p_{gr} (Section 5.2):

$$X_{air} = 0.2095 \frac{C_{dryair}}{C_{O_2}}, \tag{5.1}$$

where the dry air column C_{dryair} in the numerator is derived from an independent co-located measurement of p_{gr}, corrected for the H_2O column overburden if necessary. In the absence of systematic errors, the expected value of X_{air} is 1, and the relative error in X_Y due to O_2 retrieval errors is calculated/given by X_{air}-1. As already mentioned for C_{O_2}/p_{gr} in Section 5.2, stepwise changes in the LSE on instrument intervention introduce discontinuities in X_{air} time series, where it has to be ensured that other measurement and retrieval error sources are controlled well enough.
The Izaña 125HR time series of daily mean X_{air} and X_{CO_2} from 2008 to 2011 acquired at solar zenith angles between 40–60° are illustrated in Figure 5.6 and 5.7.

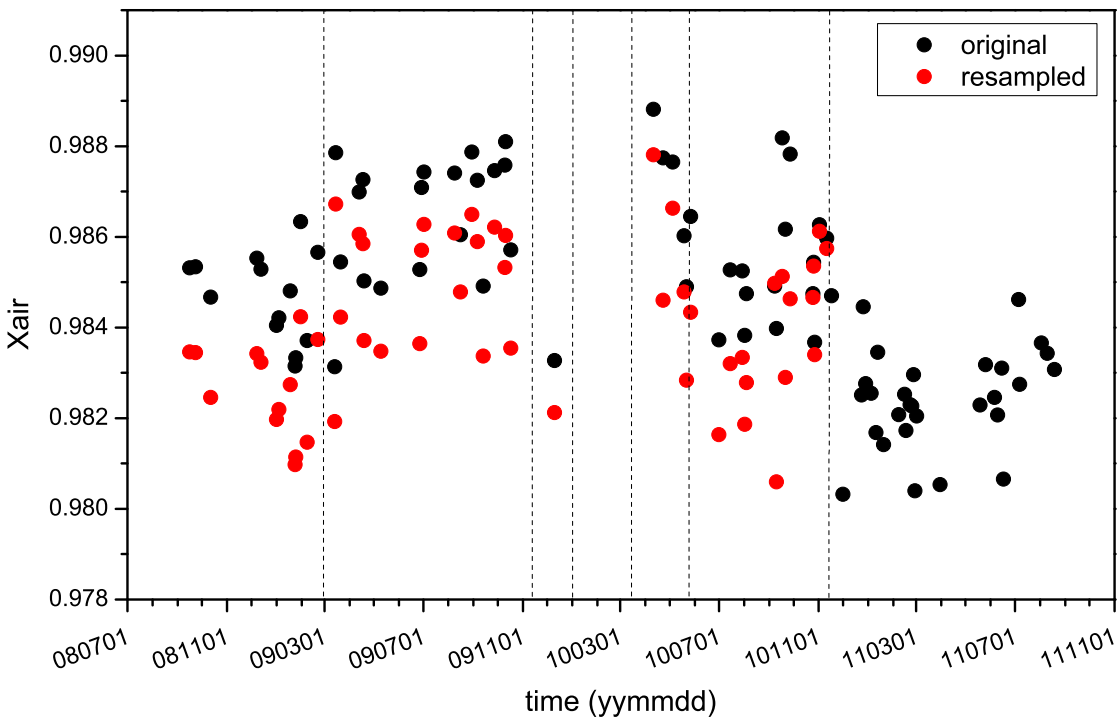

Figure 5.6: Izaña 125HR time series of daily mean X_{air} from 2008 to 2011 for original and resampled measurements. The beginning of new sub-periods with different X_{air} due to instrumental interventions or breakdowns (see Table 5.1) are indicated with vertical dashed lines. (Taken from Dohe et al. [2013])

The resampled measurements are displayed as red dots whereas the black dots show the original measurements. The uncorrected Izaña X_{air} time series in 5.6 shows seven

distinct periods with different mean X_{air}, attributed to intentional modifications on the instrument, e.g. realignment of the interferometer, exchange of reference laser, change of relevant measurement settings and laser board exchange or adjustments. Rarely, in the course of strong storms, prolonged power breakdowns of the whole container occurred at Izaña which result in very low temperature of the spectrometer. In addition, we find indications for an unexpected high bias of X_{air} during the period before September 2008 (not shown), which needs to be investigated further. In the end of 2010, the new ECL04 Bruker laser sampling unit was installed, which introduced a significant 0.35% reduction of X_{air}. Henceforward, it is assumed that these measurements are free of ghosts and provide a reference X_{air} value.
By the use of resampled data, this difference is reduced from 0.5% to 0.2%. The remaining discrepancies are attributed to changes in interferometer alignment. In addition there is a discontinuity for the resampled measurements between March 2009 and May 2010. This might be due to changes of the electrical low-pass filter settings in this period but has to be investigated further. Note, that in the interferogram pre-

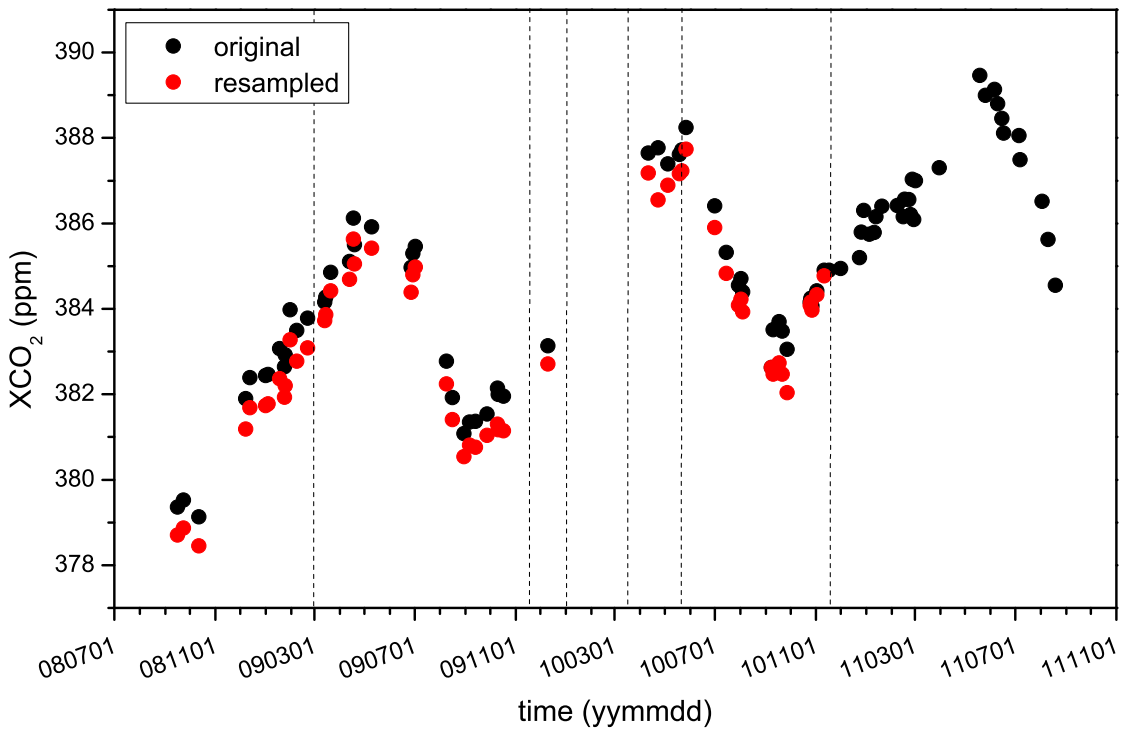

Figure 5.7: Izaña 125HR time series of daily mean X_{CO_2} from 2008 to 2011 for original and resampled measurements. The beginning of new sub-periods due to instrumental interventions or breakdowns (see Table 5.1) are indicated with vertical dashed lines. (Taken from Dohe et al. [2013])

processing the forward and reverse scans are corrected for their respective sampling errors, transformed and then coadded to generate one spectrum per forward/reverse pair.
The X_{CO_2} time series shows a reduction of X_{CO_2} for resampled measurements. As mentioned before, most of this difference is due to changes in the O_2 retrieval (>75%). For measurements at the beginning of the time series in 2008, the difference between retrievals from uncorrected and resampled spectra is about 0.2%. Smaller differences (0.03%) are found in the period before the laser board exchange in 2010.

5.4 Conclusions

Many TCCON sites worldwide recorded ghost affected interferograms for many years, leading to errors in the resultant trace gas time series (0.1–0.5% [Messerschmidt et al., 2010] [Messerschmidt et al., 2011]). To assure the high TCCON quality standard, a correction of these sampling errors is necessary, which was presented in this chapter. First, an empirical correction scheme on the basis of C_{O_2}/p_{gr} was introduced. By means of the Izaña time series it was shown that the LSE could be minimised with this method. However, errors could not have been adequately corrected for using neither this empirical method nor the empirical method described by Messerschmidt et al. [2010]. Therefore a fundamental two-step correction scheme was developed and demonstrated which enables the LSE history to be characterised through time and which enables LSEs to be corrected at the source, by resampling the interferogram.
The sampling history for Izaña shows clear changes in LSE due to instrument interventions, where similar histories are to be expected at other TCCON sites. As an example, the LSE time series for the TCCON site Lauder, where the procedure was also successfully tested, is shown in Figure 5.8.
Resulting retrieval biases for Izaña are in the range of 0.2–0.5% and are time and site dependent. After resampling, discrepancies due to instrument interventions are reduced to 0.2% at Izaña, where the residual differences are attributed to coincident changes in interferometer alignment.
Although not shown explicitly here, LSEs affect the estimated DMF of other TCCON target gases (CH_4, N_2O, CO) in a similar manner. This is the case because the bias in X_Y for the gases is primarily driven by the bias in the O_2 column, as it is for X_{CO_2}.
The aim of the TCCON to provide data with an accuracy of $\leq 0.1\%$ cannot be fulfilled in the presence of ghosts. To assure the data quality, LSEs must be determined and corrections have to be applied to historical data at all TCCON sites in the next step,

which is scheduled for the end of 2013. This should improve the accuracy to the desired value of 0.1% and the inter station comparability of the TCCON.

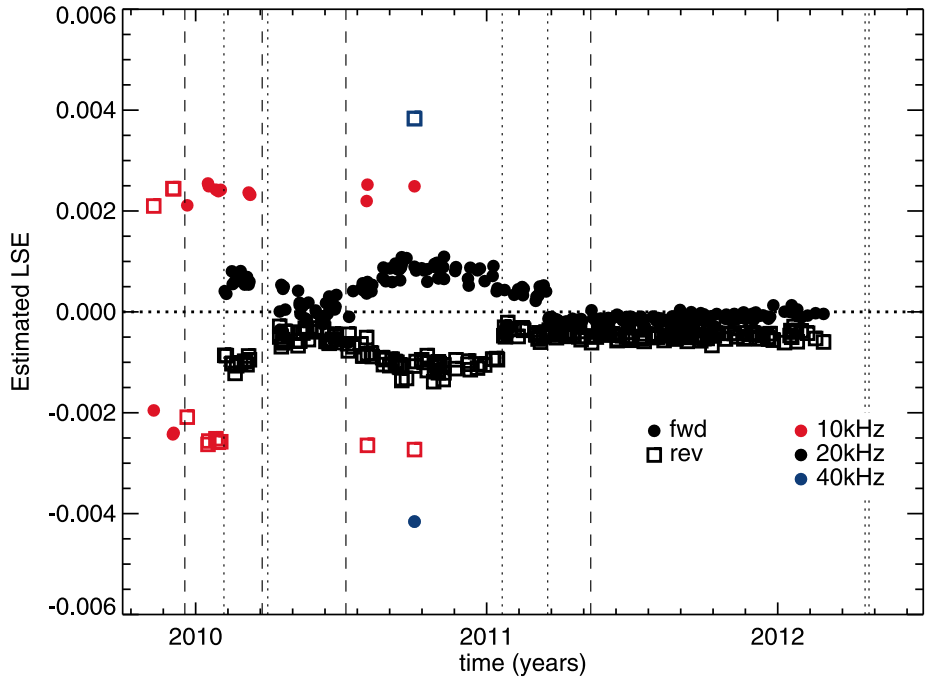

Figure 5.8: Lauder 125HR LSE time series determined from resampling analysis of solar interferograms using the 7290-7360 cm^{-1} interval. Instrument changes relevant to the LSE and/or its determination are shown with dashed lines: change from 10 to 20 kHz sample rate for routine acquisition (February 2010), increased phase resolution (April 2010), laser board and diodes exchange (January 2011) and reminimization of laser sampling error at 20 kHz after beam splitter exchange (March 2011). Instrument realignments are shown with dotted lines. (Taken from Dohe et al. [2013])

Chapter 6

TCCON X_{CO_2} data

In order to represent a high quality dataset for the validation of satellites and the investigation of the carbon cycle, TCCON data have to be calibrated onto the in situ network scale of the WMO. By use of vertical aircraft profiles above TCCON sites, the true total column of each gas can be determined and compared with the corresponding TCCON total column result. This kind of calibration has already been done by several calibration campaigns described in Washenfelder et al. [2006], Deutscher et al. [2010], Wunch et al. [2010] and Messerschmidt et al. [2011]. Compared to in situ measurements, FTIR X_{CO_2} results are biased by about 1%, which is mainly due to uncertainties in spectroscopic line data [Wunch et al., 2010]. Within the TCCON, this bias is corrected by applying a gas specific calibration factor of 0.989 for X_{CO_2}.
In this chapter, X_{CO_2} time series of the IMK-related TCCON sites Karlsruhe and Izaña will be presented and compared with nearby in situ measurements (Section 6.1). In addition, an intercomparison between TCCON data of four European sites, which are Karlsruhe (Germany), Bremen (Germany), Garmisch (Germany) and Orleans (France), will be presented in Section 6.2.

6.1 Comparison with in situ data

Concerning the IMK-related TCCON sites, Karlsruhe took part in the European IMECC (Infrastructure for Measurement of the European Carbon Cycle) campaign, where in total 5 TCCON sites participated and aircraft profiles have been recorded and compared to FTIR data [Messerschmidt et al., 2011]. Due to the absence of regular vertical CO_2 aircraft measurements at Izaña and Karlsruhe, the retrieved X_{CO_2} of these sites will be compared to ground-based nearby in situ measurements in this section.

6.1.1 Izaña

As already described in Section 3.4, an advantage of the Izaña site is the availability of co-located CO_2 in situ measurements, which are part of the WMO network GAW [Gomez-Pelaez et al.]. Most of the time, the station is located above a temperature inversion layer, acting as a natural barrier for local pollution. Air from below the inversion layer rises only during daytime, whereas night measurements are representative for the free troposphere. For comparison, mean day-night in situ values are used.

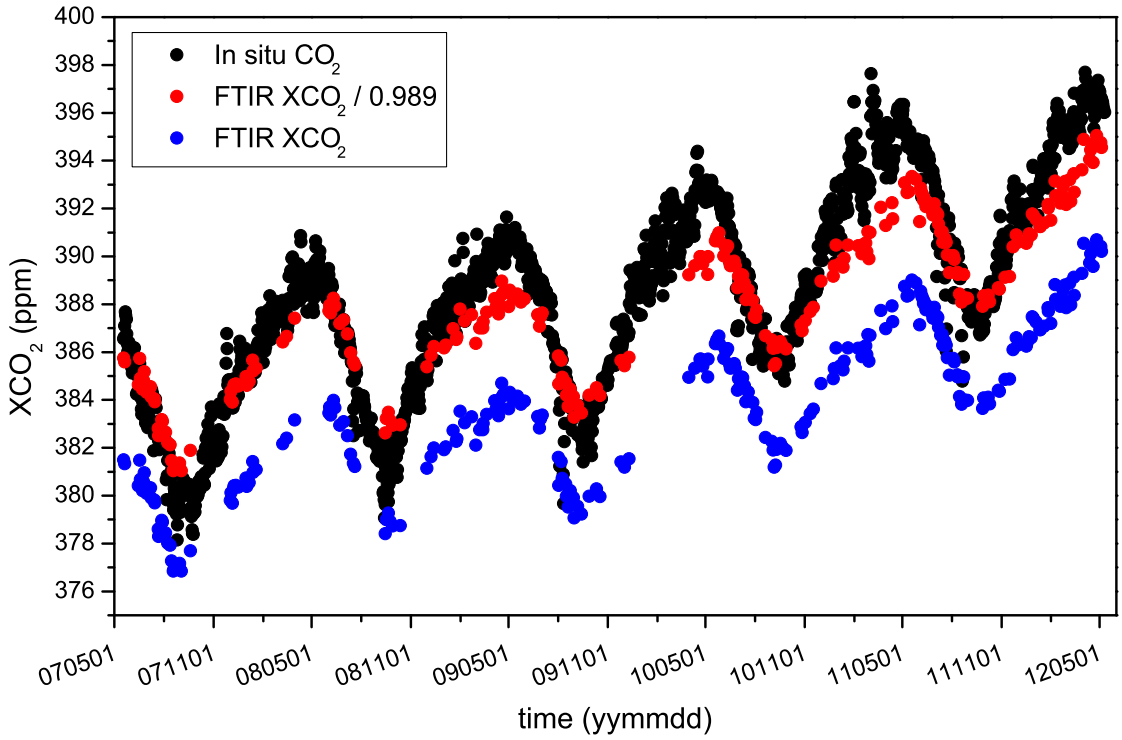

Figure 6.1: Izaña daily mean FTIR X_{CO_2} data (uncorrected: blue, corrected: red) and co-located in situ CO_2 measurements (black) from May 2007 to May 2012.

Figure 6.1 shows the daily mean FTIR X_{CO_2} data (blue and red) and co-located in situ CO_2 measurements (black) from May 2007 to May 2012. FTIR X_{CO_2} data were retrieved with the common TCCON recipe [Wunch et al., 2011], where results without applying the calibration factor of 0.989 are shown in blue, while the corrected results are shown in red. In all time series the annual cycle of CO_2 is clearly visible with increasing CO_2 concentrations over the years. However, there is a bias between the uncorrected FTIR retrieval results and in situ measurements, due to uncertainties in spectroscopic data as already described above. The corresponding correlation plot

is illustrated in Figure 6.2, where R=0.97 indicates a good agreement between the FTIR and the in situ time series. The slope of the regression line (line through origin) represents the bias between FTIR and in situ results. The bias of 1.3% resulting from a slope of 0.987 is in excellent agreement with the bias of 1% and the corresponding calibration factor of 0.989 which was detected within aircraft campaigns.

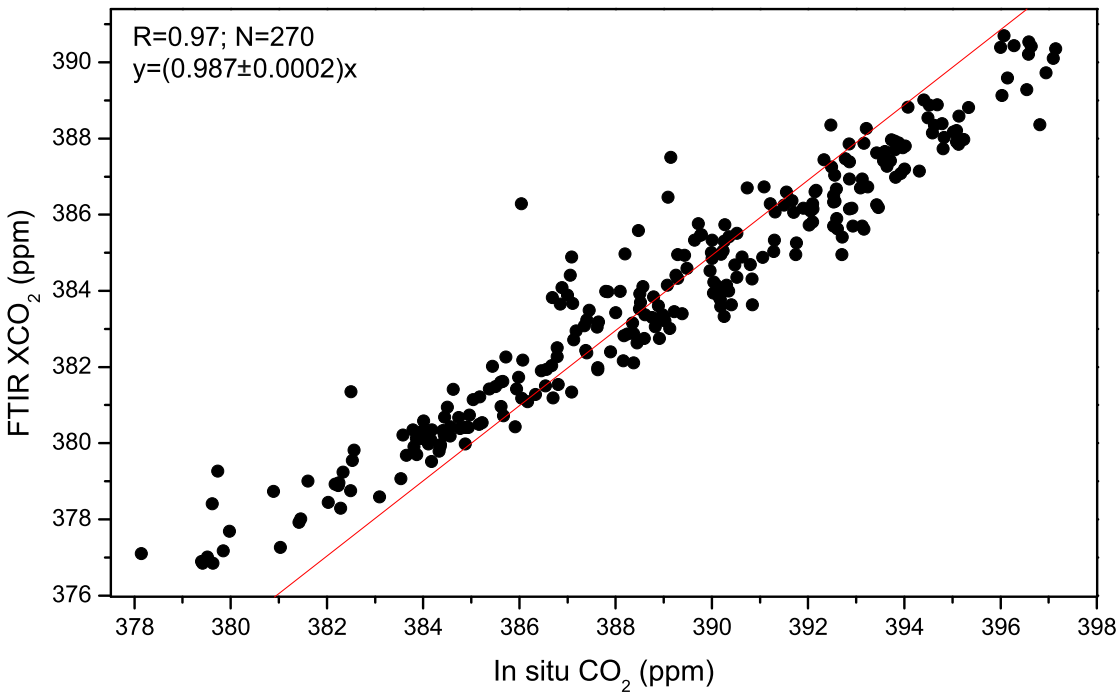

Figure 6.2: Correlation plot between daily mean FTIR X_{CO_2} data (uncorrected) and co-located in situ CO_2 measurements at Izaña, where the slope of the regression line represents the bias between FTIR and in situ results.

In addition to the discussed bias, another discrepancy between FTIR and in situ time series can be detected as well (Figure 6.1). For a better comparability, the detrended time series of in situ values (black) and FTIR measurements (red) are additionally shown in Figure 6.3. While the phases of the annual cycles are similar, the amplitude of the FTIR time series is only about 60% of the amplitude determined from in situ data. The reason is that variations in total column amounts are smaller both on seasonal and diurnal timescales, and are only indirectly affected by local fluxes, compared to variations of surface in situ values, which are strongly affected by local effects. Following Keppel-Aleks et al. [2011] variations in X_{CO_2} can be related to north-south gradients and the continental scale flux, whereas variations in surface in situ CO_2 values are more due to local fluxes.

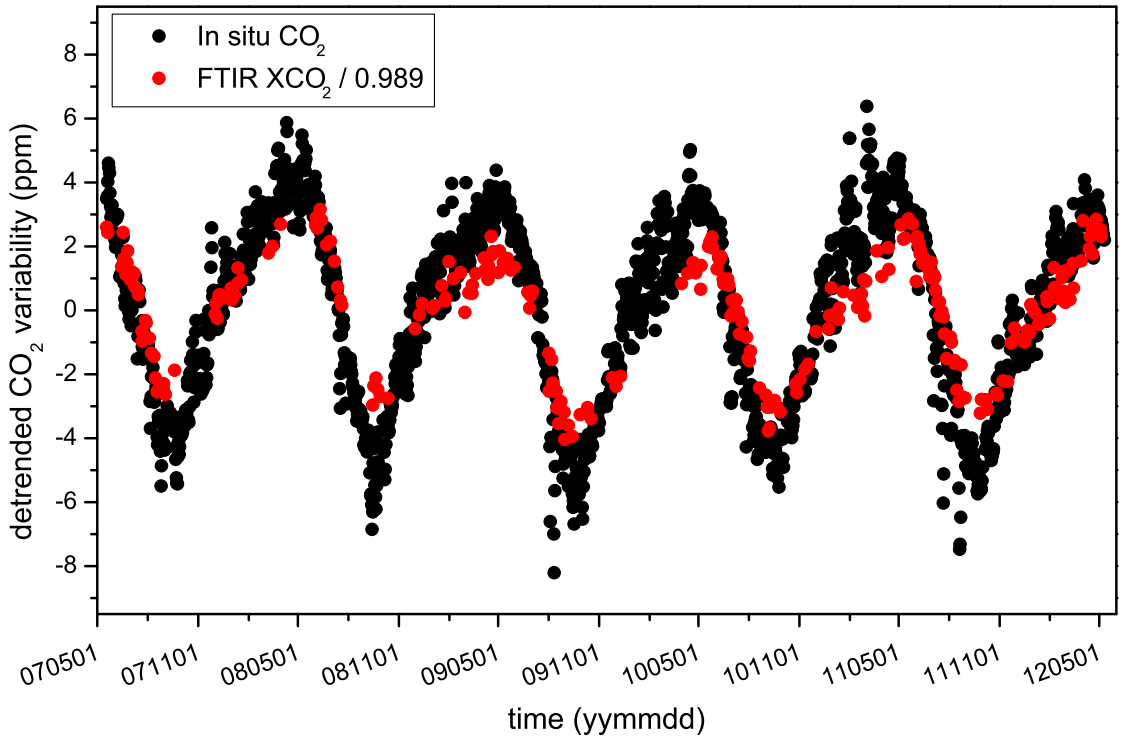

Figure 6.3: Detrended time series of daily mean FTIR X_{CO_2} data (red) and co-located in situ CO_2 measurements (black) for Izaña from May 2007 to May 2012.

6.1.2 Karlsruhe

Due to the absence of co-located in situ measurements at Karlsruhe, FTIR X_{CO_2} data are compared with in situ measurements of the GAW station Schauinsland[8]. The site is located in 140 km linear distance from KIT Campus North, nearby Freiburg in the Black Forest at an altitude of 1284 m. During nighttime measurements are representative for the free troposphere, while during daytime especially in summer, the station is located inside the boundary layer.

Figure 6.4 shows daily mean FTIR X_{CO_2} concentrations at Karlsruhe (blue and red) and nearby in situ CO_2 measurements (black) at Schauinsland from April 2010 to August 2012. Black rings represent in situ CO_2 measurements with coincident large CO concentrations, originating from incomplete combustion within the boundary layer. Like for Izaña, Karlsruhe X_{CO_2} data were analyzed using the standard TCCON recipe. The annual cycle of CO_2 can be seen in all time series, where the bias between uncorrected FTIR data (blue) and in situ measurements (black) is distinctive and reduced by applying the WMO calibration factor of 0.989 (red time series). The in situ CO_2 time

[8]Luftmessnetz des Umweltbundesamtes, Messstation Schauinsland

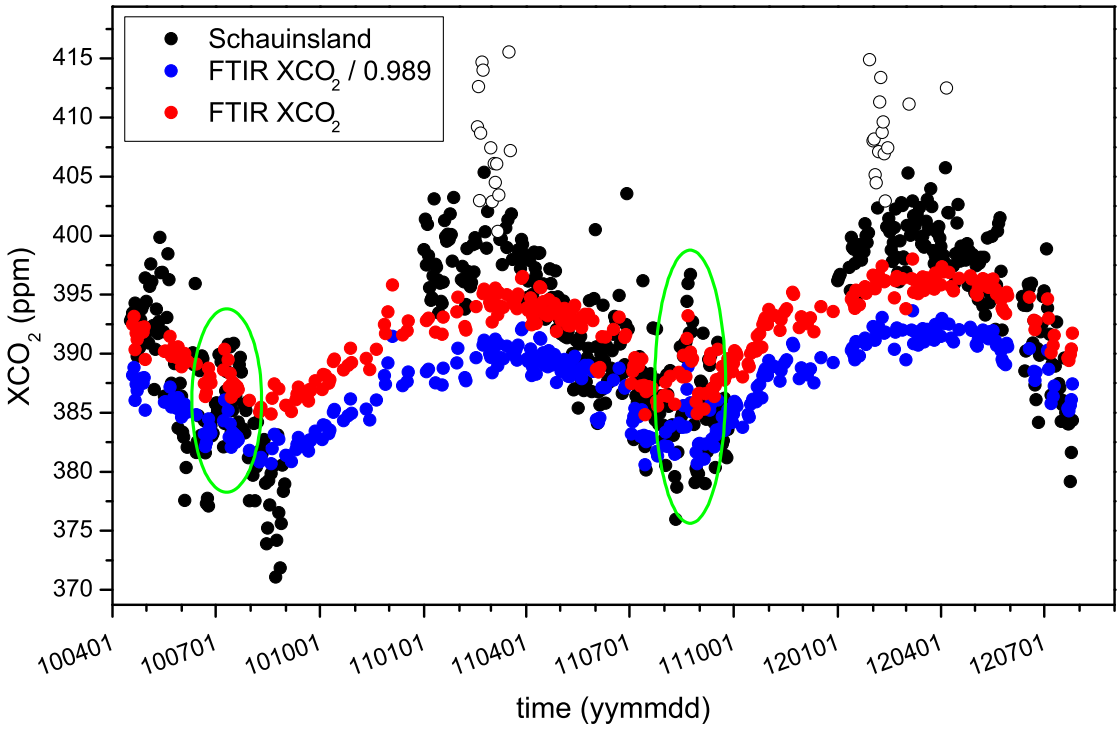

Figure 6.4: Karlsruhe daily mean FTIR X_{CO_2} data (uncorrected: blue, corrected: red) and simultaneous Schauinsland in situ CO_2 measurements (black) from April 2010 to August 2012. Black rings show CO_2 measurements with coincident large CO concentrations. Common events with unusually large CO_2 amounts are marked green.

series shows a larger scatter compared to FTIR total column results and also to Izaña in situ measurements (Figure 6.4), due to the station's location inside the boundary layer (during daytime). By neglecting measurements with simultaneously large CO values, the scatter is strongly reduced. The influence on in situ measurements by local sources and sinks is also reflected in the magnitude of the annual cycle's amplitude. For FTIR data the amplitude is only 40% of the one determined from in situ values. In addition, common events with unusually large CO_2 concentrations can be detected (marked green), which have to be investigated further.

A correlation plot between uncorrected FTIR data and in situ measurements is shown in Figure 6.5. The stability index of R=0.84 indicates a good correlation, but a weaker one compared to Izaña results (see above). Neglecting measurements with coincident large CO values (black rings), the scatter for high CO_2 values is reduced. With 0.989 (bias between FTIR and in situ of 1%), the value for the regression line's slope is in exact agreement with aircraft campaign results and the WMO calibration factor.

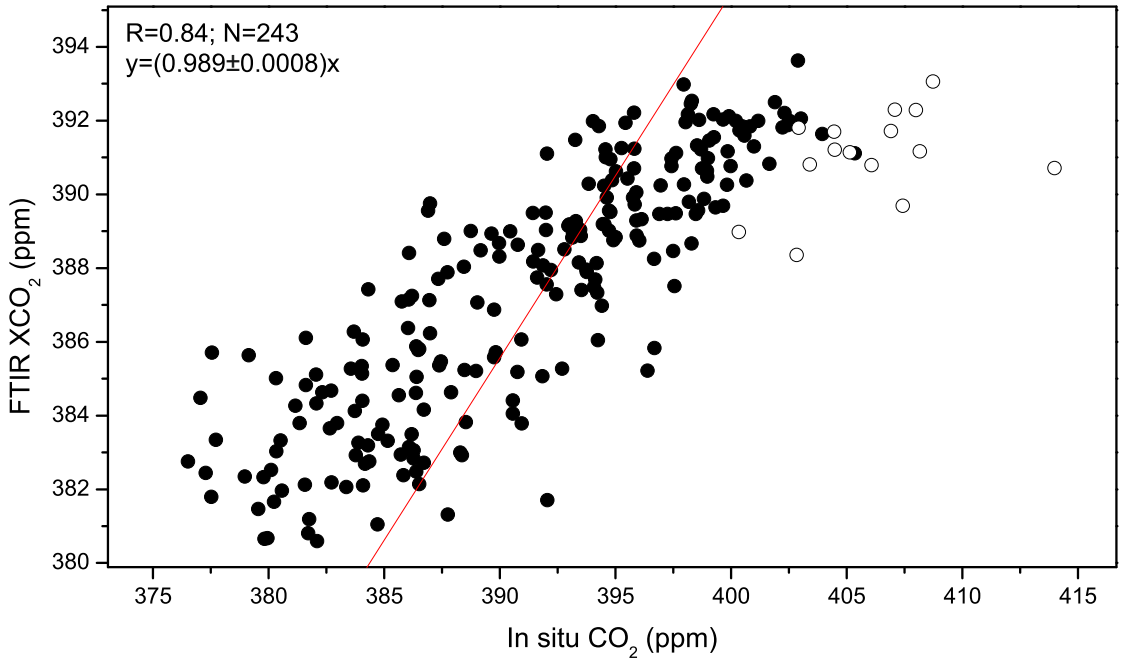

Figure 6.5: Correlation plot between Karlsruhe daily mean FTIR X_{CO_2} data and simultaneous Schauinsland in situ CO_2 measurements, where the slope of the regression line represents the bias between FTIR and in situ results. Black rings represent CO_2 measurements with simultaneously large CO concentrations.

6.2 Intercomparison between nearby TCCON sites

A map of worldwide TCCON sites has already been shown in Figure 3.4, where the large quantity of TCCON sites in middle Europe is obvious. Karlsruhe is one of these sites and X_{CO_2} data can therefore be compared to data from the nearby TCCON stations Bremen (Germany, Messerschmidt et al. [2011]), Garmisch (Germany, IMK-IFU) and Orleans (France, Messerschmidt et al. [2011]). Distances between the considered sites and Karlsruhe vary from 260 km (Karlsruhe–Garmisch) to 500 km (Karlsruhe–Orleans), where the distance between Karlsruhe and Bremen is about 440 km. The time series of daily mean X_{CO_2} (analyzed by means of the common TCCON recipe) for the four different TCCON sites from April 2010 to August 2012 is shown in Figure 6.6.

The annual cycle looks very similar for the different sites. However, the Garmisch time series (black) shows about 2–3 ppm smaller X_{CO_2} values during winter than the annual cycles for Karlsruhe (red) and Bremen (blue). Orleans (dark cyan) is hard to evaluate due to several gaps in the time series. The disagreement could be attributed to the differences in altitude of more than 600 m between the Garmisch station and the

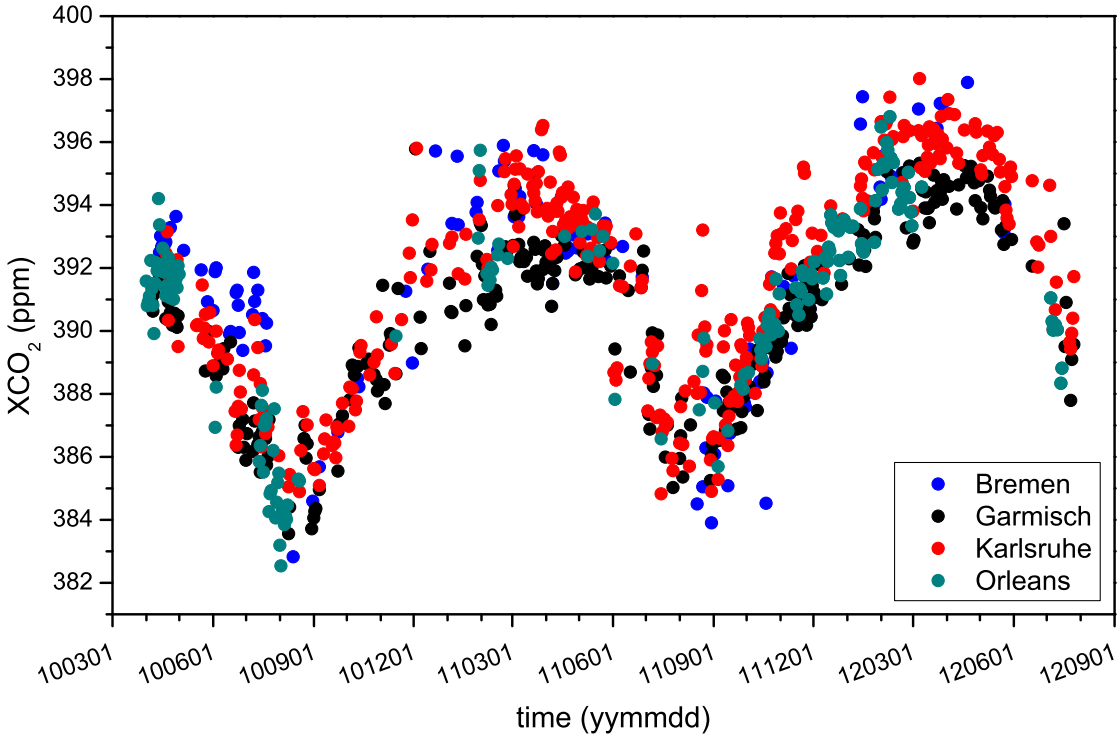

Figure 6.6: Daily mean FTIR X_{CO_2} data of four European TCCON sites: Bremen (blue), Garmisch (black), Karlsruhe (red) and Orleans (dark cyan) from April 2010 to August 2012 .

other three sites. Due to seasonal changes of the boundary layer's height (minimum in winter), the effect of photosynthesis and respiration is less pronounced for Garmisch in winter time, resulting in smaller X_{CO_2} values.
In addition, periods with unusually large X_{CO_2} values can be detected for each site. These events are assumed to be real and have to be investigated further by analyzing the respective air masses.

6.3 Conclusions

Ground-based FTIR retrieval results have to be calibrated onto the WMO in situ network's scale in order to represent a high quality dataset for satellite validation and investigating the carbon cycle. This can be realized by comparison with vertical aircraft profiles above the TCCON stations, which was already done at several TCCON sites leading to the TCCON calibration factor of 0.989 for X_{CO_2}.
Due to the lack of regular aircraft measurements of vertical CO_2 distributions at the IMK-related sites Izaña and Karlsruhe, these data were compared to nearby ground-

based in situ measurements within this chapter. In the case of Izaña, where the station is located above a temperature inversion layer most of the time, a calibration factor of 0.987 was determined, which is in good agreement with results of the mentioned aircraft campaigns. Compared to FTIR measurements, the large amplitude of the in situ data's annual cycle was attributed to the higher affection of in situ measurements by local effects.

The comparison between Karlsruhe FTIR total column results and in situ data of the Schauinsland station with a distance of about 140 km also indicated a good correlation, where the determined calibration factor of 0.989 exactly matches the factor used within TCCON. The large scatter and amplitude of in situ values are due to the location inside the boundary layer leading to an affection by local sources and sinks, which is reduced by neglecting CO_2 with coincident large CO concentrations. In addition, common events with unusually large CO_2 concentrations were determined and need to be investigated further by use of backward trajectories, in order to determine the sources.

In the last part of this chapter, the comparison between X_{CO_2} retrieval results of the European TCCON sites Karlsruhe, Bremen, Garmisch and Orleans was described, where the amplitude of the annual cycle for Garmisch is about 2–2.5 ppm smaller than for the other sites, due to the differences in altitude of more than 600 m. Furthermore, periods with unusually large amounts of X_{CO_2} were detected for each site. These events have to be investigated by analyzing the corresponding air masses.

Chapter 7

Optimization of the PROFFIT retrieval setup

High-resolution ground-based FTIR spectra in the NIR region have been recorded at the IMK-related sites Karlsruhe and Izaña since 2010 and 2007, respectively. In order to provide data with excellent quality (e.g. within the TCCON), measurements have to be analyzed accurately. In the context of this Ph.D. thesis, the analysis of CO_2 from NIR measurements was undertaken with the use of the PROFFIT software. First the analysis procedure for CO_2 was created and in the course of this work optimized step-by-step (e.g. by implementation of new features like line mixing or modifying the spectroscopic line lists), with the objective to minimize the residuals between measurement and fit, leading to an improved data accuracy.
For public distribution within the TCCON, only data analyzed with the GFIT software are accepted. Therefore all measurements for Karlsruhe and Izaña are processed with GFIT as well, and compared to PROFFIT retrieval results. By means of this comparison the impact of several error sources within the radiative transfer and the retrieval setup on resulting total column amounts can be determined. The findings of this cross-validation could provide an indication of present errors in the operational code GFIT, which have to be minimized to improve the total column accuracy and ensure the high quality of the data.
In this chapter the analysis of X_{CO_2} from ground-based NIR measurements and the stepwise optimization of the PROFFIT analysis procedure is presented. In addition, the retrieved PROFFIT results are cross-validated with GFIT total column amounts. Due to the absence of laser sampling errors and other disturbing effects, the Karlsruhe dataset is considered within this chapter.

7.1 Air-broadening width

As already mentioned in Section 2.2, pressure broadening has to be taken into account to describe the spectral line shape. The higher the density of molecules, the larger is the probability of collisions between them. Therefore, pressure broadening is more important for lower atmospheric levels.
The PROFFIT analysis of spectra is based on the HITRAN 2008 database [Rothman et al., 2009], where the air-broadening width (in $cm^{-1}atm^{-1}$) is documented for each line. If this parameter is erroneous, uncertainties in the retrievals occur, leading to solar zenith angle dependencies of the retrieved gas concentrations due to the more pronounced effect for larger air masses.

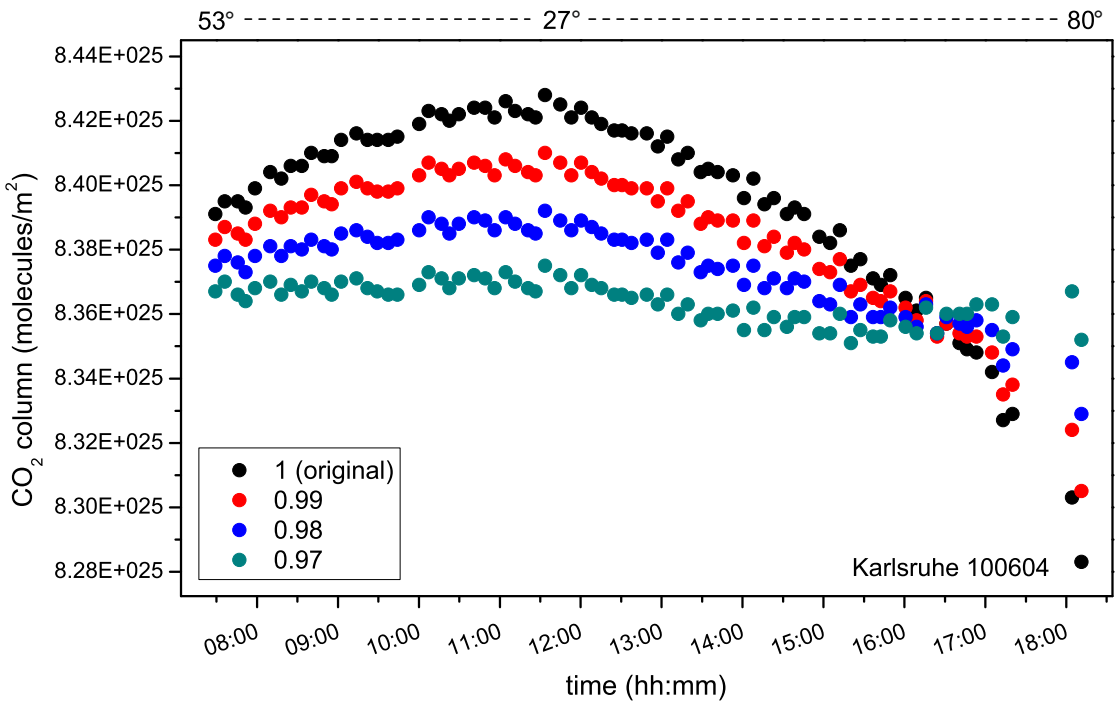

Figure 7.1: CO_2 total column results for June 4th, 2010 at the Karlsruhe site (7:30 AM to 6:00 PM, SZAs between 27° (noon) and 80°). Original results are illustrated with black dots, whereas results for different applied air-broadening correction factors are shown in different colors. Results determined with the recommended correction factor of 0.97 are illustrated in dark cyan.

The CO_2 column over the course of June 4th, 2010 from 7:30 AM to 6:00 PM at Karlsruhe is shown in Figure 7.1, where SZAs are in the range of 27° (noon) to 80°. The black dots represent the retrieved results using line data with original air-broadening widths. CO_2 column amounts indicate a distinctive air mass dependency, distorting

the true values. In order to correct this effect, air-broadening widths are modified by applying a correction factor to air-broadening parameters of all lines. After that, the data is reprocessed and the course of CO_2 concentrations during a day can be compared for different applied factors, which are illustrated in different colors in Figure 7.1. Based on the original results (black), the air mass dependence is already reduced by using a corrections factor of 0.99 (red). Up to the factor of 0.97 (dark cyan), air mass effects are nearly negligible, whereas an appliance of correction factors smaller than 0.97 leads to opposite air mass dependences.
Concerning the results of this study, a factor of 0.97 has to be used to eliminate air mass dependent effects. To verify this factor, a similar study has to be undertaken for a different day and at a different site. Hence, measurements at Izaña are used for this investigation.

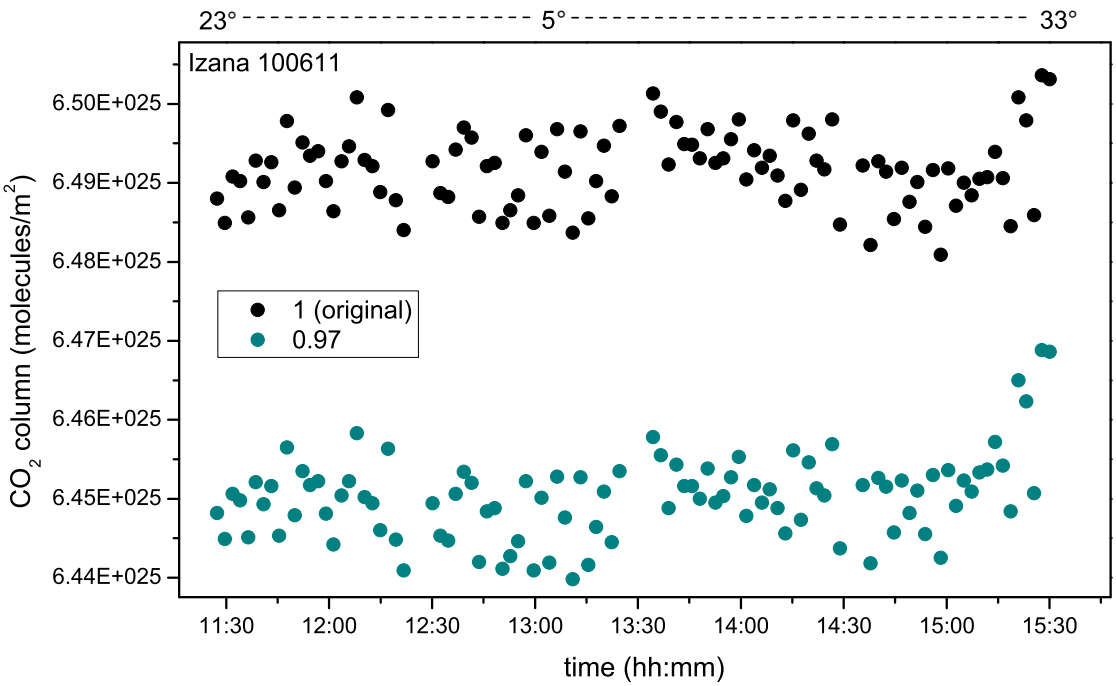

Figure 7.2: CO_2 total column results for June 11th, 2011 at the Izaña site (11:30 AM to 3:30 PM, SZAs between 5° (noon) and 33°). Original results are illustrated with black dots, whereas results determined with the applied air-broadening correction factor of 0.97 are shown in dark cyan.

The CO_2 column over the course of June 11th, 2011 from 11:30 AM to 3:30 PM (SZAs between 5° (noon) and 33°) at Izaña is shown in Figure 7.2, where results using the original air-broadening widths are illustrated in black, whereas the results including

the applied correction factor of 0.97 are shown in dark cyan. Due to the site's high altitude, air mass dependent effects are already small with the use of original parameters (black). Using the correction factor of 0.97 (dark cyan), these effects are eliminated. An additional effect using corrected air-broadening widths is the reduction of CO_2 column amounts of 0.6% at both sites.

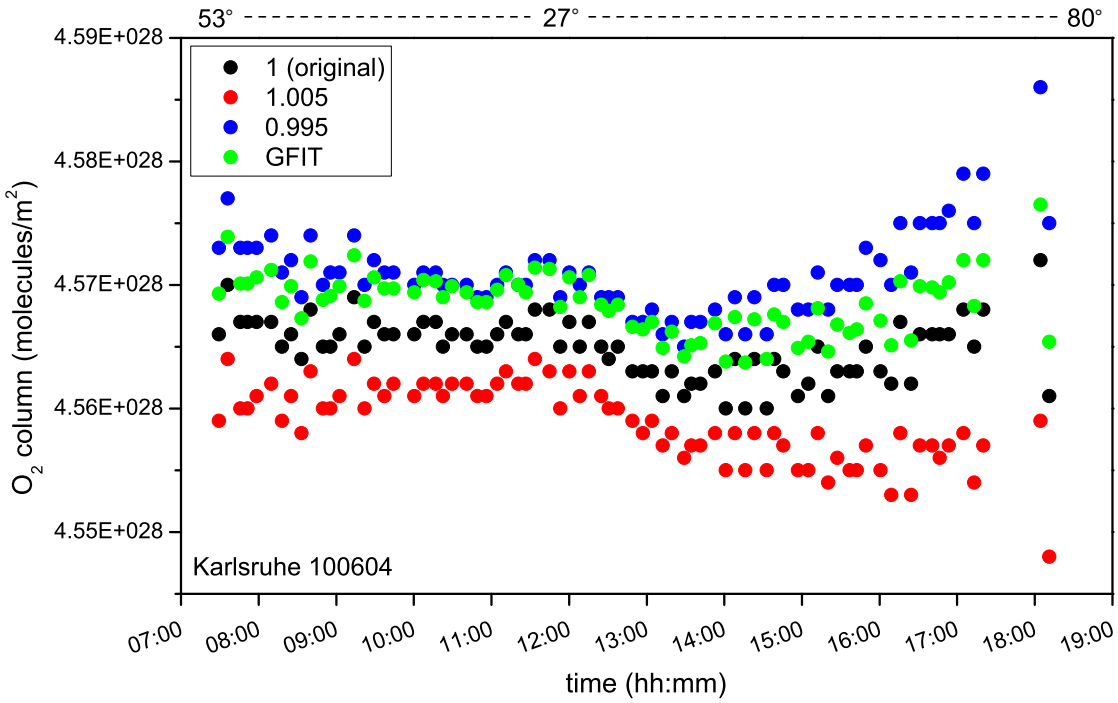

Figure 7.3: O_2 total column results for June 4th, 2010 at the Karlsruhe site (7:30 AM to 6:00 PM, SZAs between 27° (noon) and 80°). Original results are illustrated with black dots, whereas results determined with the different applied air-broadening correction factors 1.005 and 0.995 are shown in red and blue. Green dots represent results retrieved with the use of the original GFIT O_2 line list.

Due to the use of X_{CO_2} within the TCCON, O_2 retrieval results have to be tested as well, which is illustrated in Figure 7.3 for Karlsruhe (June 4th, 2010) and in Figure 7.4 for Izaña (June 11th, 2011). In contrast to CO_2, O_2 total column results using the original air-broadening widths (black) indicate a realistic behavior during the course of the day at both sites. Implementation of air-broadening correction factors (1.005 and 0.995) lead to a worsening of the results (red and blue). In addition, O_2 total column results retrieved after implementation of the original GFIT O_2 line list (see Section 7.8) are shown in green, where a bias of about 0.08% compared to the results retrieved with the use of the original PROFFIT line list (black) can be detected. For the GFIT

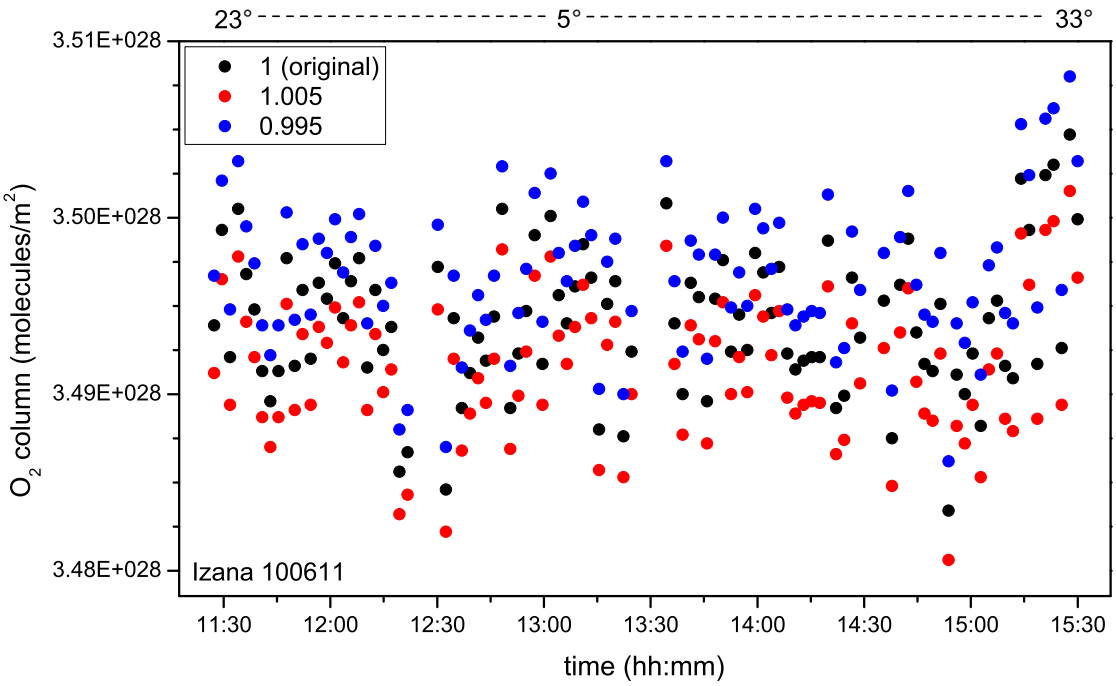

Figure 7.4: O_2 total column results for June 11th, 2011 at the Izaña site (11:30 AM to 3:30 PM, SZAs between 5° (noon) and 33°). Original results are illustrated with black dots, whereas results determined with the different applied air-broadening correction factors 1.005 and 0.995 are shown in red and blue.

line list, air mass dependent effects are negligible as well. Henceforward, the confirmed CO_2 air-broadening correction factor of 0.97 is used for common X_{CO_2} retrievals with PROFFIT in order to achieve accurate retrieval results, whereas O_2 line data remain unchanged.

7.2 Implementation of line mixing

Concerning high-resolution ground-based FTIR measurements, errors in spectral line shapes have a large impact on resulting total gas columns. Therefore effects like line mixing should not be neglected within the analysis of NIR spectra.

Line mixing happens if due to a molecular collision a population transfer between rotational-vibrational states takes place, leading to a modified intensity of the considered band. The amount of LM correlates with pressure, since the pressure is proportional to the density of molecules.

Neglecting this effect causes significant errors in absorption coefficients, leading to systematic effects in fit residuals and air mass dependent CO_2 concentrations [Hartmann

et al., 2009]. To avoid that, LM was implemented for CO_2 as a new feature within the PROFFIT analysis in the course of this work. The line mixing parameter $Y(T)$ as well as the temperature dependency was calculated based on the LM code by Tran and Hartmann [Hartmann et al., 2009]. In front of each line participating in LM an additional line was implemented in the HITRAN line list, and labeled with the species code 997. This line contains all necessary information to determine $Y(T)$ for the following line.

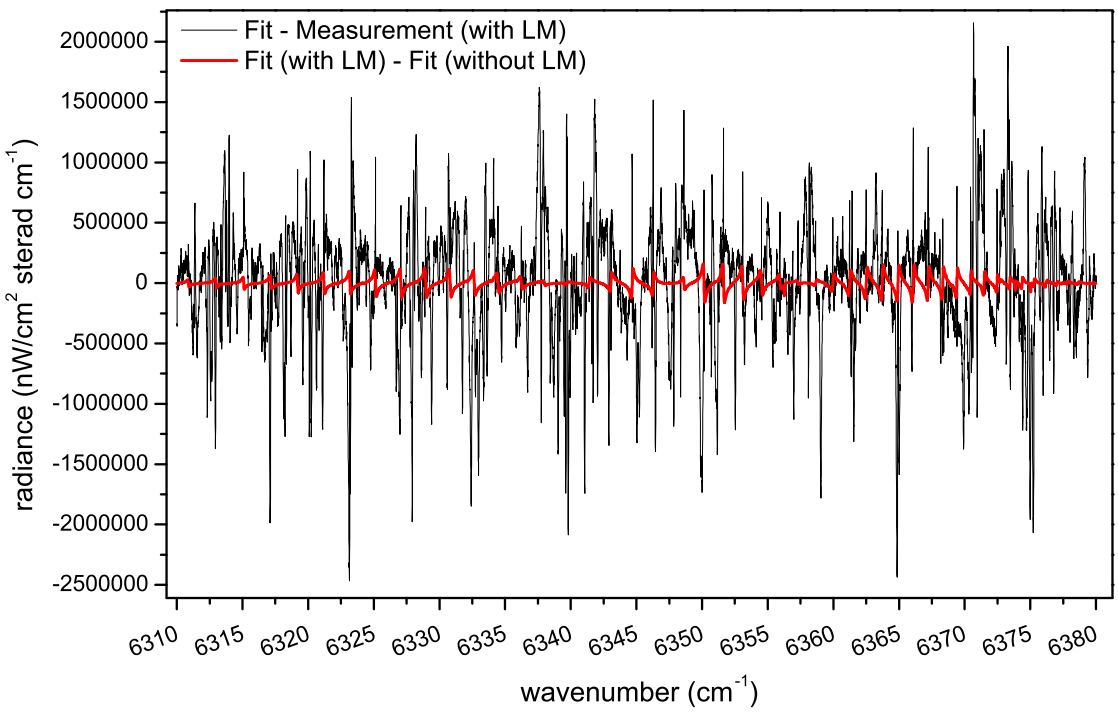

Figure 7.5: Residuals between fit and measurement for the 6310–6380 cm^{-1} microwindow after implementation of line mixing are shown in black for a measurement at Karlsruhe. The red curve represents the difference between fit with LM and fit without LM.

In Figure 7.5 the residuals between fit and measurement for the 6310–6380 cm^{-1} microwindow after implementation of line mixing are shown for a measurement at Karlsruhe. In addition, the discrepancy between the fit with LM and the fit without LM is illustrated in red, indicating the necessity of the LM implementation due to detectable systematic effects. The impact of improved residuals due to the implementation of LM on total column CO_2 amounts is shown in Figure 7.6 for June 4th, 2010 at Karlsruhe (7:30 AM–6:30 PM). Retrieval results without considering LM are illustrated as red rings, whereas black squares represent results of the setup where LM was implemented.

Due to only slight differences between the results with and without LM, the effect can be described as near negligible for the setup used. Concerning profile retrievals, which will be presented in Chapter 8, a non-negligible impact is expected.

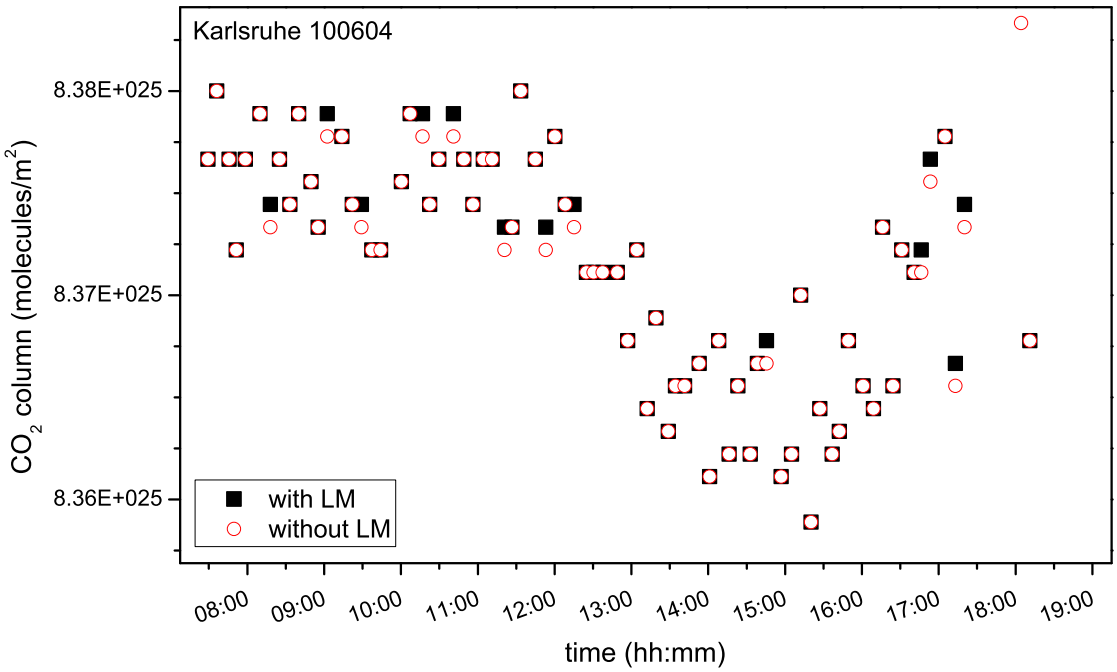

Figure 7.6: CO_2 total column amounts for June 4th, 2010 at Karlsruhe (7:30 AM–6:30 PM). Results where LM is neglected are shown as red rings, whereas black squares represent results with implemented LM.

7.3 Baseline fit and collision induced absorption

Due to the use of X_{CO_2} within TCCON, also total columns of O_2 have to be analyzed carefully, where especially collision induced absorption has to be considered. Concerning the common PROFFIT analysis, the collision induced spectral line shape is considered by applying an extended baseline fit, in contrast to the GFIT software, where a CIA model is used. In the course of this work, an O_2 CIA model was additionally included within PROFFIT, essentially following Chagas et al. [2002]. In this section, the new feature will be validated and compared to the previously used baseline fit. The O_2 microwindow (7765–8005 cm^{-1}) for a measurement at Karlsruhe is shown in Figure 7.7, where the measured spectrum is illustrated in black, the fitted spectrum in red and the residual between measurement and fit in blue. The measurement shown

in (a) was analyzed without the new CIA feature, simply using a 2 parameter baseline fit. It indicates huge differences between fit and measurement, reflected in a large residuum, due to the missing alignment of the CIA spectral shape. In contrast, plot (b) shows the same measurement, but analyzed using the CIA model in addition to the 2 parameter baseline fit. The CIA spectral shape is reproduced accurately, leading to small residuals between fit and measurement. Therefore the implementation of the CIA model was successful. Nevertheless a comparison between the use of the CIA feature and using an extended baseline fit needs to be performed in order to determine if the implementation of CIA leads to better results, as it is assumed by TCCON.
In Figure 7.8 spectral fits of the considered O_2 microwindow are shown again, where in (a) a 25 parameter baseline fit in addition to the CIA feature was applied, while in (b) only a 25 parameter baseline fit was implemented. Comparing the two Figures, residuals between fit and measurement of the two different setups appear identical. To investigate the necessity of using a CIA model in presence of an extended baseline fit, O_2 retrieval results from both setups have to be compared, which is done by considering time series of O_2 total column amounts from Karlsruhe and Izaña. The corresponding correlation plots are shown in Figure 7.9, where total columns of O_2 with implemented CIA are plotted against O_2 columns without CIA. Both setups ((a) Karlsruhe, (b) Izaña) contain a 25 parameter baseline fit.
With R=1 and the regression line's function of $y = x$, the results retrieved with both setups are identical for Izaña and for Karlsruhe as well. This leads to the conclusion that modeling the CIA feature is dispensable for TCCON retrievals if an extended baseline fit is used.

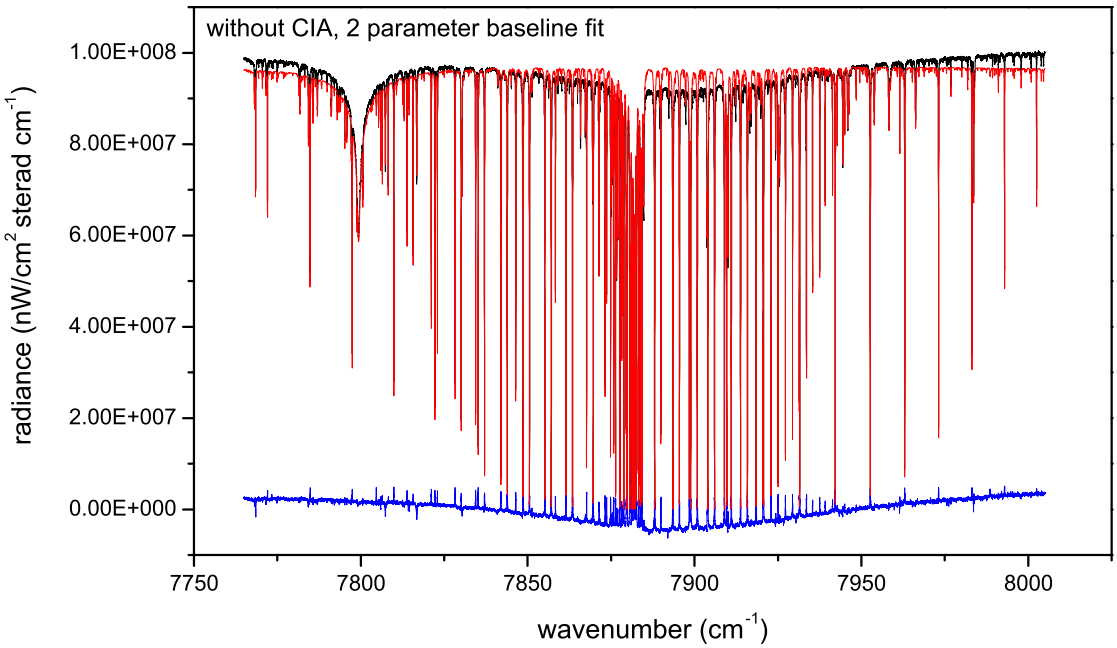

(a) Without CIA and with a 2 parameter baseline fit.

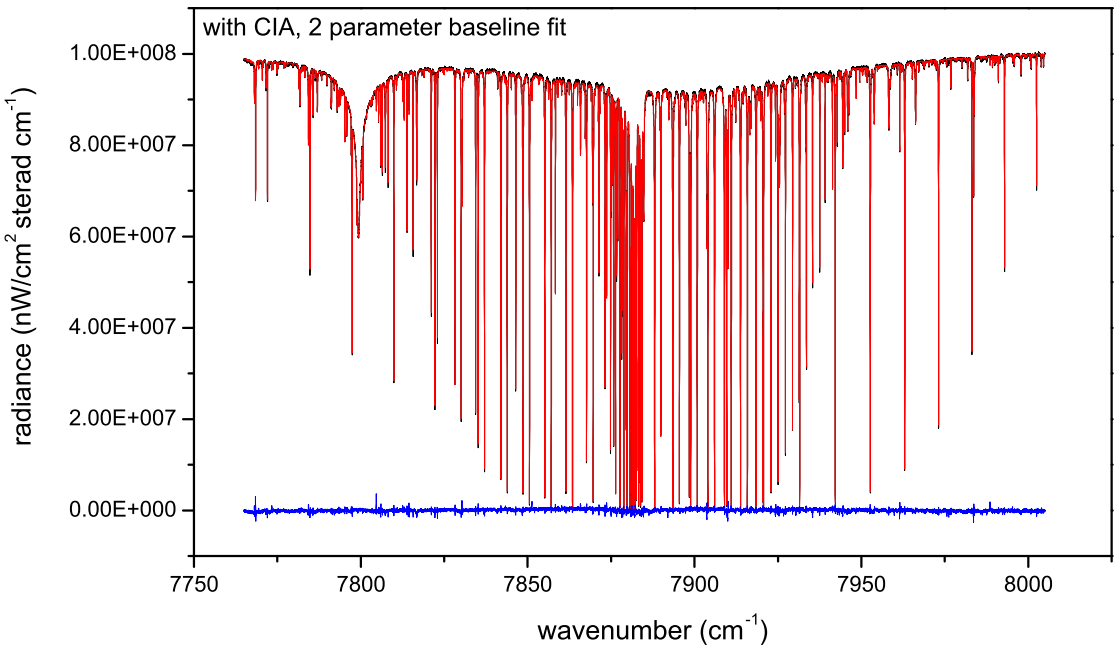

(b) With CIA and a 2 parameter baseline fit.

Figure 7.7: O_2 microwindow (7765–8005 cm^{-1}) analyzed with different setups for a measurement at Karlsruhe, where the measured spectrum is shown in black, the fitted spectrum in red and the residual in blue.

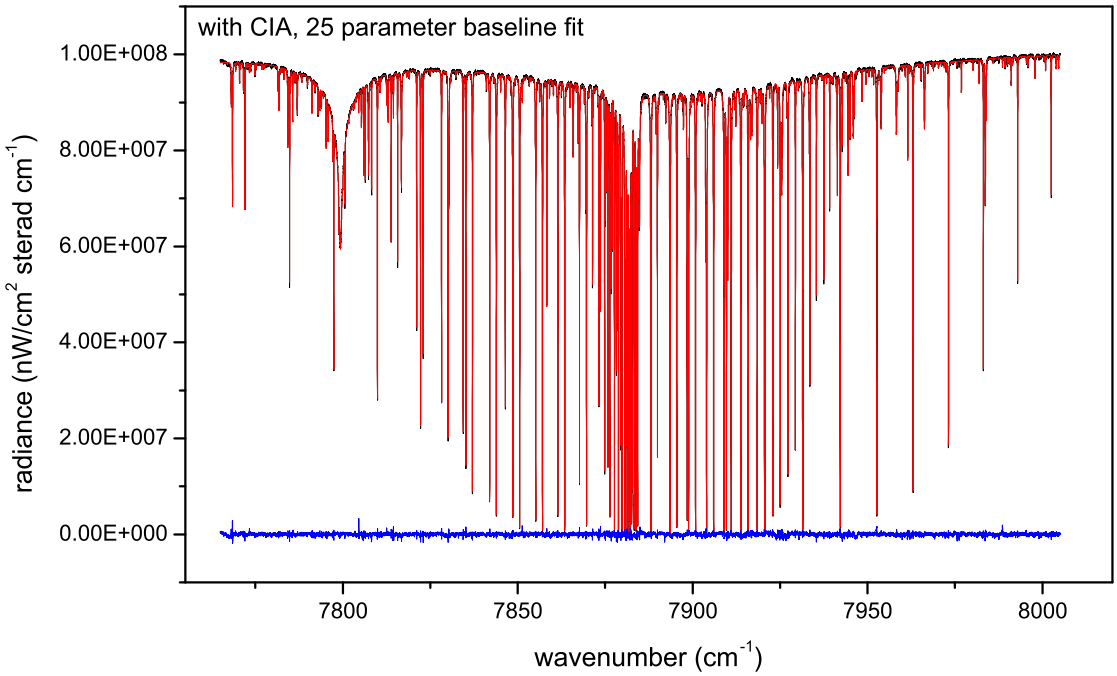

(a) With CIA and a 25 parameter baseline fit.

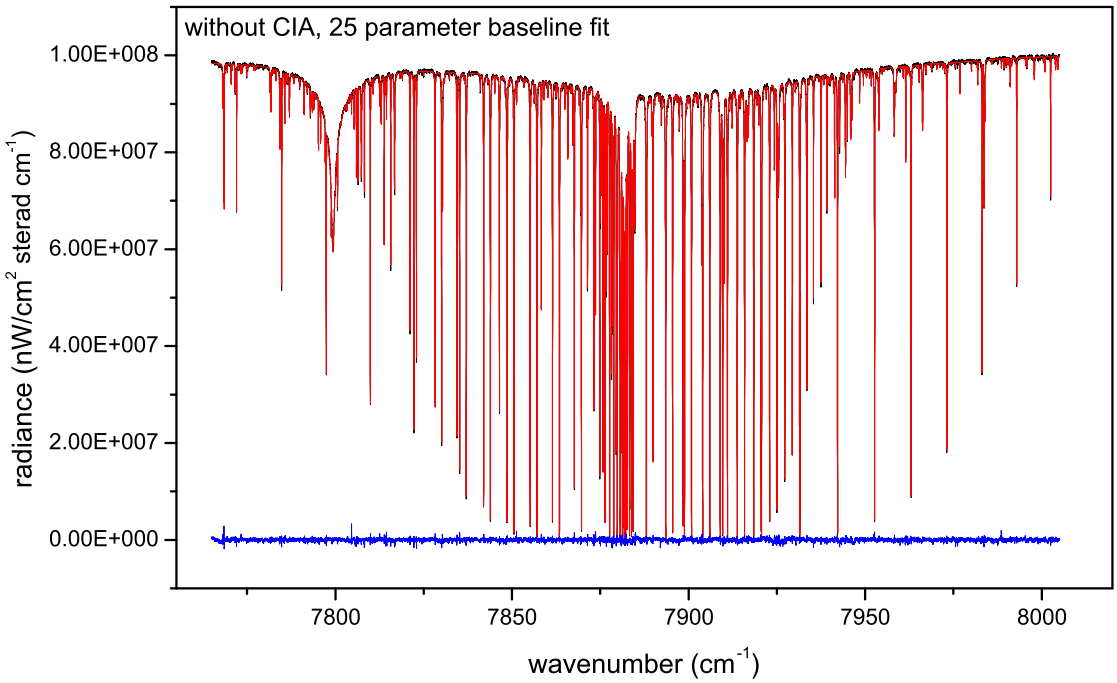

(b) Without CIA and with a 25 parameter baseline fit.

Figure 7.8: O_2 microwindow (7765–8005 cm^{-1}) analyzed with different setups for a measurement at Karlsruhe, where the measured spectrum is shown in black, the fitted spectrum in red and the residual in blue.

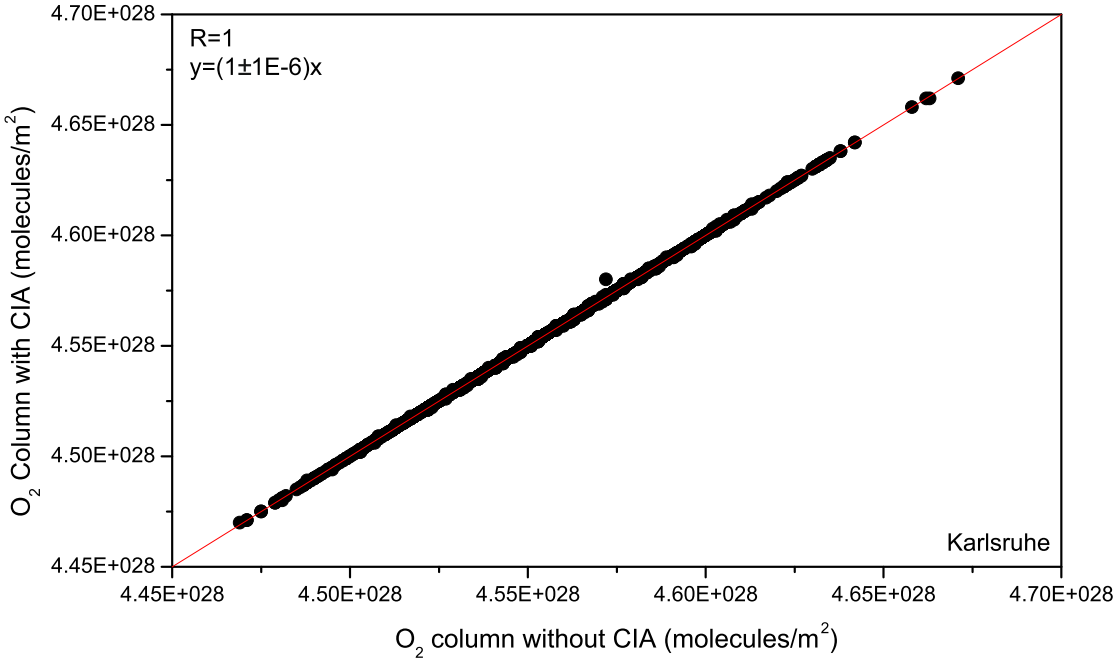

(a) Karlsruhe time series.

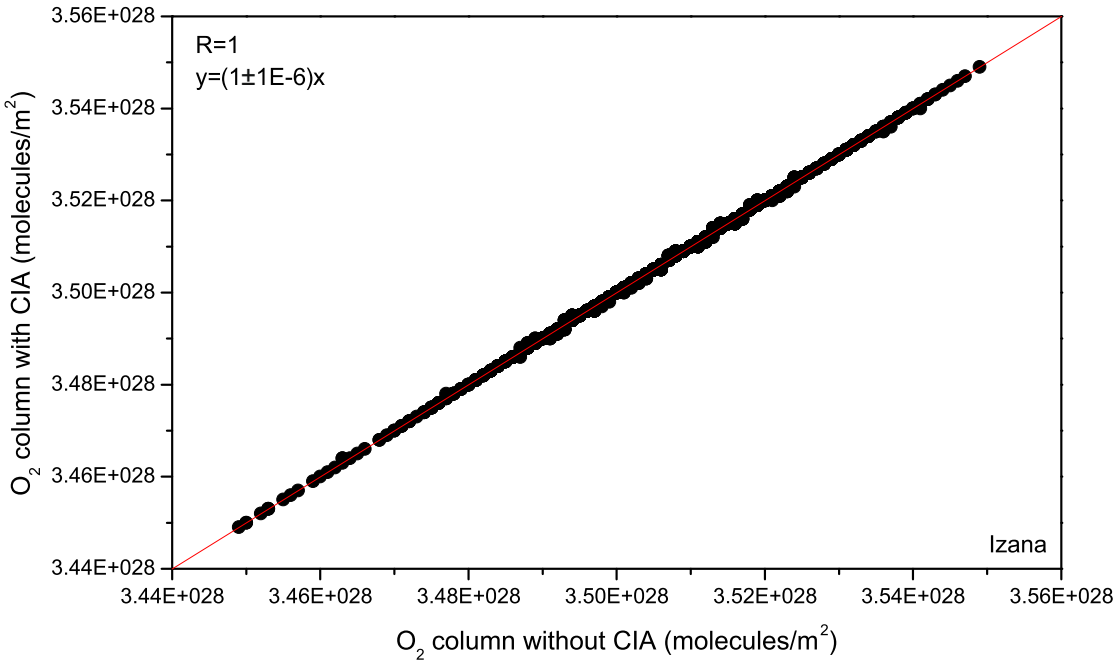

(b) Izaña time series.

Figure 7.9: Correlation plots between total columns of O_2 including the CIA feature and O_2 total columns without the implementation of CIA for Karlsruhe and Izaña.

7.4 Reparametrization of partition functions

The partition function $Q(T)$ specifies the total number of accessible quantum states at a certain temperature and is important for the calculation of line intensities from the Boltzmann distribution. Detailed information about the vibrational and rotational partition functions and the calculation of line intensities can be found in von Clarmann [2003].

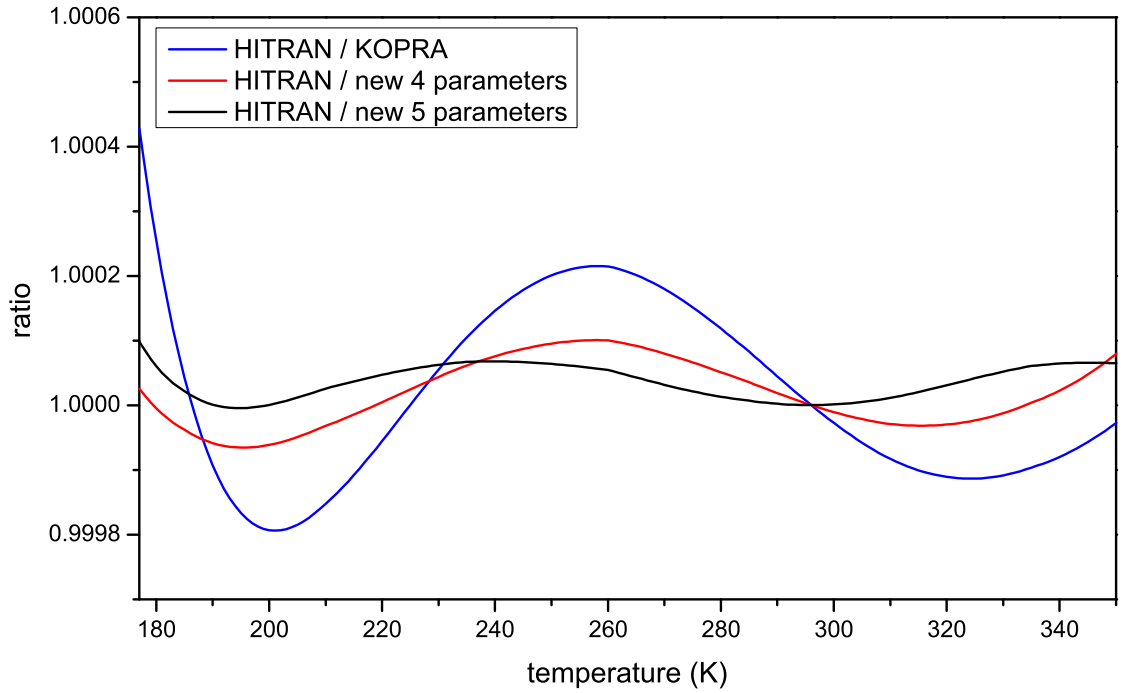

Figure 7.10: Ratio between $Q(T)$ from HITRAN and $Q(T)$ used by PROFFIT against the temperature. The comparison with KOPRA $Q(T)$ is shown in blue, with the more precise 4 parameters setup in red and with the 5 parameters setup in black.

In the analysis procedure, partition functions are implemented for each molecule (including different isotopes), where the way of implementation differs between PROFFIT and GFIT. Concerning the latter one, tabulated values of $Q(T)$ from the HITRAN database are used. In contrast, PROFFIT calculates $Q(T)$ for each molecule during the analysis by means of a parametrization from KOPRA (Karlsruhe Optimized and Precise Radiative transfer Algorithm), where 4 temperature and mass dependent parameters are used. In the course of this work, a more precise parametrization was implemented by adapting the PROFFIT partition functions to original HITRAN values. Therefore the ratio between $Q(T)$ from HITRAN and $Q(T)$ from PROFFIT

is considered, which is shown in Figure 7.10, where the ratio is plotted against the temperature in the range of 176 to 350 K. The relation between HITRAN data and KOPRA $Q(T)$ is shown in blue with a bias of up to 0.04%. The new, more precise parametrization of $Q(T)$ (4 parameters) is illustrated in red, where the deviation is reduced to 0.01%. In order to minimize this bias, the parametrization of $Q(T)$ was again improved by using a polynomial fit of fifth order. Corresponding results are shown as a black curve in Figure 7.10, indicating a reduction of the bias in the relevant range to 0.007%.

The effect of adapting PROFFIT $Q(T)$ values to HITRAN can be determined in X_{CO_2} as well, which is shown by means of the Karlsruhe time series of daily mean X_{CO_2} from April 2010 to March 2011 in Figure 7.11.

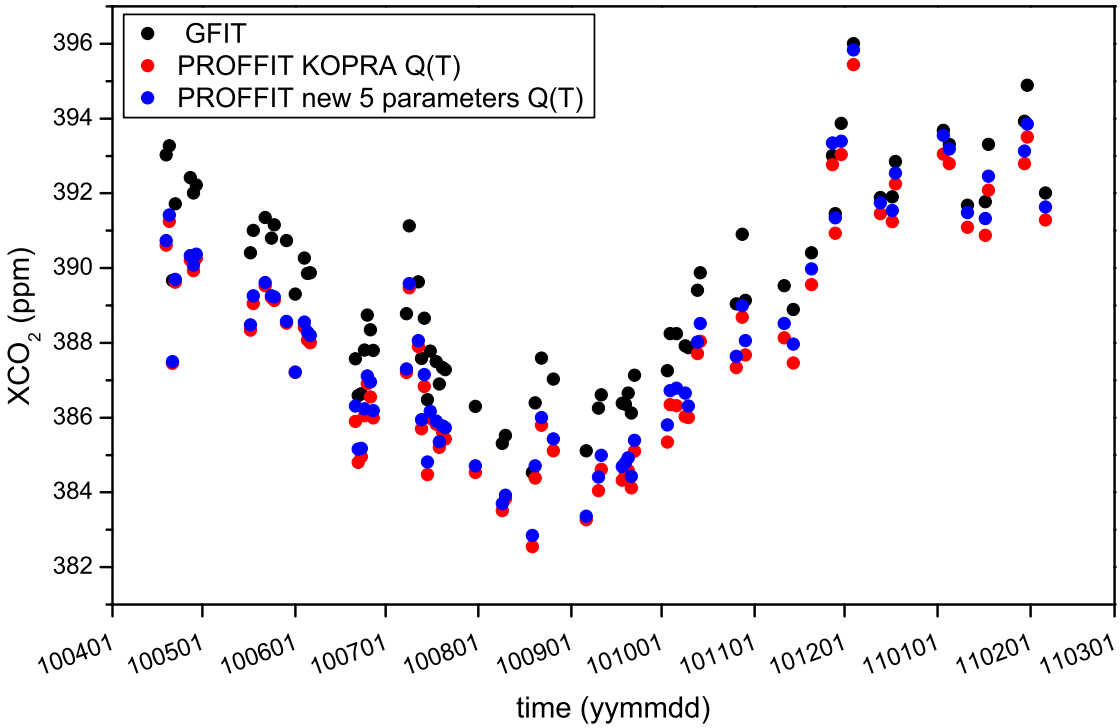

Figure 7.11: Karlsruhe time series of daily mean X_{CO_2} from April 2010 to March 2011 analyzed with PROFFIT using the KOPRA parametrization of $Q(T)$ (red) and the new 5 parameters setup (blue). Data analyzed with GFIT is illustrated in black.

Retrieval results of PROFFIT where the KOPRA parametrization is implemented are displayed in red, PROFFIT results with the use of the new 5 parameters setup in blue and results of GFIT in black. This comparison already indicates a reduction of the X_{CO_2} bias between PROFFIT and GFIT. In the corresponding correlation diagram

(Figure 7.12), where PROFFIT X_{CO_2} is plotted against GFIT X_{CO_2}, the differences between retrieval results can be determined in more detail. The regression line's standard deviations (SD) of the KOPRA setup (0.520 ppm, red) and the new 5 parameters setup (0.593 ppm, black) are nearly the same. In contrast, the bias between PROFFIT and GFIT retrieval results is reduced from 0.42% to 0.35% being an improvement in the course of adjusting the two codes.

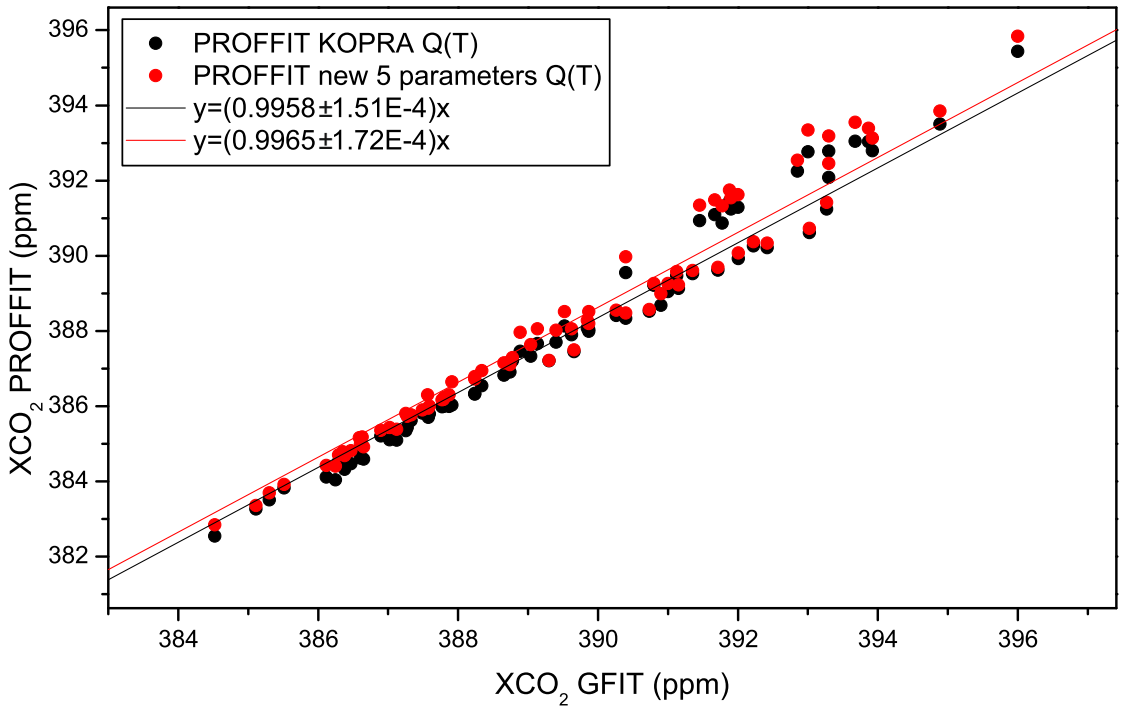

Figure 7.12: Correlation diagram between Karlsruhe X_{CO_2} data analyzed with PROFFIT and GFIT. PROFFIT results retrieved with the KOPRA parametrization are shown in red, while results using the new 5 parameters setup are illustrated in black.

7.5 Implementation of GFIT a priori profiles

Concerning the analysis of ground-based FTIR spectra, the kind of implemented a priori profile is important as well. Within TCCON a pure scaling retrieval is used to determine total columns of X_{CO_2}, where the included a priori profile is simply scaled. All PROFFIT results presented in this chapter have been determined by use of a scaling retrieval as well.

Regarding PROFFIT, the same a priori profile is used for every measurement in common CO_2 retrievals. In the case of Karlsruhe a climatology of the Whole Atmosphere

Community Climate Model (WACCM[9]) composed of 49 levels from the ground to up to 120 km is implemented. In contrast, GFIT retrievals use different empirical modeled profiles for each day, which are based on fits of GLOBALVIEW[10] data and exist up to an altitude of 10 km. Above this height, age-dependent profiles are assumed [Wunch et al., 2011].

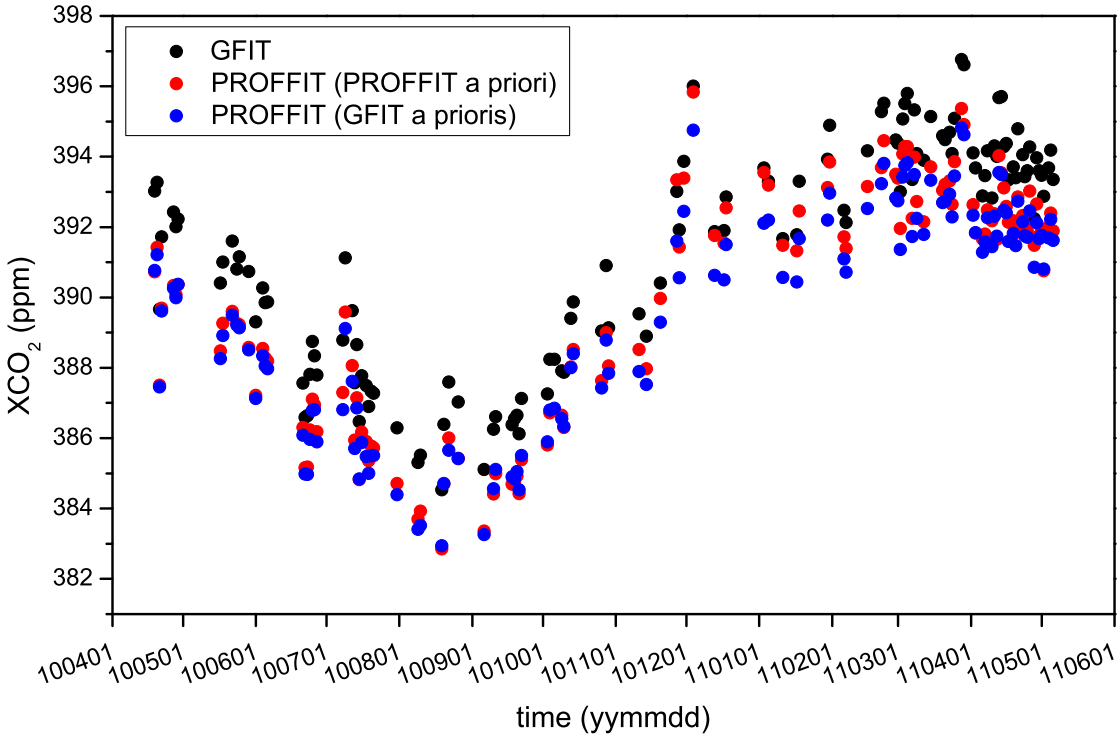

Figure 7.13: Time series of daily mean X_{CO_2} for Karlsruhe from April 2010 to May 2011, where retrievals of PROFFIT using the former PROFFIT a priori profile are shown in red, results of PROFFIT with implemented GFIT a priori profiles in blue and results of GFIT in black.

In the course of adjusting retrieval results of PROFFIT and GFIT, and to determine the influence of using different a priori profiles within the retrieval, the temporally variable GFIT a priori profiles were implemented in PROFFIT. Time series of daily mean X_{CO_2} for Karlsruhe from April 2010 to May 2011 are presented in Figure 7.13, where retrievals of PROFFIT using the former PROFFIT a priori profile are shown in red, results of the PROFFIT setup with implemented GFIT a priori profiles in blue and results of GFIT in black. It becomes apparent that the implementation of different

[9]http://www.cesm.ucar.edu/working_groups/WACCM/
[10]http://www.esrl.noaa.gov/gmd/ccgg/globalview/co2/co2_intro.html

a priori profiles lead to non negligible effects in resulting X_{CO_2} values, while it is not obvious if these differences are systematic.

In order to investigate this effect in more detail, the corresponding correlation plot is shown in Figure 7.14, where PROFFIT X_{CO_2} is plotted against GFIT X_{CO_2}. The former PROFFIT setup is illustrated in red, while the new setup is shown in black. Concerning the adaption, a strong improvement is clearly visible. While the comparison between the former PROFFIT setup and GFIT indicates a large scatter especially for high X_{CO_2} values during winter and the beginning of spring (SD=0.509 ppm), this scatter is reduced by use of the new setup with implemented GFIT a priori profiles (SD=0.265 ppm). The bias between PROFFIT and GFIT is a little larger (old setup: 0.36%, new setup: 0.46%) but now the same over the entire range.

The used a priori profile has a significant impact on retrieved total column results. Therefore it is preferable to implement the most accurate a priori profile within the retrieval. By means of profile retrievals, which are presented in Chapter 8, vertical CO_2 profiles can be determined from TCCON measurements and then used as a priori profiles in common retrievals. This might lead to an improvement of total column accuracies.

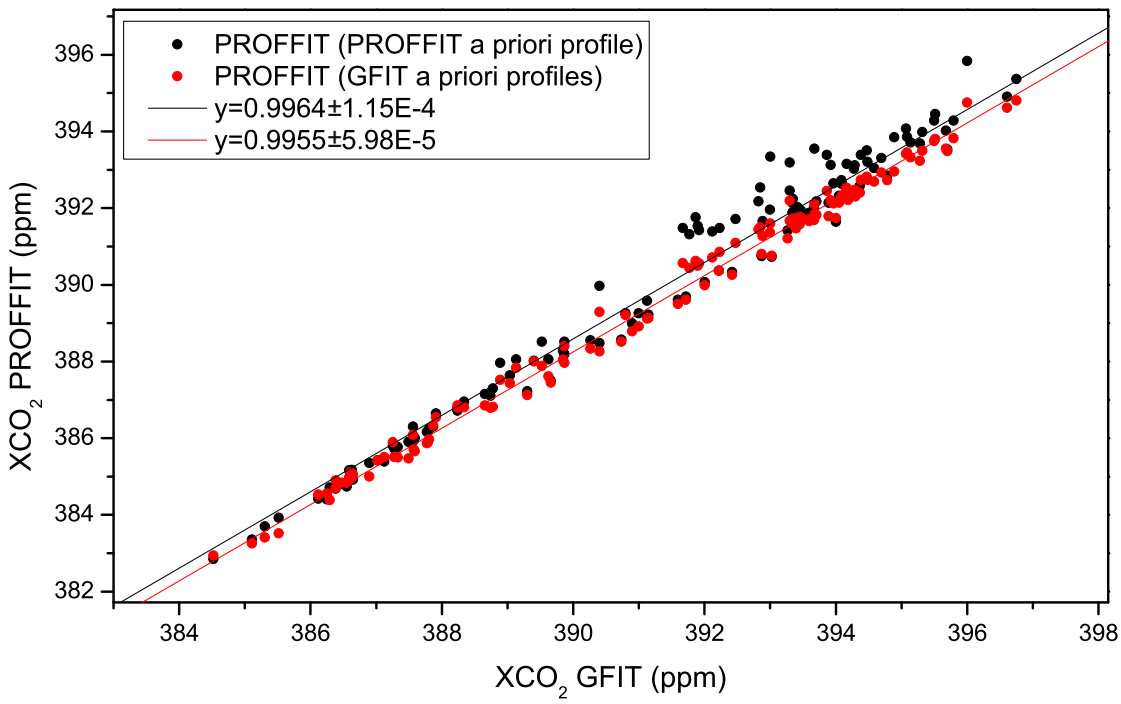

Figure 7.14: Correlation diagram between Karlsruhe X_{CO_2} of PROFFIT and GFIT. PROFFIT results retrieved with the former PROFFIT a priori profile are shown in red, while results using GFIT a priori profiles are illustrated in black.

7.6 Implementation of GFIT pressure-temperature profiles

As already described in Section 4.4, the knowledge of the vertical pT profile during a measurement is important in order to achieve high quality retrieval results. Due to the absence of continuous in situ measurements of temperature and pressure at FTIR sites (most TCCON sites only possess ground-based in situ measurements), model data are used within the retrievals. Both in PROFFIT and GFIT, models provided by NCEP are used, which can be received in different ways.

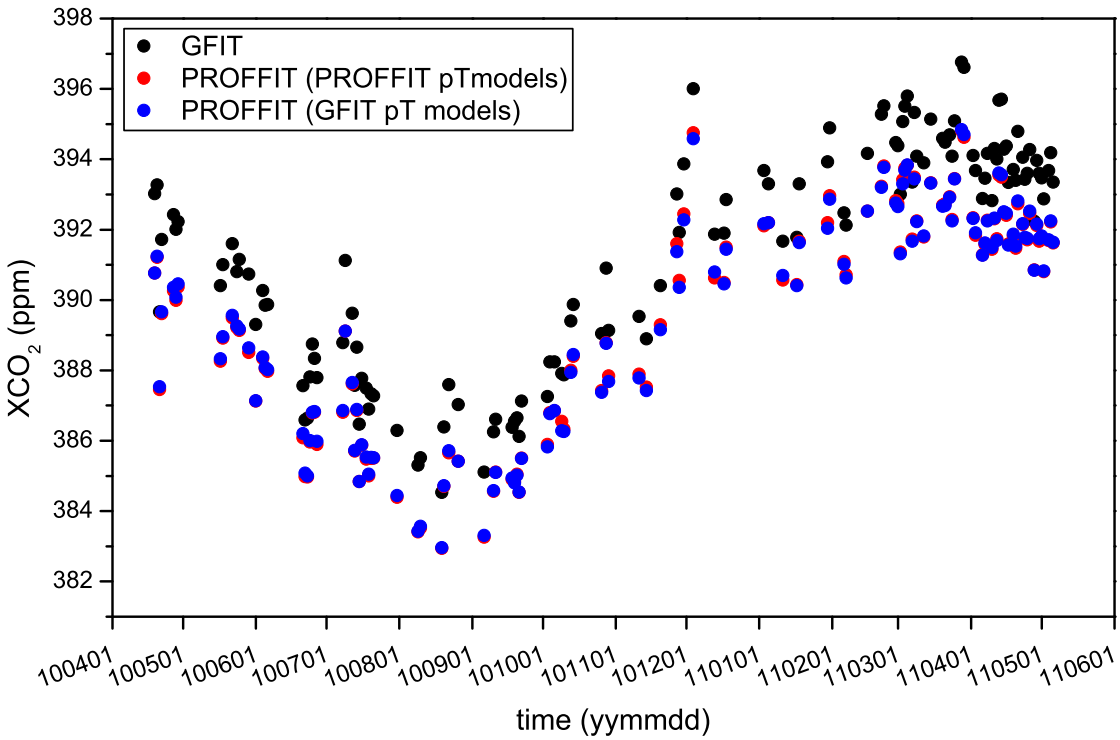

Figure 7.15: Time series of daily mean X_{CO_2} for Karlsruhe from April 2010 to May 2011, where PROFFIT results using the PROFFIT pT profiles are shown in red, results of the new PROFFIT setup (GFIT pT profiles) in blue and GFIT results in black.

For the use in PROFFIT, an email including date and location of the site is sent to the Goddard Automailer (operated by L. R. Lait, P.A. Newman and M.R. Schoeberl at NASA Goddard Space Flight Center[11]). The replied email contains the pT profile of the desired day (at 12 AM) up to an altitude of 45 km. In GFIT, 6-hourly pT profiles for a certain location and time are downloaded via the website of the National Oceanic

[11] http://acdb-ext.gsfc.nasa.gov/Data_services/automailer/

& Atmospheric Administration (NOAA[12]) and interpolated to local noon. In contrast to the use of the Goddard Automailer, it is also possible to download longer time series of models at once via the NOAA web page. To further enhance the comparability be-

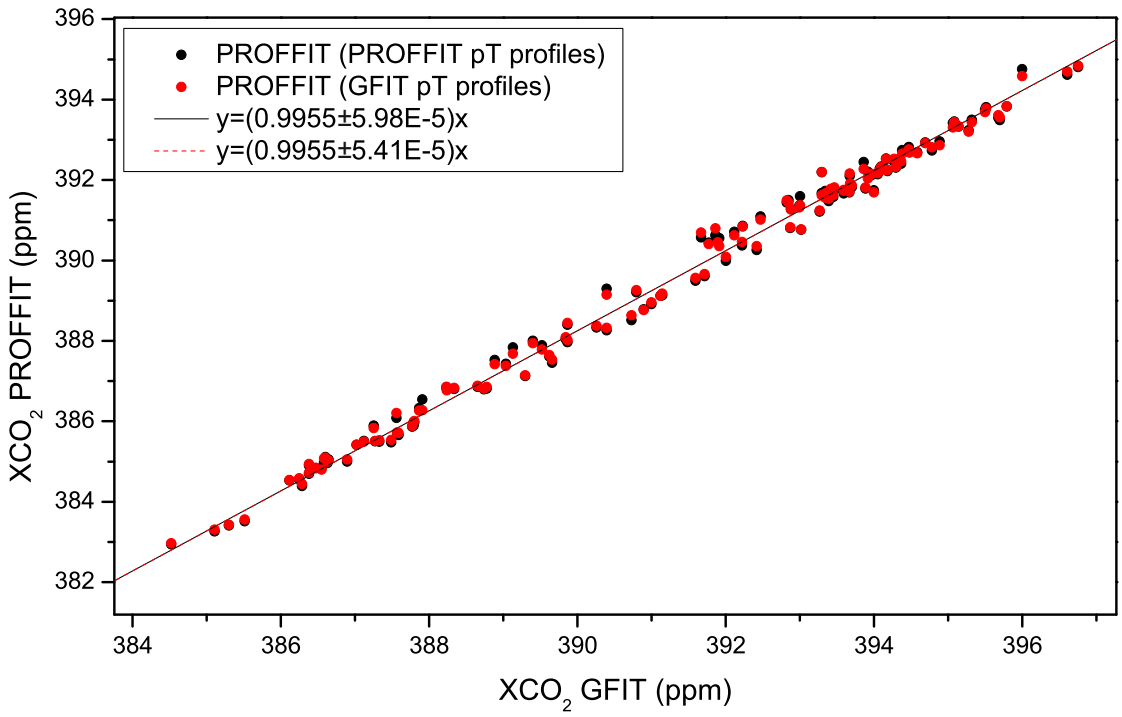

Figure 7.16: Correlation diagram between Karlsruhe X_{CO_2} of PROFFIT and GFIT. PROFFIT results using the PROFFIT pT profiles are shown in red, while results using the new setup with implemented GFIT pT profiles are illustrated in black.

tween PROFFIT and GFIT retrieval results, GFIT pT profiles were implemented in the PROFFIT analysis. The Karlsruhe time series of daily mean X_{CO_2} from April 2010 to May 2011 for the different setups is illustrated in Figure 7.15, where PROFFIT results using the PROFFIT pT profiles are shown in red, results of the new setup with implemented GFIT pT profiles in blue and GFIT results in black. The diagram indicates only slight differences between the results.

To investigate the changes in more detail, the corresponding correlation plot is shown in Figure 7.16, where PROFFIT X_{CO_2} is plotted against GFIT X_{CO_2}. Results retrieved with the former PROFFIT setup are displayed in red, while retrieval results of the new setup with GFIT pT profiles are shown in black. Both regression lines indicate exactly the same slope, which means that the bias between the results of the two codes (0.46%)

[12] www.esrl.noaa.gov/psd/data/gridded/data.ncep.reanalysis.html

has not been changed. Regarding the scatter, only slight differences are visible where the standard deviation changed from 0.265 ppm to 0.240 ppm.
In summary, the implementation of GFIT pT profiles within PROFFIT indicates a near negligible effect, as it was expected, due to the same source of pT profiles with only two differences, being the way of getting the profiles and the use of 6 hourly profiles interpolated to local noon (GFIT) compared to profiles modeled for noon (PROFFIT).
Since Gisi [2012] showed that the use of several pT profiles within one day reduces disturbing effects in the retrieved O_2 column, the use of variable pT profiles during one day would be preferable for an improved TCCON retrieval setup.

7.7 Improvement of the solar line list

A ground-based solar absorption spectrum does not only consist of absorption lines caused by gases in the Earth's atmosphere but also by solar features generated in the

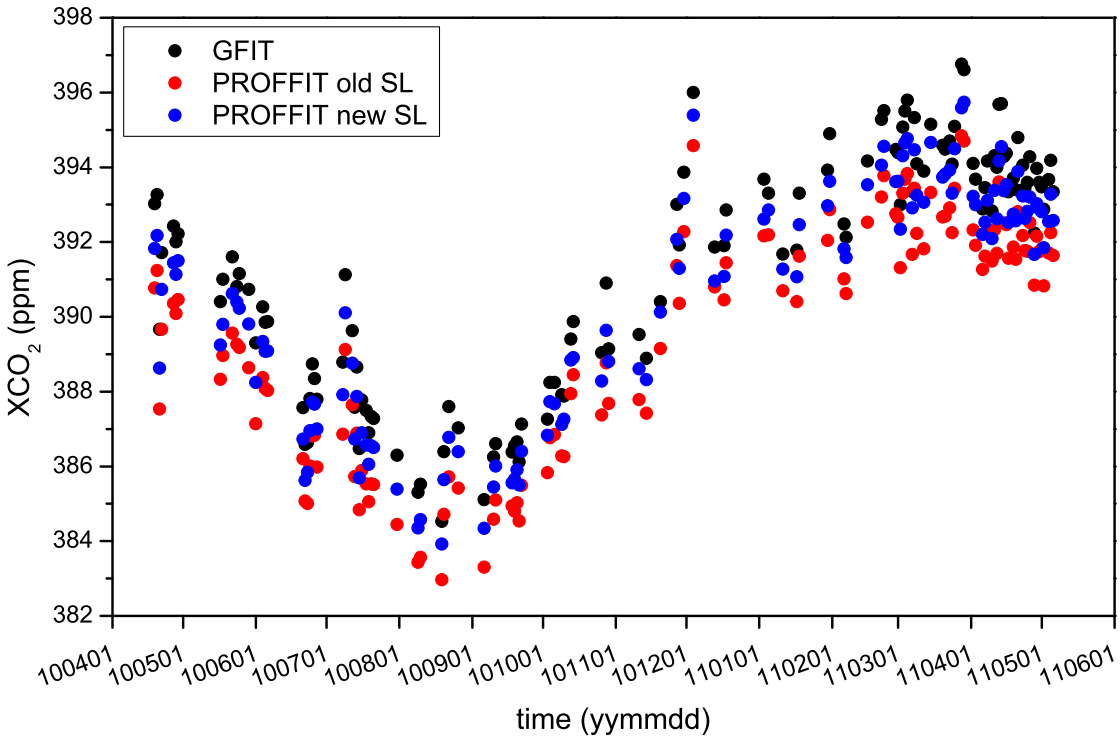

Figure 7.17: Karlsruhe time series of daily mean X_{CO_2} from April 2010 to May 2011. PROFFIT retrieval results with the use of the improved solar line list (SL) are shown in blue, results with the use of old line data are shown in red and GFIT results are illustrated in black.

atmosphere of the Sun. These lines have to be considered within the retrieval to avoid unwanted large residuals between measurement and fit. Therefore solar features are taken into account by using tabulated solar line data. In the course of this work, an improvement of solar lines for the NIR region based on the analysis of ground-based FTIR spectra [Hase, 2012b], has been compared to the previous PROFFIT line list. The influence of this improvement on resulting X_{CO_2} values is shown by means of the comparison with X_{CO_2} results retrieved with the old solar line list and additionally with GFIT retrievals, where a different solar line list is used.
The Karlsruhe time series of daily mean X_{CO_2} from April 2010 to May 2011 is illustrated in Figure 7.17, where PROFFIT results retrieved with old line data are shown in red, with new line data in blue and GFIT results in black.

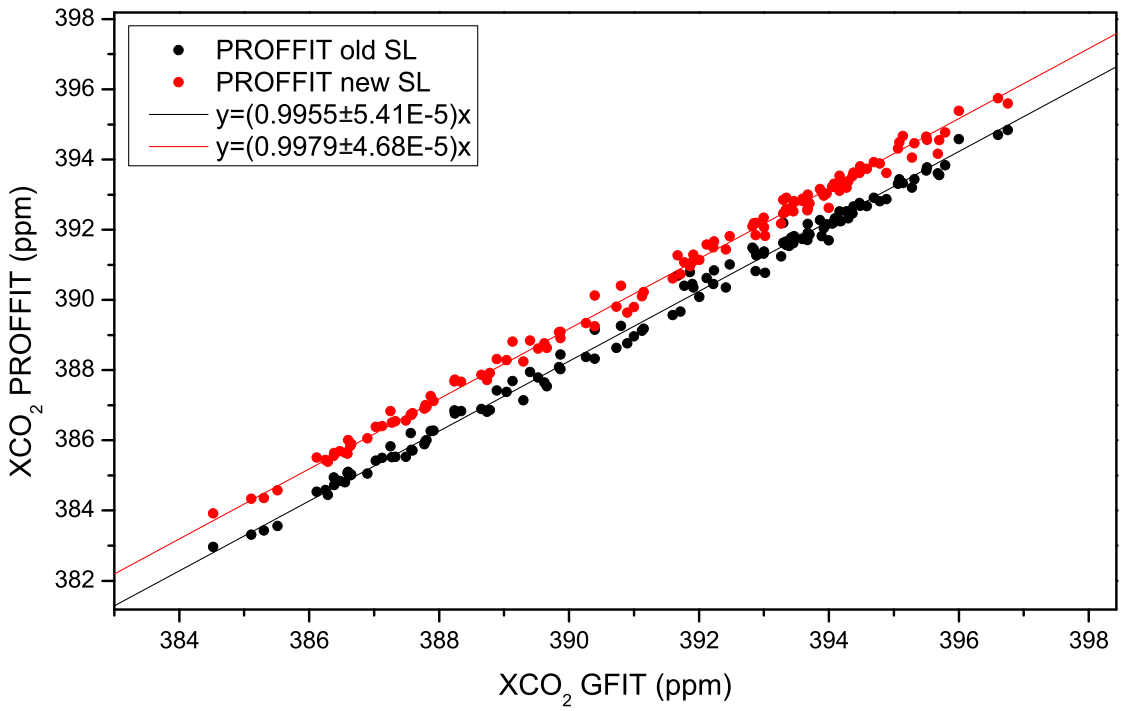

Figure 7.18: Correlation plot between X_{CO2} values of PROFFIT and GFIT. Retrievals using the old solar line list are shown in red, while results using the improved solar line list are illustrated in black.

There is a large difference between X_{CO_2} values for the different PROFFIT setups due to the reduction of fit residuals. The discrepancies between PROFFIT and GFIT is reduced by using the improved solar line list as well. By means of the corresponding correlation diagram (Figure 7.18), where PROFFIT X_{CO_2} is plotted against GFIT X_{CO_2}, this can be verified. The bias between PROFFIT and GFIT X_{CO_2} values is

strongly reduced from 0.46% (black, old solar line list) to 0.21% (red, new solar line list), where most of the effect is due to changes in CO_2. Regarding the scatter, changes are only small, with a reduction of the standard deviation from 0.240 ppm to 0.207 ppm.

In summary, the optimization of the solar line list not only causes a strong improvement concerning the residuals between fit and measurement in PROFFIT but also leads to a considerable reduction of the bias between PROFFIT and GFIT retrieval results.

7.8 Implementation of the GFIT O_2 line list

As mentioned in the previous sections, the line list (including e.g. line strengths and temperature dependences) used within the retrieval has a large impact on total column results. In PROFFIT, different line lists are implemented, depending on the kind of molecule. For CO_2 a modified HITRAN 2008 line list is used, where air-broadening widths were improved (see Section 7.1) and line mixing parameters were implemented

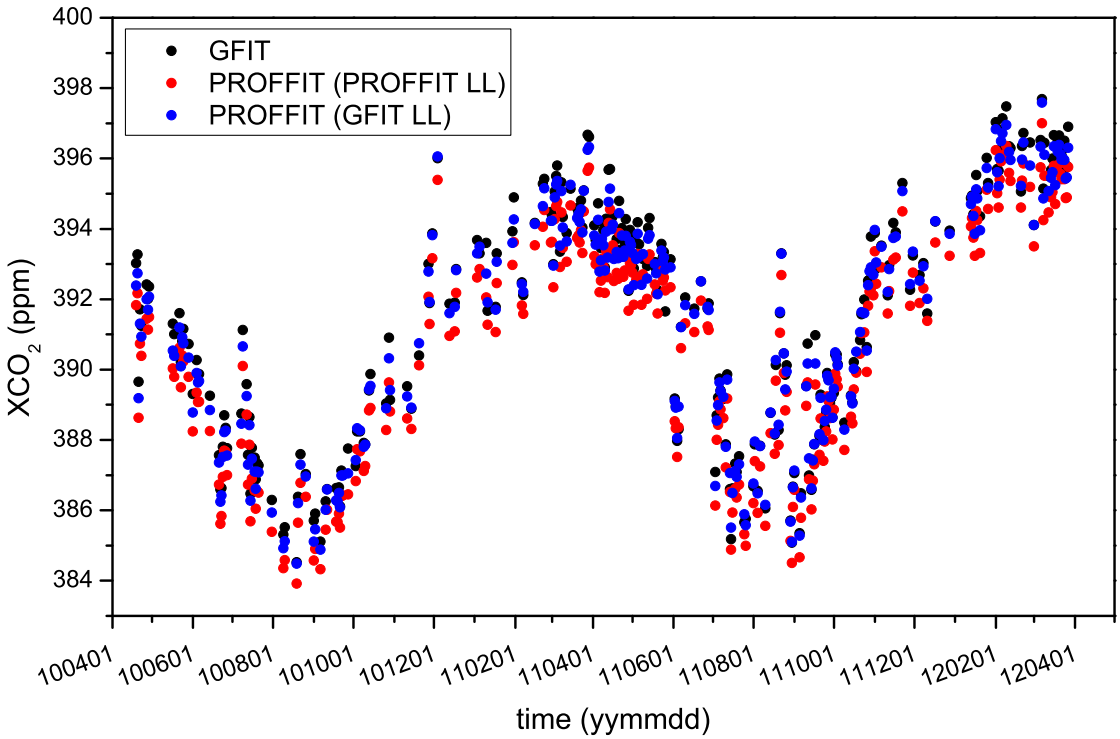

Figure 7.19: Karlsruhe time series of daily mean X_{CO_2} from April 2010 to May 2011. PROFFIT retrieval results including the GFIT O_2 line list (LL) are shown in blue, PROFFIT results using the PROFFIT O_2 line list are shown in red and GFIT results are illustrated in black.

(see Section 7.2). Concerning O_2 the original HITRAN 2009 line list is applied.
Within the GFIT analysis, line lists originating from different sources are used. For CO_2 and the region above 4300 cm^{-1}, the line list of Toth et al. [2008] is included, while the O_2 line list is based on laboratory measurements of Newman et al. [1999] (modified in accordance with Yang et al. [2005]) and quadrupole lines from Gordon et al. [2010]. CIA is fitted based on laboratory measurements by Smith and Newnham [2000].
In the course of adjusting retrieval results of PROFFIT and GFIT, and in order to detect the line list's impact on the retrieval results, the GFIT O_2 line list was implemented in PROFFIT. The absence of air mass dependent effects in O_2 total column amounts retrieved by the use of the GFIT O_2 line list has already been shown in Section 7.1. Due to the modification of air-broadening widths and the implemented line mixing feature in the PROFFIT CO_2 line list, this line list will not be replaced by the GFIT line list within future retrievals.
In Figure 7.19, the Karlsruhe time series of daily mean X_{CO_2} from April 2010 to March 2012 is illustrated, where PROFFIT results including the GFIT O_2 line list are shown

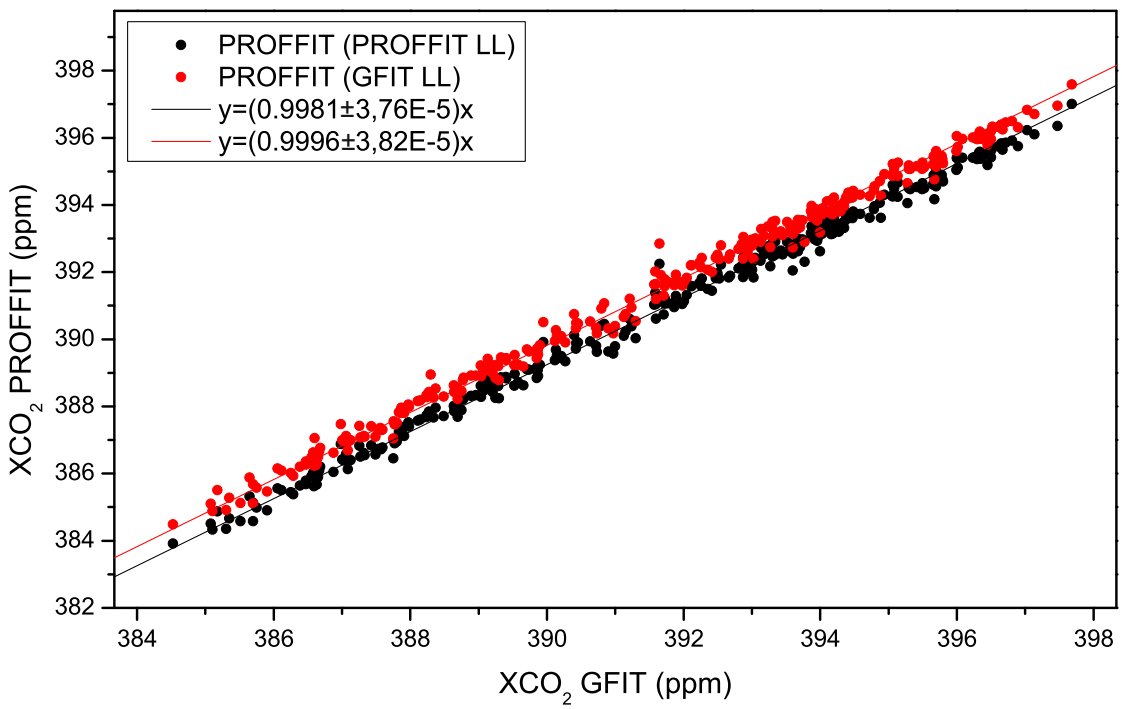

Figure 7.20: Correlation plot between X_{CO2} values of PROFFIT and GFIT. PROFFIT results using the PROFFIT line list are shown in red, while results using the GFIT O_2 line list are illustrated in black.

in red, PROFFIT results using the PROFFIT line list are shown in blue and GFIT results are displayed in black. There are large discrepancies between PROFFIT retrievals including different line list setups, where results of PROFFIT with implemented GFIT O_2 line list are now very similar to GFIT results. This should be verified by means of the corresponding correlation plot (Figure 7.20), where PROFFIT X_{CO_2} is plotted against GFIT X_{CO_2}. Retrievals using the PROFFIT line list are shown in red, while results using the GFIT line list are illustrated in black. The strong reduction of the bias between PROFFIT and GFIT results to one fourth of the former value (from 0.20% to 0.05%) is clearly visible. In contrast, the scatter remains nearly unaffacted ($\mathrm{SD}_{PROFFIT\ LL} = 0.250$ ppm, $\mathrm{SD}_{GFIT\ LL} = 0.253$ ppm).
To sum up, results retrieved with different line list setups indicated strong differences which have to be considered. After the implementation of the GFIT O_2 line list within PROFFIT, differences between total column results of the two codes become very small (0.05%).

7.9 Intercomparison between PROFFIT and GFIT

Retrieval results of X_{CO_2} are only accepted for public distribution within TCCON if data were analyzed with the GFIT software. In the previous sections, not only the influence of several error sources within the radiative transfer and the retrieval on resulting total columns amounts was determined, but also adjustments between the two codes PROFFIT and GFIT were carried out. These are in detail the reparametrization of partition functions (Section 7.4) and the implementation of GFIT a priori profiles (Section 7.5), GFIT pT profiles (Section 7.6) and the GFIT O_2 line list (Section 7.8), where the optimization of the solar line list (Section 7.7) also led to an improvement of the comparability between the two codes.

In this section, the adjustment's overall effect on the comparability between X_{CO_2} results of PROFFIT and GFIT will be finally described and compared with the initial status of 2011. The Karlsruhe time series of daily mean X_{CO_2} from April 2010 to March 2011 analyzed with PROFFIT and GFIT, and the corresponding correlation plot are shown in Figure 7.21. This is the initial status of 2011, where no adjustment between

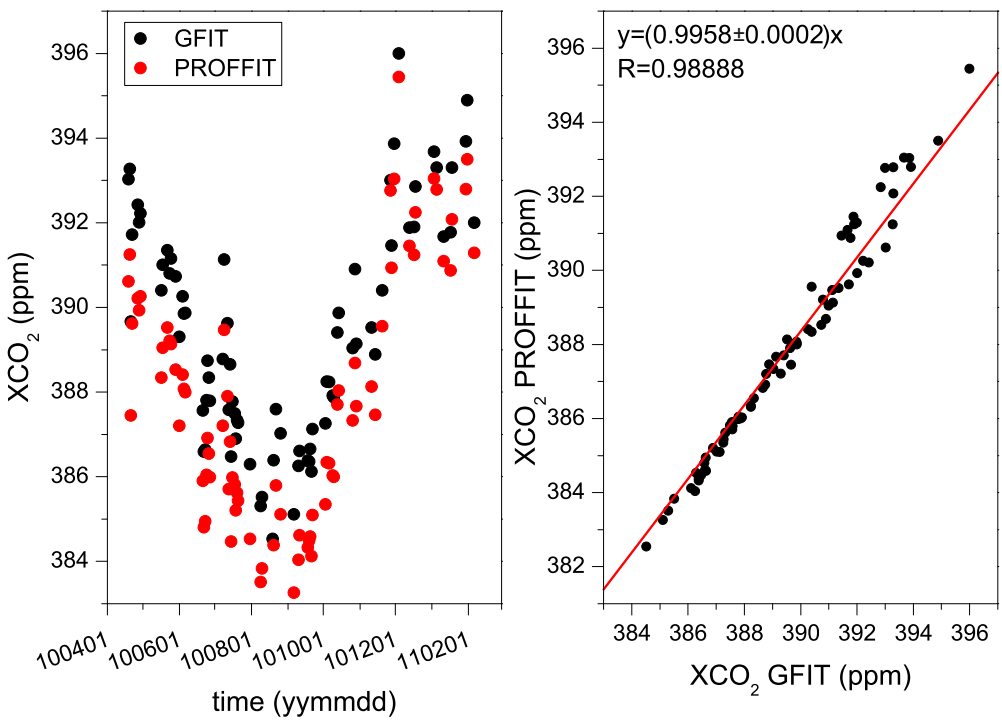

Figure 7.21: Left: Karlsruhe time series of daily mean X_{CO_2} from April 2010 to March 2011 analyzed with PROFFIT and GFIT using the setups of 2011. Right: Correlation plot between X_{CO_2} values of PROFFIT and GFIT (initial status of 2011).

the codes were made. There is a good correlation, but the bias between PROFFIT and GFIT results (about 0.42%) is not negligible likewise the scatter especially for large X_{CO_2} values.

Figure 7.22 shows the same plot as Figure 7.21 but for the final comparison status of 2013 by means of an expanded period (April 2010 to May 2012). In addition to the already mentioned changes, temporally variable pT profiles were implemented within the PROFFIT setup [Gisi, 2012], while GFIT makes use of ground level tall tower temperature and pressure measurements (provided by M. Kohler at KIT Campus North).

Including all adjustments and improvements, the bias between PROFFIT and GFIT X_{CO_2} was reduced to 0.03%, where the standard deviation also decreased from 0.520 to 0.194 ppm. The presented results demonstrate the successful cross-validation of the two major codes for the analysis of ground-based FTIR measurements in the NIR region.

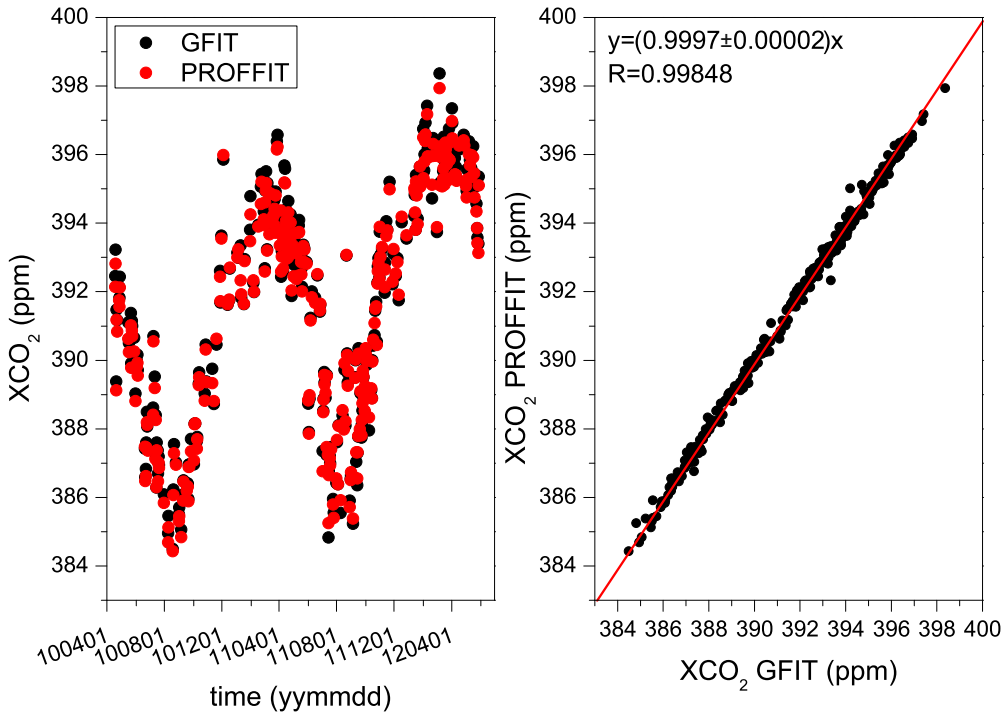

Figure 7.22: Left: Karlsruhe time series of daily mean X_{CO_2} from April 2010 to May 2012 analyzed with PROFFIT and GFIT using the final setups of 2013. Right: Correlation plot between X_{CO_2} values of PROFFIT and GFIT (status of 2013).

7.10 Air mass dependence

In addition to the successful cross-validation of PROFFIT and GFIT, the intercomparison revealed shortcomings of the operational TCCON retrieval as well. Within a common GFIT analysis, retrieved total column results usually undergo a post processing procedure, in which several empirical corrections are applied to the data [Wunch et al., 2011]. One of these corrections is the so called in situ correction, where gas specific in situ correction factors are used to scale FTIR results (0.989 for X_{CO_2}) onto the WMO network's scale. Another important correction inside the routine is the air mass correction.

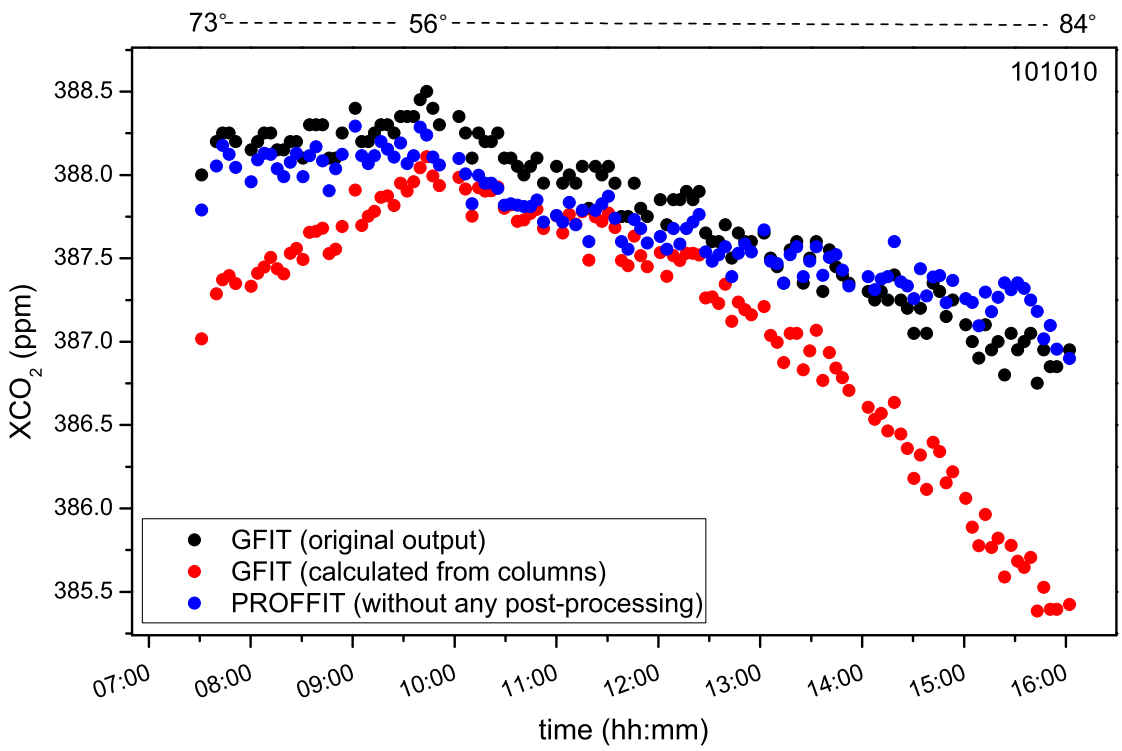

Figure 7.23: X_{CO_2} total column results for October 10th, 2010 at Karlsruhe (7:30 AM to 4:00 PM). PROFFIT results are illustrated in blue, GFIT results without post processing in red and original GFIT retrievals including post processing in black.

As already described in Section 7.1, air mass effects appear as systematic differences between results from measurements at noon and measurements at sunrise or sunset. The disregard of these effect leads to erroneous values in the seasonal cycle of X_{CO_2} due to the SZA's variation depending on season and latitude, leading to differences between the sites. Instead of correcting the air mass effect at its source, an empirical

post correction is applied within the common TCCON analysis, which is described in more detail in Wunch et al. [2010] and Deutscher et al. [2010].
Unlike GFIT, there are no air mass dependent post corrections at all during retrievals with PROFFIT, only the global in situ correction factor of 0.989 for X_{CO_2} was applied.

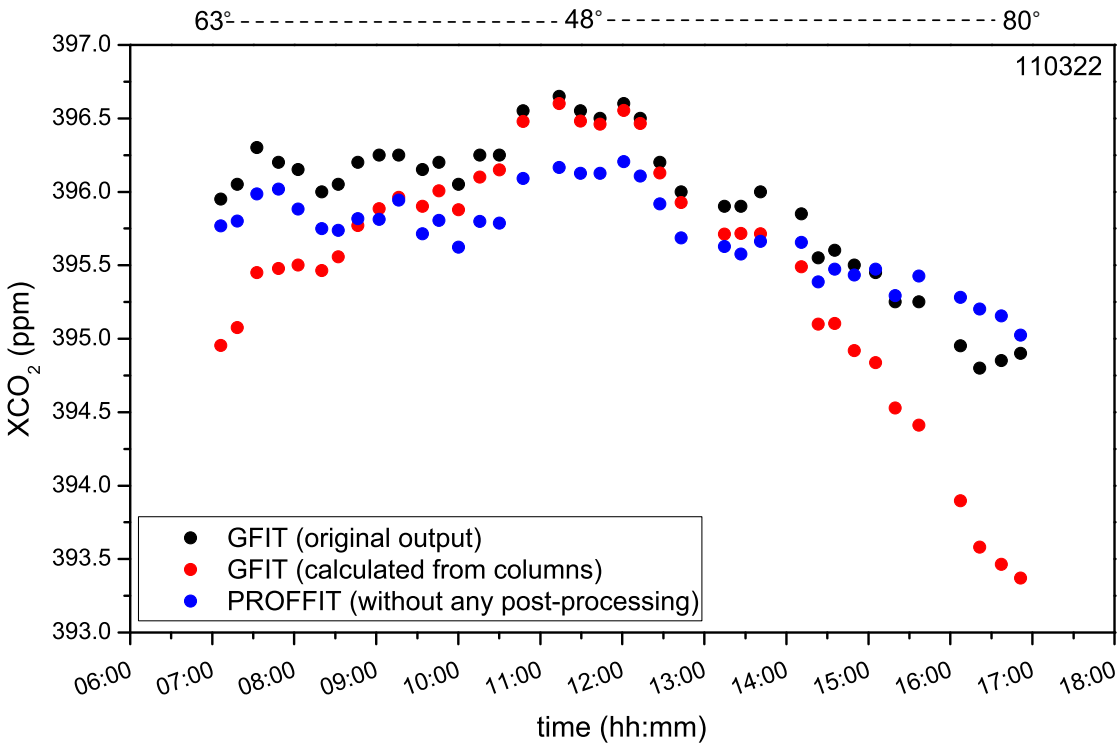

Figure 7.24: X_{CO_2} total column results for March 22nd, 2011 at Karlsruhe (7:00 AM to 5:00 PM). PROFFIT results are illustrated in blue, GFIT results without post processing in red and original GFIT retrievals including post processing in black.

In Figures 7.23 and 7.24 Karsruhe X_{CO_2} values for two different days are presented. Data analyzed with PROFFIT are shown in blue, retrievals of GFIT including post processing are shown in black and data analyzed with GFIT without using the post processing routine are illustrated in red. Both plots indicate the same structure. GFIT X_{CO_2}, which was retrieved without post processing (red), shows a strong air mass dependence with an increase of X_{CO_2} until noon followed by a decrease of concentration. For original GFIT results (black) this effect is only slightly visible, due to the applied air mass correction during the post processing procedure. Concerning PROFFIT, where no air mass correction is applied, no air mass dependencies can be determined in the retrieved X_{CO_2} time series of either Figures. The retrieved X_{CO_2} values are

similar to the ones retrieved with the original GFIT setup, nevertheless there are small differences between the results probably contributing to the remaining bias between PROFFIT and GFIT described in Section 7.9. But why does this effect only occur in retrievals with GFIT? Air mass dependent effects are caused by uncertainties in the spectroscopy, like erroneous line widths or the negligence of line mixing. In order to investigate the reason for air mass dependencies in GFIT X_{CO_2}, total column results of CO_2 and O_2 have to be considered separately. Due to the fact that air mass dependencies are also apparent in GFIT O_2 columns, the line list and the negligence of line mixing are not the reason for the air mass dependence in GFIT, because PROFFIT makes use of the same GFIT O_2 line list. The most likely reason is therefore the different implementation of CIA and the lack of an extended baseline fit in GFIT.
Concerning the strict requirements of the TCCON, these effects have to be eliminated. Indeed, these errors are corrected empirically, but a correction at the source would be preferable to ensure the high accuracy and quality of the data. Therefore an investigation of the effect's source is recommended.

7.11 Conclusions

Ground-based FTIR measurements have to be analyzed accurately in order to provide high quality data products. In the course of this work, the PROFFIT analysis procedure for CO_2 from NIR spectra was created and stepwise improved to ensure this high quality.
Air mass dependent effects in the total column of CO_2 were minimized by modifying the CO_2 air-broadening widths. The implementation of line mixing and the improvement of the solar line list led to a reduction of the residuals between fit and measurement, where the use of the new CIA feature turned out to be dispensable if an extended baseline fit is used. In summary, the accuracy of 0.05–0.12% in X_{CO_2} for measurements at Karlsruhe was improved by up to 50%.
By means of a comparison between PROFFIT and GFIT the impact of several error sources within the forward calculation and the retrieval was analyzed. Modifications within the PROFFIT setup like the improvement of the solar line list, the reparametrization of partition functions, and the implementation of GFIT a priori profiles, GFIT pT profiles and the GFIT O_2 line list led to a reduction of differences between X_{CO_2} results of the two codes. After all changes the bias between PROFFIT and GFIT X_{CO_2} was strongly reduced from 0.42% to 0.03%, where the standard deviation decreased from 0.520 ppm to 0.194 ppm as well. The influence of each modification

	Bias	SD (ppm)
Status of 2011	**0.42%**	**0.520**
$Q(T)$	0.35%	0.593
A priori profiles	0.46%	0.265
pT profiles	0.46%	0.240
Solar line list	0.21%	0.207
O_2 line list*	0.05%	0.250
Status of 2013**	**0.03%**	**0.194**

Table 7.1: The influence of each modification within the PROFFIT setup on the bias and standard deviation between PROFFIT and GFIT X_{CO_2} results. (*extended time series; **including an additional pT update)

is summarized in table 7.1. These results demonstrate the successful cross-validation of PROFFIT and GFIT and indicate that PROFFIT represents an alternative for the analysis of NIR spectra within the TCCON.

In addition the cross-validation of PROFFIT and GFIT revealed shortcomings of the operational TCCON retrieval. In contrast to PROFFIT, GFIT X_{CO_2} results show a significant air mass dependence. These discrepancies are most likely due to the different implementation of the CIA feature and the lack of an extended baseline fit within GFIT. In order to ensure the high quality standard of the TCCON, this error has to be corrected at its source instead of applying an empirical post correction, as it is currently done within the common TCCON analysis.

Chapter 8

CO_2 profile retrievals from TCCON spectra

Within the TCCON, ground-based high-resolution FTIR spectra of the NIR region are used to retrieve total gas columns of CO_2, being an essential contribution for the validation of satellite data and the investigation of the carbon cycle. However, the determined total column contains no information about the vertical profile of CO_2, due to the use of a scaling retrieval where the a priori profile is simply scaled.
In contrast to the common TCCON analysis where the GFIT code only provides the opportunity of doing a scaling retrieval, the PROFFIT code has the ability to determine vertical gas profiles by performing a profile retrieval. In those retrievals, the pressure broadening effect of absorption lines is used to retrieve vertical gas profiles. Weakly broadened lines originate from higher altitudes, whereas strongly broadened lines originate from lower atmospheric levels. For gases in the MIR region, such profile retrievals are already commonly performed by means of the PROFFIT software [Sepúlveda et al., 2012]. However, due to mostly unsaturated lines in the NIR region and the low variability of the true CO_2 profile compared to the a priori profile, the performance of CO_2 profile retrievals using TCCON spectra pose a big challenge.
In the course of this Ph.D. thesis, an analysis procedure for retrievals of vertical CO_2 profiles from TCCON spectra was developed. This procedure aims at improving the retrieval information content and optimizing the column sensitivity. With this enhanced information content, the retrieved profiles are of great interest for the CO_2 modeling community to investigate the carbon cycle. Currently aircraft measurements are used to consider the vertical transport within the models. Compared to these only sparsely available measurements, the implementation of continuous profiles from TCCON measurements would be a great improvement.

In addition the determined vertical CO_2 profiles can be used as a priori profiles within the common TCCON scaling retrieval to improve total column accuracies.
In this chapter, the developed analysis procedure for profile retrievals of CO_2 will be presented, beginning with the description of the setup in Section 8.1. Afterwards the determined profiles will be shown and compared to in situ values for Izaña in Section 8.2. Section 8.3 deals with the validation of retrieved profiles by means of aircraft measurements at Lamont. The problem of an unrealistically high intraday variability of CO_2 profiles will be investigated on the basis of sensitivity studies in Section 8.4, while Section 8.5 concludes Chapter 8.

8.1 PROFFIT profile retrieval setup

In order to retrieve vertical CO_2 profiles from TCCON measurements by means of PROFFIT profile retrievals, an applicable PROFFIT retrieval setup has to be found being a challenging task by itself. First, a suitable microwindow has to be selected, containing CO_2 lines with reasonable intensities and as little absorption lines of in-

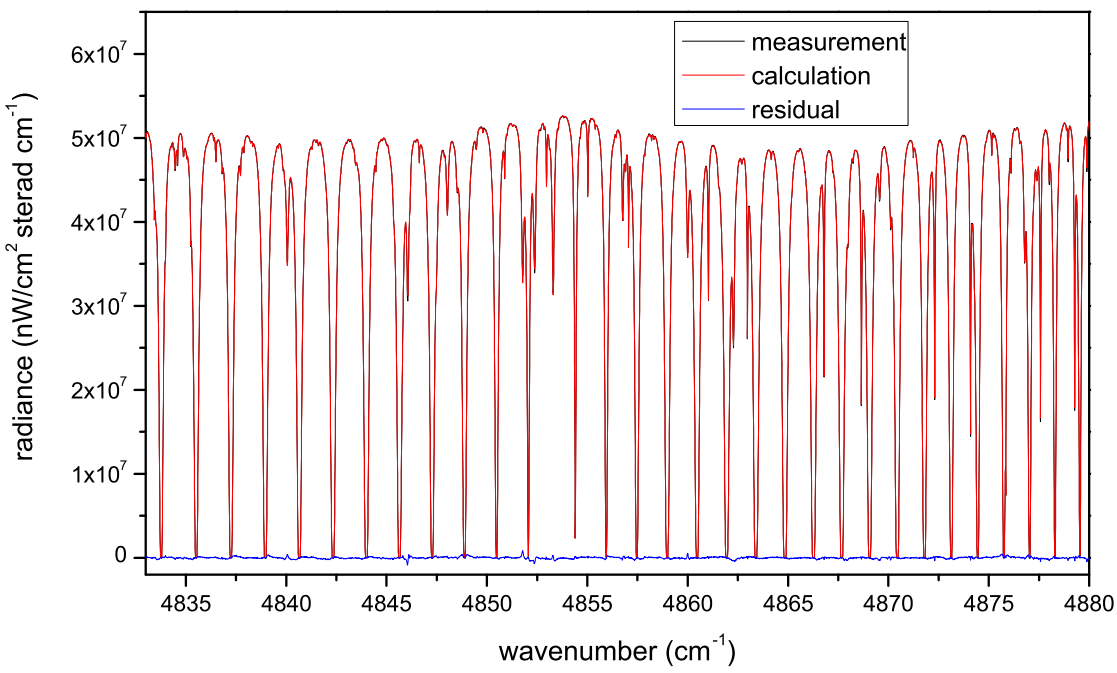

Figure 8.1: CO_2 microwindow (4833–4880 cm^{-1}), which is used to retrieve vertical profiles of CO_2 by means of the PROFFIT code. The measured spectrum is shown in black, the fitted spectrum in red and the residual between fit and measurement in blue.

terfering species. Due to the low line intensities, the use of the standard TCCON microwindows for CO_2 (see Section 4.3) turned out to be difficult. Therefore a new microwindow in the NIR region with acceptable lines and intensities had to be found, where the microwindow from 4833–4880 cm^{-1} proved to be suitable. This microwindow is illustrated in Figure 8.1, where the fitted spectrum is shown in red, the measured spectrum in black and the residuum between fit and measurement is illustrated in blue. Compared to the common TCCON microwindows for CO_2 (Section 4.3), the region between 4833 to 4880 cm^{-1} shows considerably larger line intensities ranging up to saturated values.

In addition to CO_2, the gases H_2O and CH_4 are also considered during the retrieval. However, they possess only unsaturated absorption features in this region. Within the retrieval, a modified HITRAN 2008 line list is used for CO_2 and the original HITRAN 2008 line list for CH_4, while for H_2O the HITRAN 2009 update is applied. In order to adjust the continuum shape of the spectral window, a 5 point baseline fit is applied by default. For the inversion, the method of Tikhonov-Phillips is selected, where constraints are regulated in such a way that resulting profiles usually have about 1.5 DOFs. As pT profiles, models from NCEP are applied (see Section 7.6). An ideal ILS is assumed in all retrievals.

For all measurements analyzed by means of profile retrievals in this work, the same

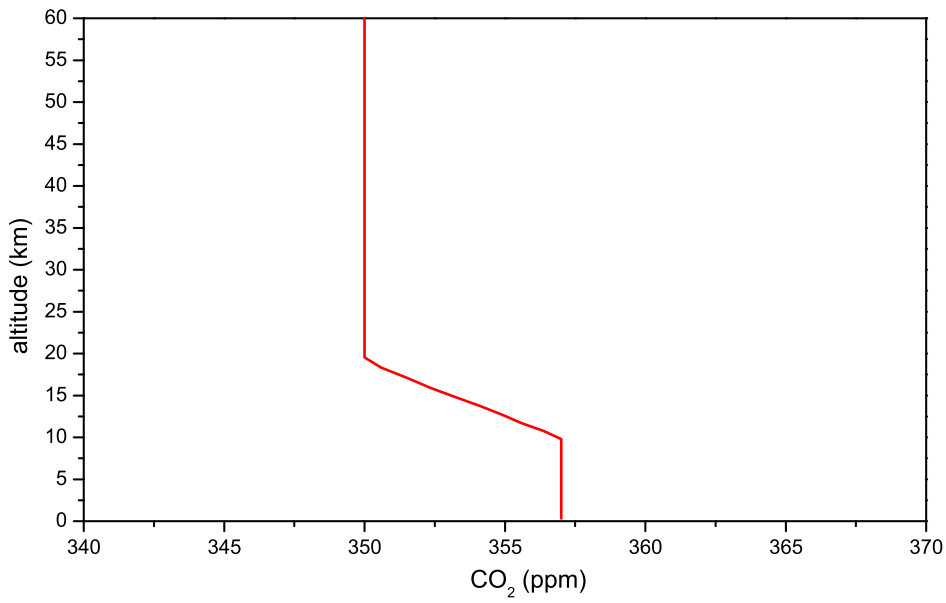

Figure 8.2: A priori profile of CO_2 which is used within PROFFIT profile retrievals for all measurements.

a priori profile is used, which is shown in Figure 8.2. Therefore differences in the retrieved profiles are not due to the application of variable a priori profile inputs. The a priori profile indicates constant CO_2 concentration up to an altitude of 10 km, while in the region between 10 and 20 km the concentration decreases by 7 ppm and remains constant again from 20 km upwards. Due to the used regularization method, only the shape of the a priori profile is important for the retrieval, where absolute values are irrelevant.

In Figure 8.3, typical sensitivities, resulting from a measurement analyzed with the described PROFFIT setup are illustrated as a function of altitude. It indicates large sensitivities for tropospheric levels (0–10 km), while the sensitivity strongly decreases for higher altitudes (10–60 km). However, this is not surprising due to large line intensities up to saturated lines in the used microwindow, containing more information about lower levels.

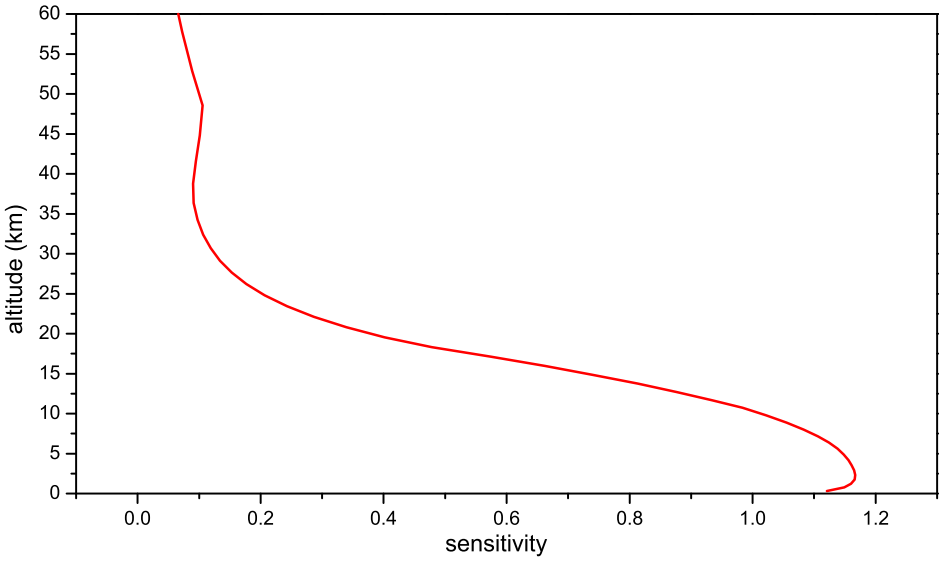

Figure 8.3: Typical sensitivities resulting from a measurement analyzed with the described PROFFIT profile retrieval setup.

8.2 Izaña results

In this section the determined vertical CO_2 profiles for Izaña will be shown and compared to co-located in situ ground measurements. The daily mean vertical profiles of CO_2 for Izaña, determined by use of the described PROFFIT analysis procedure, are

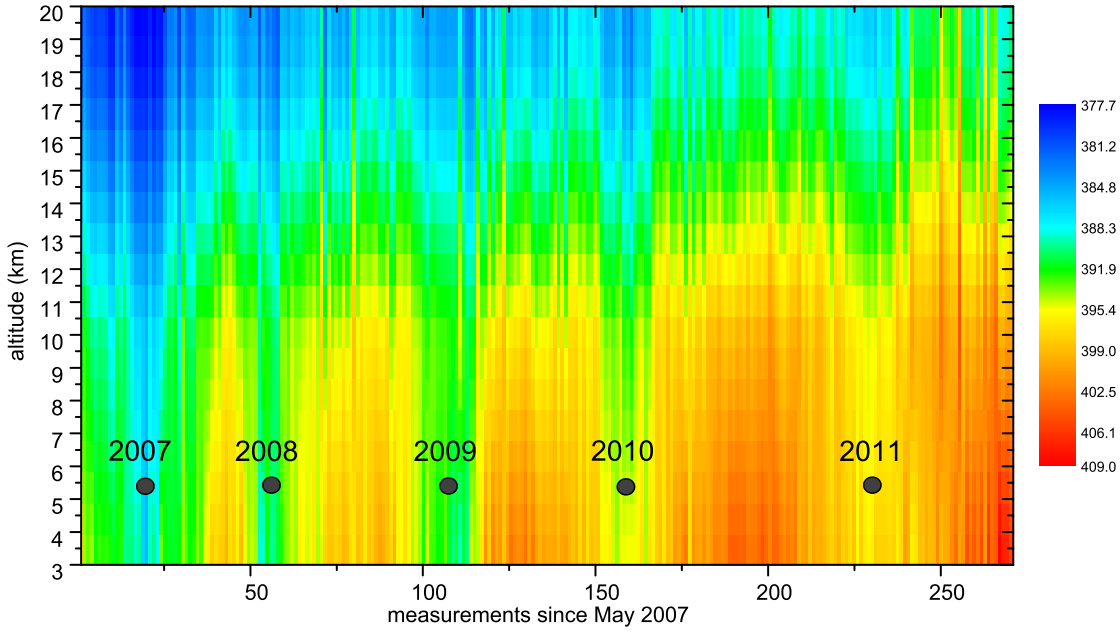

Figure 8.4: Daily mean vertical profiles of CO_2 at Izaña from May 2007 to May 2012, determined by use of the described PROFFIT analysis procedure, where the altitude is plotted against the number of measurements since May 2007 and different colors indicate the different CO_2 concentrations. CO_2 minima at the ground in September are labeled with the corresponding years.

shown in Figure 8.4 from May 2007 to May 2012. The altitude is plotted against measurements since May 2007 (days without measurements are not shown) and different colors represent different CO_2 concentrations. The annual cycle of CO_2 is clearly visible, where CO_2 minima at the ground in September are labeled with the corresponding years. The diagram also indicates an increase of CO_2 with time at all displayed altitudes (3–20 km), due to the shift of colors from dark blue to mainly green and red.
By comparisons of single profiles, differences in the shapes can be obtained, showing partially a large vertical slope. Nevertheless all profiles have in common that ground level CO_2 amounts are larger compared to higher levels. In general, Figure 8.4 indicates that the developed PROFFIT analysis procedure for CO_2 works quite well, due to reasonable results retrieved for Izaña. Although each measurement is analyzed using the same a priori profile, realistic variations between the retrieved profiles can be detected.

Comparison with in situ measurements

While in Section 6.1 TCCON X_{CO_2} total columns were compared to co-located ground-based in situ measurements, this section focuses on the validation of the retrieved vertical CO_2 profiles against the aforementioned measurements. For that purpose, CO_2 ground level concentrations are extracted from the profiles and compared to in situ values. First of all, profile retrieval results (ground values) have to be calibrated onto the in situ network's scale. The required calibration factor can be determined by the use of the correlation plot between FTIR CO_2 (ground level) and in situ CO_2, shown in Figure 8.5 (black). In this diagram, the former comparison between FTIR X_{CO_2} and in situ CO_2 is additionally shown in red, where the calibration factor of 0.989 for X_{CO_2} is already implemented. With a stability index of R=0.94, the plot indicates a good correlation between FTIR ground values and in situ measurements, where the slope of the regression line represents the demanded calibration factor. This factor (1.022) is different compared to the one determined for X_{CO_2} (0.989), where the discrepancy results from the use of different microwindows within the retrieval.
CO_2 ground values indicate a larger scatter compared to GFIT X_{CO_2} results which

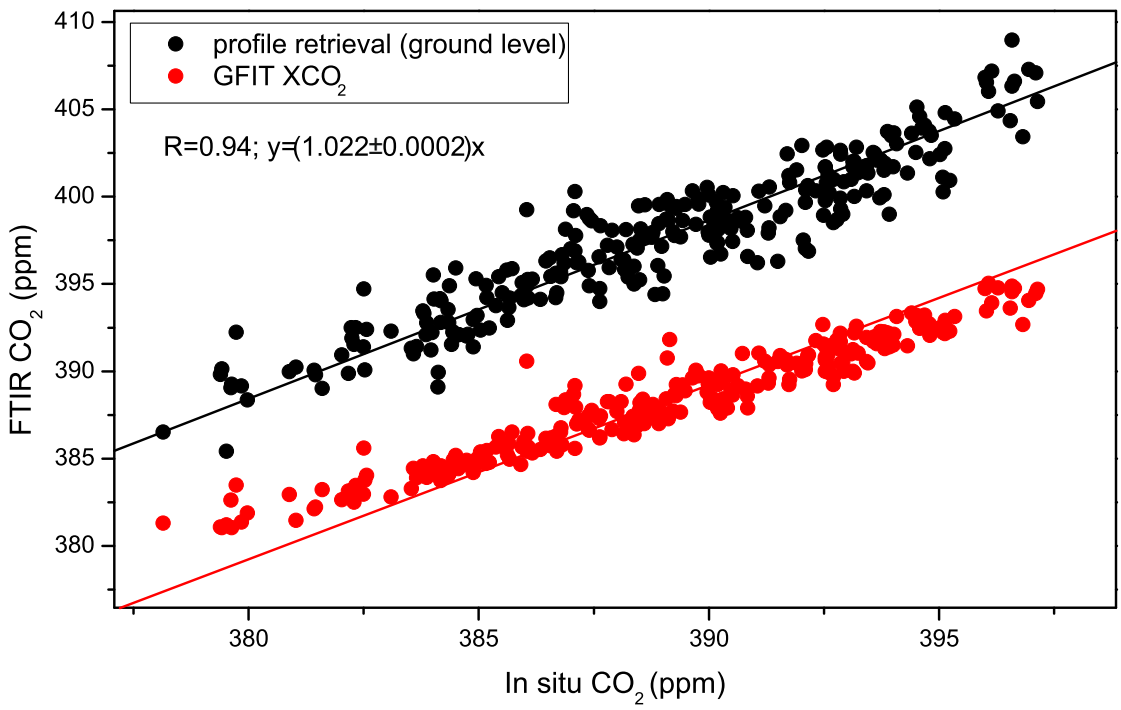

Figure 8.5: Correlation plot between FTIR CO_2 values (ground level) and in situ CO_2 results (black) for Izaña. Additionally the comparison between FTIR X_{CO_2} and in situ CO_2 is shown in red, where the calibration factor of 0.989 is already implemented.

may be due to strong CO_2 variations at the ground compared to more unaffected total columns results. Otherwise, the scatter can also be caused by an observed unrealistically high intraday variability of the retrieved profiles, which will be discussed in Section 8.4. In addition, FTIR ground values match the slope of the regression line much better than total column X_{CO_2} values, which show systematic differences.
The time series of daily mean CO_2 from GFIT (X_{CO_2}, red), profile retrieval ground values (black) and in situ measurements (grey) are illustrated in Figure 8.6, where calibration factors are already implemented in X_{CO_2} as well as in CO_2 (0.989 and 1.022 respectively). The three different time series are in good accordance with each other. Concerning the amplitude of the annual cycle, there is an excellent agreement between in situ values and CO_2 surface concentrations determined by the use of the PROFFIT profile retrieval. In contrast, the amplitude of the annual cycle of X_{CO_2} is smaller because it is less affected by local effects.
In summary the comparison between FTIR ground values and in situ measurements demonstrated that PROFFIT profile retrievals provide reasonable results.

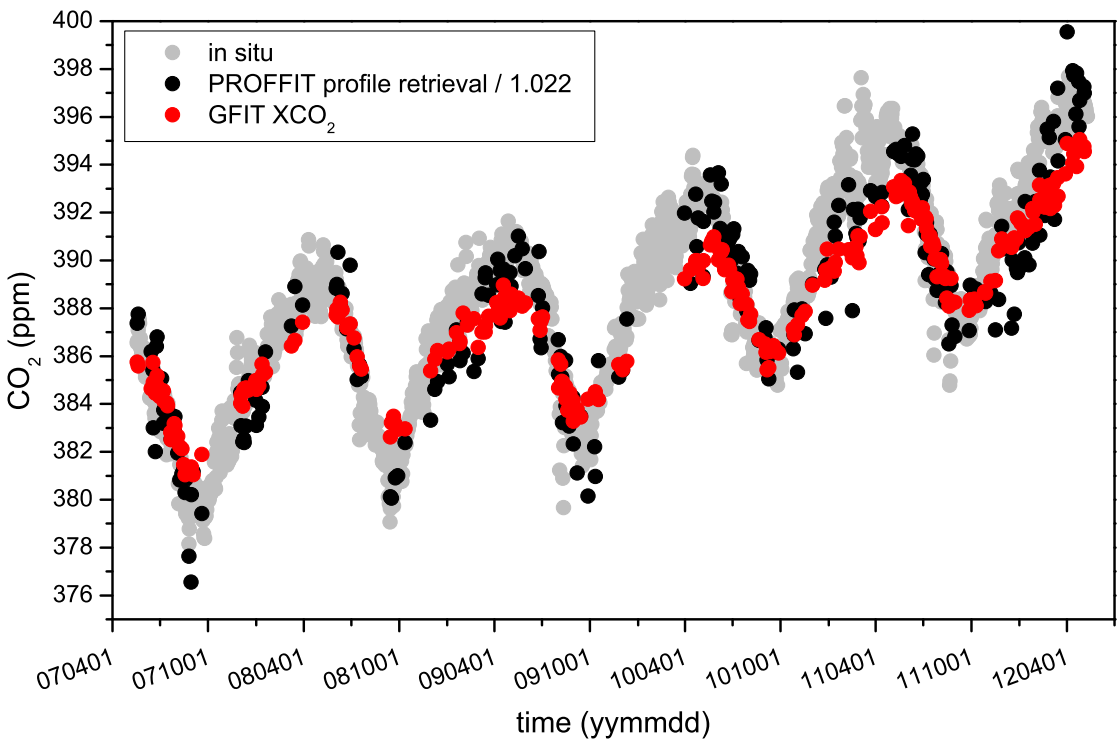

Figure 8.6: Izaña time series (2007–2012) of daily mean CO_2 from GFIT (X_{CO_2}, red), PROFFIT profile retrieval ground values (black) and in situ measurements (grey). Calibration factors for X_{CO_2} and FTIR CO_2 ground values are already implemented.

8.3 Lamont results

In this section vertical CO_2 profiles retrieved with the PROFFIT code are compared to simultaneous aircraft measurements. Due to the absence of high altitude aircraft measurements at the IMK-related TCCON sites Izaña and Karlsruhe, data from the TCCON site Lamont (Oklahoma, USA, 36.6°N, 97.5°W) are used for this comparison. The used aircraft measurements were observed during the aircraft campaigns HIPPO [Wofsy, 2011] and Learjet [Abshire et al., 2010]. The corresponding TCCON spectra were kindly provided by courtesy of D. Wunch and P. Wennberg.

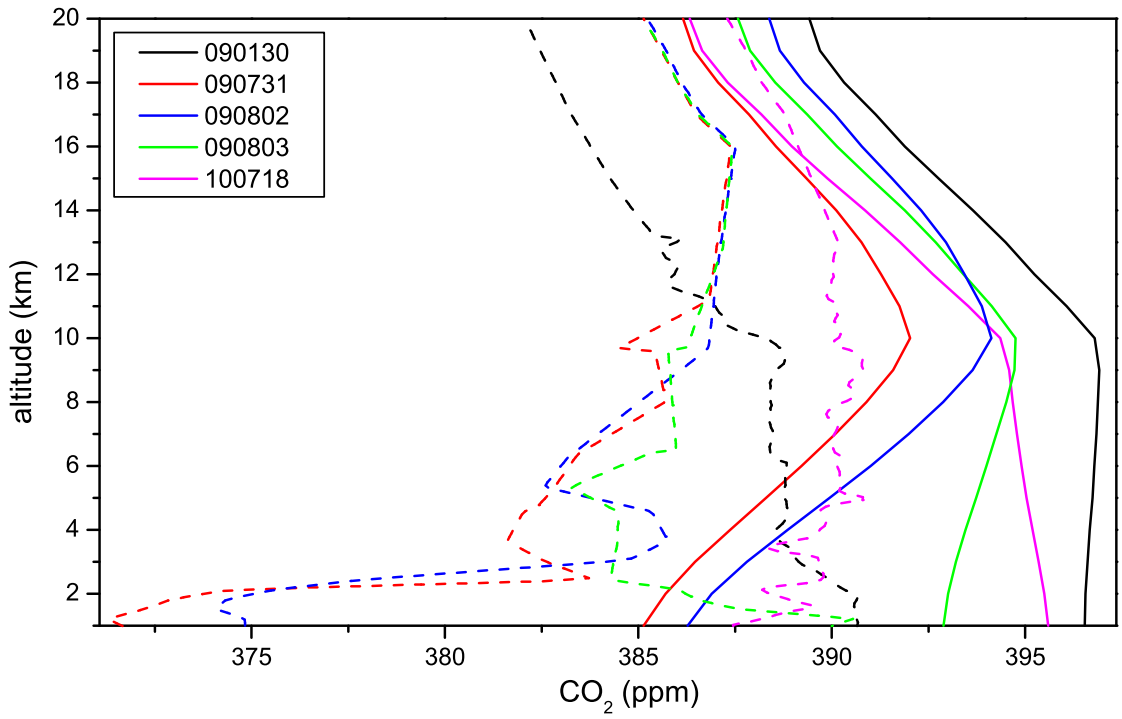

Figure 8.7: Vertical CO_2 profiles for altitudes of 1 to 20 km determined from TCCON spectra (solid lines) and retrieved from aircraft measurements (dashed lines) for five different days (different colors) at Lamont.

In Figure 8.7, vertical CO_2 profiles determined with PROFFIT (solid lines) and retrieved from aircraft measurements (dashed lines) at Lamont are shown for five different days (different colors) for altitudes between 1 and 20 km. The PROFFIT results are mean vertical profiles, retrieved from measurements recorded during the respective flight, where the number of simultaneous TCCON measurements for each flight/day are tabulated in Table 8.1.

A comparison between aircraft profiles and PROFFIT retrieval results indicates a shift

Flight date (yymmdd)	Flight time (hh:mm)	TCCON measurements
090130	13:43–14:47	44
090731	09:37–12:31	94
090802	10:05–12:57	93
090803	10:14–13:00	89
100718	11:15–15:27	3

Table 8.1: Number and local times of TCCON measurements which were taken during the corresponding flights.

of the latter ones to higher CO_2 values (5–10 ppm). This bias can be minimized by applying the calibration factor for the concerned microwindow, determined in the previous section. In addition the shape of profiles from PROFFIT and from aircraft measurements are very similar for each day, where only the profiles from the 3rd of August, 2009 (090803, green) differ for altitudes below 10 km.
In general, a comparison of vertical CO_2 profiles from FTIR measurements with in situ aircraft measurements (which are assumed to represent the true state) would only be reasonable if the sensitivity of profile retrieval results was ideal for each altitude. Since this is not the case, it is more proper to compare the results from profile retrievals with smoothed aircraft profiles, where the sensitivity of the retrieval is included:

$$\text{aircraft profile}_{\text{smoothed}} = \mathbf{AVK}\,(\text{aircraft profile} - \text{a priori profile}) + \text{a priori profile} \quad (8.1)$$

AVK is the averaging kernel, which is a measure for the sensitivity of a retrieved CO_2 value at a specific altitude to all altitude levels of the true CO_2 distribution.
In Figure 8.8 the determined CO_2 profiles from PROFFIT (solid lines) are compared to smoothed aircraft profiles (dashed lines), where the determined calibration factor of 1.022 (see Section 8.2) is already applied to the PROFFIT results. As before, different days are displayed with different colors.
The implementation of the microwindow specific calibration factor leads to a strong reduction of the bias between FTIR results and aircraft values. In addition, there is a very good agreement between profile shapes for most of the days, where also the profiles from 090803 (green) fit quite well. Major differences can only be detected for profiles from 100718 (magenta) concerning both the shape and the bias. By means of Table 8.1 these discrepancies can be attributed to the small number of only 3 measurements during this day compared to 44 for 090731 (red) and around 90 measurements for the other days.

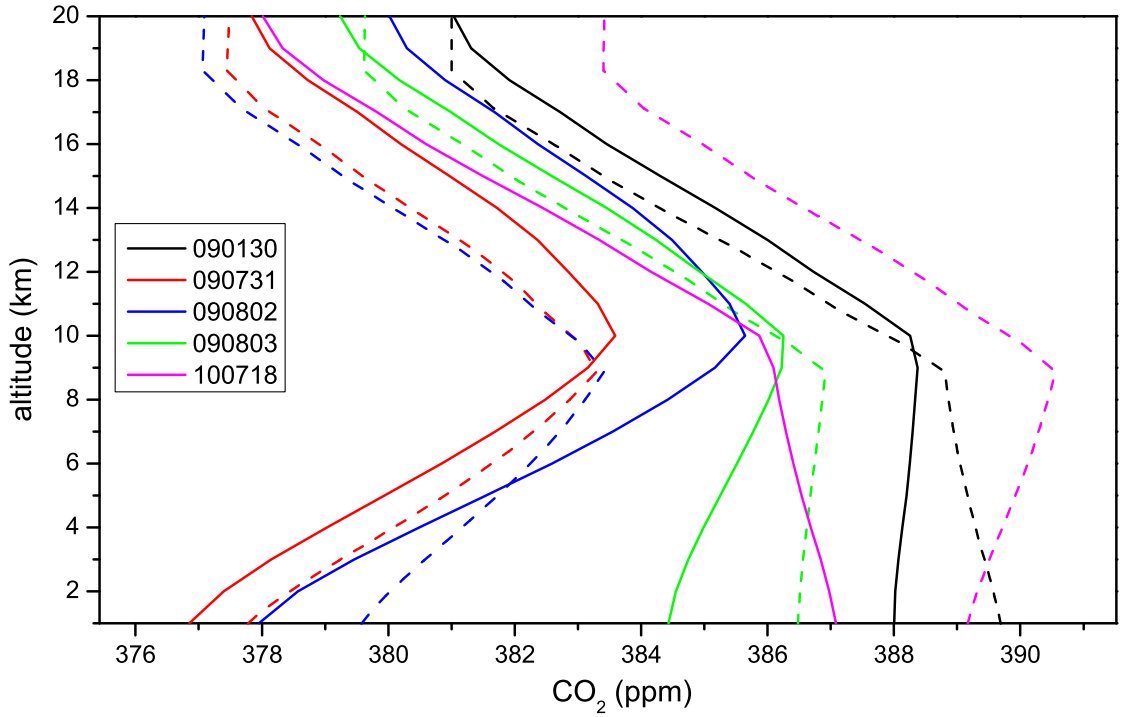

Figure 8.8: Comparison of vertical CO_2 profiles for altitudes of 1 to 20 km from TCCON spectra (solid lines) and smoothed aircraft profiles (dashed lines) for five different days (different colors) at Lamont, where the calibration factor of 1.022 is already implemented in TCCON measurements.

In general, the validation with vertical aircraft measurements demonstrated the possibility of determining vertical CO_2 profiles from TCCON spectra, which are of great interest for the modeling community.

8.4 Sensitivity studies

In the previous two sections the functionality of PROFFIT profile retrievals of CO_2 has been demonstrated. In addition to the good agreements of retrieval results with in situ ground measurements (Izaña) and with aircraft profiles (Lamont), an open issue has been found, which will be investigated within this section.
The complete set of TCCON CO_2 profiles (without implementing the calibration factor) for January 30th, 2009 (090130) measured at Lamont is shown in Figure 8.9, where the color gradient from red via green to blue represents the time of measurement (13:45–14:45, local time). For comparison the corresponding aircraft profile is illustrated in black. Regarding the shape of the determined profiles, a strong variabil-

ity can be detected, where the retrieved daily mean profile is in a good agreement with the aircraft measurement (see also Figure 8.7 or 8.8). This unrealistically large variability between measurements recorded within one hour can also be detected at other stations and has to be investigated further. Possible sources are correlations with the solar zenith angle, changing H_2O amounts, variations in ground pressure or changes in the temperature profile.

First of all, the sensitivity of the profile shape to changes of the SZA and variations of H_2O concentrations was tested by means of measurements from Izaña and Lamont. However, no correlation between these parameters and the profile shape was determined, while changes in the ILS, the ground pressure and the temperature profile lead to systematic effects. Therefore sensitivity studies for ILS, ground pressure and temperature profiles will be presented in the following sections.

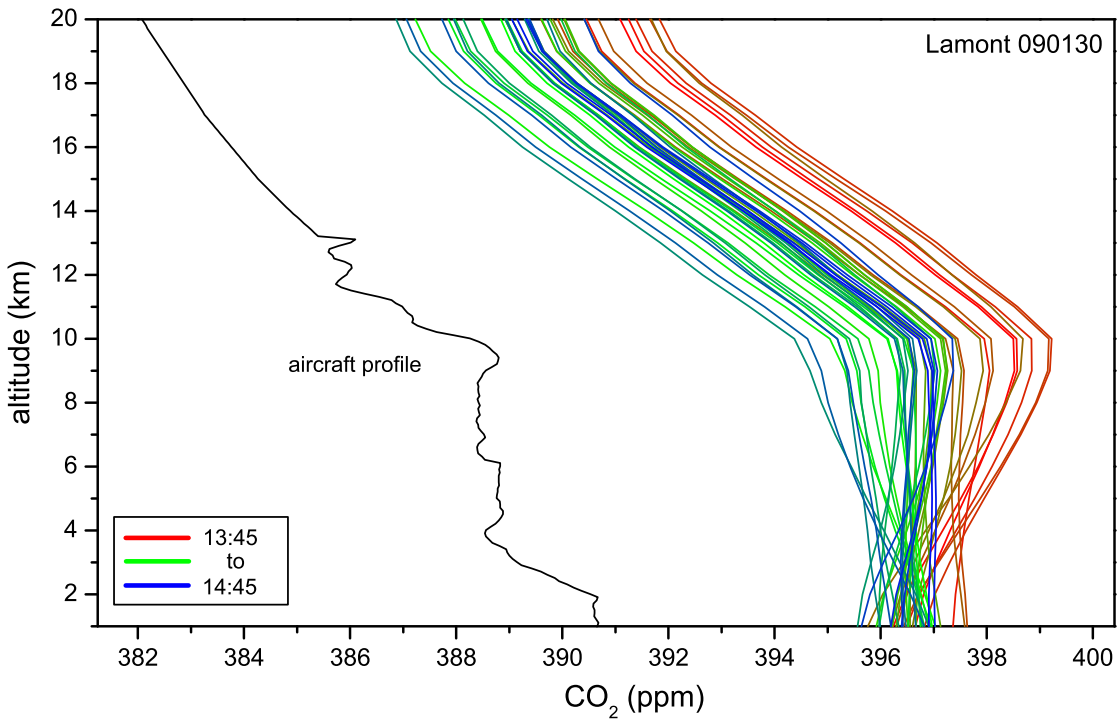

Figure 8.9: TCCON CO_2 profiles (without calibration factor) for January 30th, 2009 (090130) at Lamont, where the color gradient represents the time of measurement (red=13:45, blue=14:45). The corresponding aircraft measurement is illustrated in black.

8.4.1 Instrumental line shape

As described in Section 3.2, the ILS represents the imperfection of the instrument. In contrast to the ideal ILS, misalignments lead to an asymmetric behavior or smaller amplitudes of the real ILS, which have to be considered.
In this section, the impact of different ILS settings on the CO_2 profile shape will be studied. For this test, a measurement from 090130 at Lamont is analyzed with different ILS settings. The results are displayed in Figure 8.10, where the retrieved profiles for

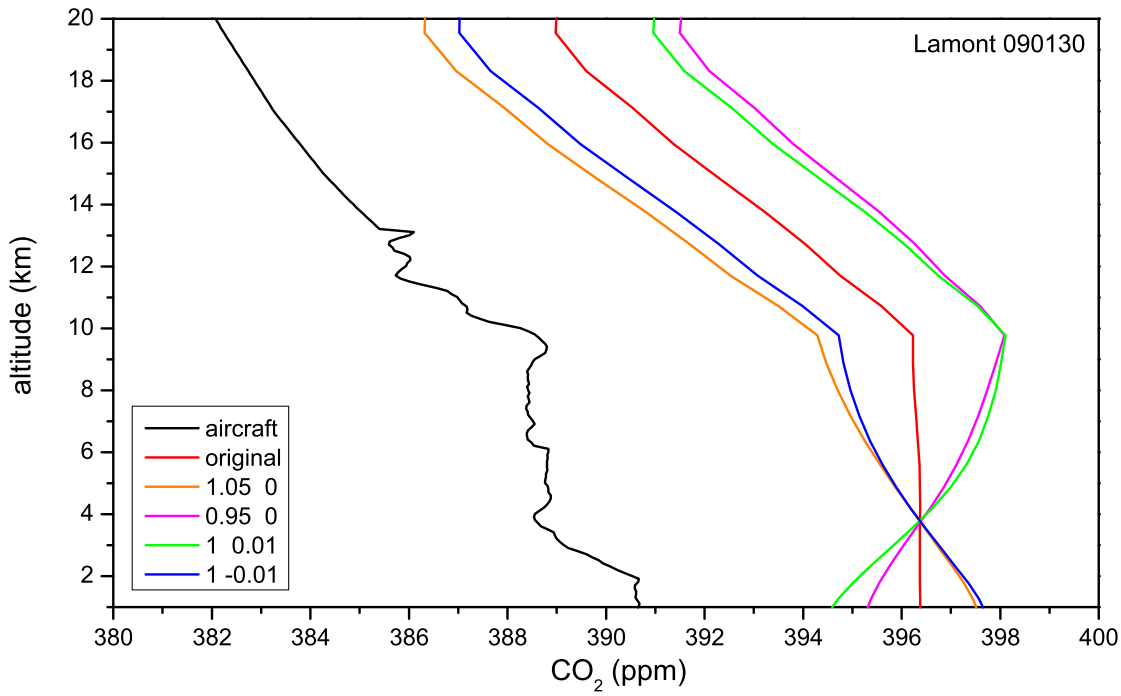

Figure 8.10: CO_2 profiles for 090130 at Lamont retrieved with different ILS settings. The red profile represents the standard setup. Whereas for orange and magenta colored profiles a 5% error in modulation efficiency was induced, the green and blue profiles were retrieved by using a 0.01 rad phase error. The black profile shows the corresponding aircraft measurement.

altitudes of 1 to 20 km with different ILS setups are shown in different colors and the corresponding aircraft measurement is additionally shown in black. The red profile was retrieved using the ideal ILS, which is the standard setup. Whereas for orange and magenta colored profiles a 5% error in modulation efficiency was induced, the green and blue profiles were retrieved by using a 0.01 rad phase error.
The differences between the resulting profiles indicate that changes in the ILS lead to non-negligible effects on the profile's shape. However, no ILS variability of this size

is expected during one day and even less during one hour, leading to the conclusion that changes in the ILS are not the reason for large intraday variabilities between CO_2 profiles. Nevertheless, this sensitivity study indicates that the ILS has to be considered within the retrieval in order to avoid errors in the resulting profiles.

8.4.2 Ground pressure

Another possible source for the detected large intraday variability of CO_2 profiles are variations of the ground pressure during one day, which are not considered within the retrieval (one pT profile per day). Therefore, the influence of ground pressure variations on the shape of the profile is analyzed by performing retrievals with different ground pressure values for a measurement from 090130 at Lamont.
In Figure 8.11 the results of this sensitivity study are shown for altitudes from 1 to 20 km, where the corresponding aircraft profile is again shown in black. While the red profile was determined by using the original ground pressure value (from NCEP), the blue and green profiles represent the results for a ground pressure change of ±1 hPa. Concerning the orange and magenta profiles, the ground pressure was modified by

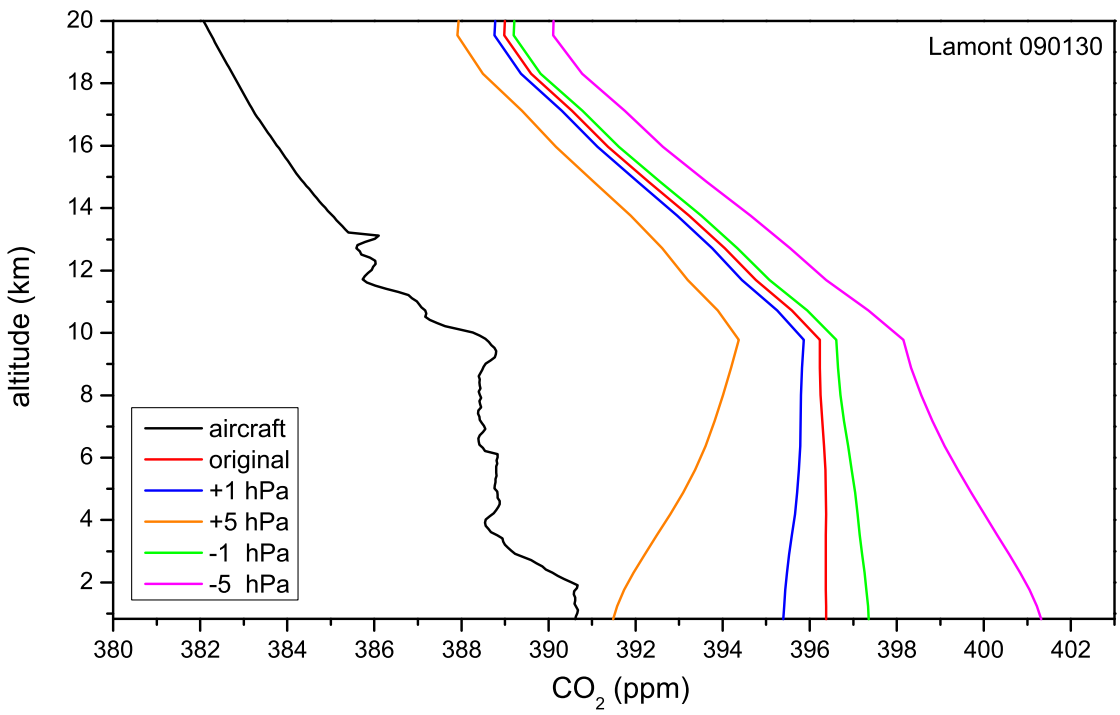

Figure 8.11: CO_2 profiles from 090130 at Lamont, analyzed with different deviations (±1 hPa, ±5 hPa.) from the original NCEP ground pressure value (red). The black profile illustrates the aircraft measurement.

±5 hPa.

Figure 8.11 indicates that ground pressure variations in the order of ±1 hPa only have small effects on the shape of the corresponding profiles, while larger changes of ±5 hPa have a strong impact, especially on lower levels. For each 1 hPa change at the ground, the CO_2 surface concentration changes by about 1 ppm. Since ground pressure variations in the order of ±5 hPa are quite possible, this effect could be a reason for the detected large intraday variability of vertical CO_2 profiles. However, it mainly leads to changes of CO_2 concentrations at the ground, which are not in accordance with the detected large variability at higher altitudes. Therefore additional reasons are likely and have to be investigated.

8.4.3 Temperature

Due to solar radiation which heats the Earth's surface, an intraday rise of the surface temperature is very common. Additionally, air masses at lower atmospheric levels are affected as well, leading to intraday variabilities in the temperature's profile.

In the standard profile retrieval, this effect is not considered (one pT profile per day), which may lead to errors in the resulting CO_2 profiles. Therefore the effect of intraday

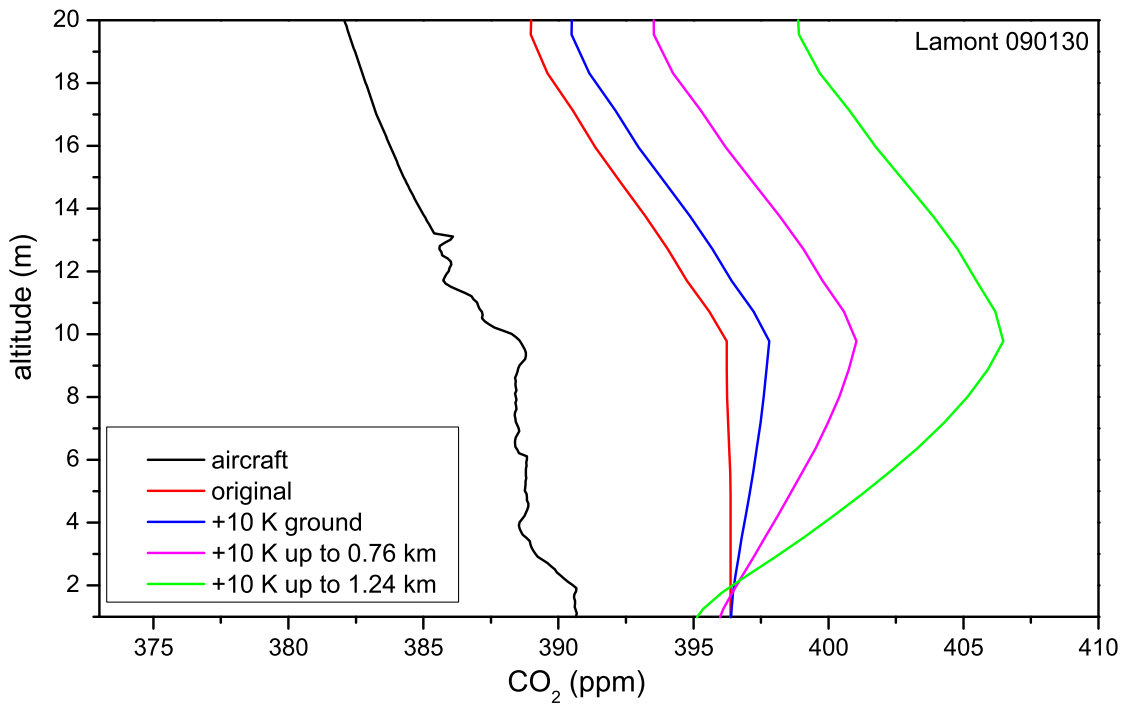

Figure 8.12: CO_2 profiles from 090130 at Lamont, analyzed with the use of different temperature profiles. The black profile illustrates the aircraft measurement.

temperature variabilities on CO_2 profiles will be investigated within this section. In this regard, the measurement from 090130 at Lamont is analyzed by using different temperature profiles within the retrievals. The results of this sensitivity study are shown in Figure 8.12. The corresponding aircraft profile is displayed in black, whereas the red profile represents the retrieval with the use of the original pT profile. Concerning the blue profile, the ground temperature was increased by 10 K, for the magenta profile ground and second level temperatures were increased by 10 K (up to 0.76 km) and for the green profile, 10 K was added to temperature values of the first three levels (up to 1.24 km).
While variations of the ground temperature (blue) lead to only small changes of the CO_2 profile, strong effects can be detected for temperature changes at higher altitudes (magenta, green). CO_2 concentrations at lower levels are less affected compared to higher levels, where a strong variability is clearly visible.
Due to the fact that temperature variations of this dimension are quite reasonable, this effect could be another reason for the detected intraday variability of the CO_2 profiles. In addition, it mainly influences the shape of the profile at higher altitudes, which is in accordance with the observed variability.

8.5 Conclusions

Regarding the common TCCON analysis, ground-based FTIR measurements in the NIR region are used to determine total column amounts of CO_2. However these results contain no information about the vertical CO_2 distribution, being of great interest. Therefore an analysis procedure for profile retrievals of CO_2 from TCCON spectra was developed and described in this chapter. In contrast to standard TCCON retrievals, the microwindow at 4338–4880 cm^{-1} was used, containing stronger line intensities. This led to larger column sensitivities at lower levels. In order to assure that profile variabilities are not caused by the implementation of different a priori profiles, the same a priori profile was used for every measurement.
The analysis of Izaña TCCON measurements by means of the PROFFIT profile retrieval led to reasonable results. A comparison between profile retrieval ground values and in situ ground measurements showed an excellent agreement, also with regard to the amplitude of the annual cycle. In addition an in situ calibration factor of 1.022 was determined for the aforementioned microwindow.
A more accurate validation for a larger number of levels was realized by comparing CO_2 aircraft profiles from Lamont with profile retrieval results from simultaneous TCCON

measurements. After smoothing the aircraft profiles by means of the averaging kernels and applying the in situ calibration factor of 1.022, a good agreement between profiles of aircraft measurements and profile retrievals was found. Large differences were detected for one day (100718) and have been assigned to the small number of TCCON measurements during the corresponding flight.

In addition to these very promising results, the issue of an unrealistically large intraday variability of CO_2 profiles was determined as well, where different sensitivity studies were performed to investigate the source of this effect. Intraday variations of the ground pressure and the temperature profile turned out to be the most probable sources, which haven't been considered in the retrieval process so far. Therefore the retrieval strategy has to be extended by using specific pT profiles for each measurement. While the ground pressure could be implemented from co-located measurements, the temperature profile might be determined from other gas retrievals (for example H_2O). Once the issue of large intraday variations of CO_2 profiles is solved, the determined vertical profiles can be used for a variety of applications. Due to their larger information content compared to total column results, these profiles are of great interest for the CO_2 modeling community in order to investigate the carbon cycle. In contrast to only sparsely available aircraft measurements which are currently used to consider the vertical transport within the models, the implementation of continuous profiles from TCCON measurements would be a great advantage. In addition, the use of the resulting profiles as a priori profiles within the common TCCON scaling retrievals will lead to an improved total column accuracy of X_{CO_2}.

Chapter 9

Summary and Outlook

In order to understand global climate change and to predict future effects, the investigation of the carbon cycle is strongly required. In this regard, accurate CO_2 total column abundances from ground-based FTIR measurements represent the major resource for the validation of satellites and are essential for the determination of CO_2 sources and sinks. Due to the fact that the desired total column accuracy of 0.1% [Olsen and Randerson, 2004] has not been achieved by former FTIR measurements [Wunch et al., 2011], a reduction of errors within the retrieval was necessary. The characterization and correction of error sources as well as an improvement of the retrieval method was presented in this work.

An error source which is of great importance especially for historic TCCON measurements, are sampling errors of the interferogram, leading to erroneous CO_2 total column amounts (0.1–0.5% [Messerschmidt et al., 2010] [Messerschmidt et al., 2011]). A procedure for the quantification and correction of these sampling errors was presented and published in Dohe et al. [2013]. With the use of this new method, laser sampling errors in the order of 0.2–0.5% were determined for Izaña, which are time and site dependent. After correcting the error at its source by resampling the interferogram, discrepancies have been reduced to 0.2%, where the residual difference was attributed to coincident changes in interferometer alignment. Since the desired TCCON total column accuracy of 0.1% cannot be achieved in the presence of sampling errors, the presented correction method has to be applied to defective measurements at all TCCON sites, which is scheduled for the end of 2013.

The calibration of TCCON measurements onto the in situ network's scale is important to provide a high quality data set for the validation of satellites. A comparison of TCCON measurements recorded at the IMK-related sites Izaña and Karlsruhe with co-located ground-based in situ measurements showed a good agreement, where the TCCON X_{CO_2} calibration factor of 0.989 [Messerschmidt et al., 2011] was verified for

both sites. For Karlsruhe, common periods with unusually large CO_2 concentrations were detected for in situ and FTIR measurements. Discrepancies in the amplitude of the annual cycle were attributed to the use of different measurement techniques (total column results compared to in situ measurements). Furthermore, a comparison between X_{CO_2} retrievals from different nearby European TCCON sites indicated a good agreement as well, where differences in the annual cycle were explained by the site's altitudes. In addition, events with unusually large CO_2 amounts were detected for all sites and have to be investigated further by use of backward trajectories.

In order to achieve the desired total column accuracy, a stepwise optimization of the PROFFIT CO_2 retrieval procedure was performed within this work. The implementation of the new line mixing feature and the improvement of the solar line list showed a reduction of fit residuals, while the application of collision induced absorption turned out to be dispensable if an extended baseline fit is applied. In addition, disturbing airmass dependent effects were eliminated by the modification of air-broadening widths. In summary, the accuracy in X_{CO_2} of about 0.05–0.12% for measurements at Karlsruhe was improved by up to 50%.

By means of an intercomparison between PROFFIT and GFIT X_{CO_2} results, the impact of several error sources within the retrieval was analyzed. Modifications of the PROFFIT retrieval setup like the improvement of the solar line list, the reparametrization of partition functions and the implementation of GFIT a priori profiles, GFIT pT profiles and the GFIT O_2 line list were carried out which led to a reduction of differences between X_{CO_2} values of the two codes. Including all changes, the bias between PROFFIT and GFIT was reduced from 0.42% to 0.03%, where the standard deviation also decreased from 0.520 ppm to 0.194 ppm, verifying the successful cross-validation of the two major codes for the analysis of ground-based FTIR measurements in the NIR region. It further indicates that PROFFIT represents an alternative for the analysis of NIR spectra within the TCCON.

In contrast to the good agreements between the two codes, the intercomparison revealed shortcomings of the operational TCCON retrieval. Airmass dependent effects were only detected for GFIT results and are probably due to the different implementation of the CIA feature and the lack of an extended baseline fit in GFIT. In order to ensure the high accuracy, this effect has to be corrected at its source, instead of applying an empirical post correction, as it is currently done for common TCCON retrievals.

In Chapter 8, a novel analysis procedure for the determination of vertical CO_2 profiles from TCCON spectra was presented. By the use of TCCON measurements from the

sites Izaña and Lamont, the functionality of the profile retrieval was demonstrated. On the basis of the comparison between profile retrieval ground values and ground-based in situ measurements recorded at Izaña, an in situ calibration factor of 1.022 was determined. After applying this factor a very good agreement between the resulting time series was found, also regarding the annual cycle's amplitude. The validation of retrieved CO_2 profiles with aircraft measurements from Lamont indicated an excellent agreement for all days with a sufficient number of measurements, where the above mentioned calibration factor was verified. In addition, an issue was detected, being the unrealistically variability of CO_2 during one day, which is presumably due to intra-day variations of the ground pressure and the temperature distribution. These effects haven't been considered in the retrieval process so far. By means of an expanded retrieval strategy with the use of specific pT profiles for each measurement, the problem might be solved. Temperature profiles can possibly be determined from other gas retrievals, while the ground-pressure can be taken from co-located measurements.
Due to their larger information content compared to total column results, the retrieved vertical CO_2 profiles are of great interest for the CO_2 modeling community, where up to now aircraft measurements are used to consider the vertical transport. The implementation of continuous profiles retrieved by means of TCCON measurements would be a great advantage. Concerning the common TCCON scaling retrievals, the determined CO_2 profiles can be used as a priori profiles leading to an improved total column accuracy.

References

Abrams, M. C., Toon, G. C., and Schindler, R. A.: Practical example of the correction of Fourier-transform spectra for detector nonlinearity, Applied Optics, 33, 6307–6314, doi:10.1364/AO.33.006307, URL http://ao.osa.org/abstract.cfm?URI=ao-33-27-6307, 1994.

Abshire, J. B., Riris, H., Allan, G. R., Weaver, C. J., Mao, J., Sun, X., Hasselbrack, W. E., Kawa, S. R., and Biraud, S.: Pulsed airborne lidar measurements of atmospheric CO_2 column absorption, Tellus B, 62, 770–783, doi:10.1111/j.1600-0889.2010.00502.x, URL http://dx.doi.org/10.1111/j.1600-0889.2010.00502.x, 2010.

Archer, D., Eby, M., Brovkin, V., Ridgwell, A., Cao, L., Mikolajewicz, U., Caldeira, K., Matsumoto, K., Munhoven, G., Montenegro, A., and Tokos, K.: Atmospheric Lifetime of Fossil Fuel Carbon Dioxide, Annual Review of Earth and Planetary Sciences, 37, 117–134, doi:10.1146/annurev.earth.031208.100206, URL http://www.annualreviews.org/doi/abs/10.1146/annurev.earth.031208.100206, 2009.

Atkins, P.: Physikalische Chemie, Wiley-VCH, Weinheim, 2001.

Beer, E.: Remote Sensing by Fourier Transform Spectroscopy, Wiley & Sons, New York, 1992.

Berner, R. A.: The carbon cycle and carbon dioxide over Phanerozoic time: the role of land plant, Philosophical Transactions of the Royal Society of London. Series B, Biological Sciences, 353, 75–82, doi:10.1098/rstb.1998.0192, URL http://rstb.royalsocietypublishing.org/content/353/1365/75.full.pdf+html, 1998.

Bovensmann, H., Buchwitz, M., Burrows, J. P., Reuter, M., Krings, T., Gerilowski, K., Schneising, O., Heymann, J., Tretner, A., and Erzinger, J.: A remote sensing technique for global monitoring of power plant CO_2 emissions from space

and related applications, Atmospheric Measurement Techniques, 3, 781–811, doi: 10.5194/amt-3-781-2010, URL http://www.atmos-meas-tech.net/3/781/2010/, 2010.

Chagas, J. C. S., Newnham, D. A., Smith, K. M., and Shine, K. P.: Impact of new measurements of oxygen collision-induced absorption on estimates of short-wave atmospheric absorption, Quarterly Journal of the Royal Meteorological Society, 128, 2377–2396, doi:10.1256/qj.01.159, URL http://dx.doi.org/10.1256/qj.01.159, 2002.

Chevallier, F., Deutscher, N. M., Conway, T. J., Ciais, P., Ciattaglia, L., Dohe, S., Fröhlich, M., Gomez-Pelaez, A. J., Griffith, D., Hase, F., Haszpra, L., Krummel, P., Kyrö, E., Labuschagne, C., Langenfelds, R., Machida, T., Maignan, F., Matsueda, H., Morino, I., Notholt, J., Ramonet, M., Sawa, Y., Schmidt, M., Sherlock, V., Steele, P., Strong, K., Sussmann, R., Wennberg, P., Wofsy, S., Worthy, D., Wunch, D., and Zimnoch, M.: Global CO_2 fluxes inferred from surface air-sample measurements and from TCCON retrievals of the CO_2 total column, Geophysical Research Letters, 38, L24 810, doi:10.1029/2011GL049899, URL http://dx.doi.org/10.1029/2011GL049899, 2011.

Cooley, J. W. and Tukey, J. W.: An Algorithm for the Machine Calculation of Complex Fourier Series, Mathematics of Computation, 19, 297–301, URL http://www.jstor.org/stable/2003354, 1965.

Demtröder, W.: Experimentalphysik 3: Atome, Moleküle und Festkörper, Springer, Berlin, Heidelberg, 2005.

Deutscher, N. M., Griffith, D. W. T., Bryant, G. W., Wennberg, P. O., Toon, G. C., Washenfelder, R. A., Keppel-Aleks, G., Wunch, D., Yavin, Y., Allen, N. T., Blavier, J.-F., Jiménez, R., Daube, B. C., Bright, A. V., Matross, D. M., Wofsy, S. C., and Park, S.: Total column CO_2 measurements at Darwin, Australia - site description and calibration against in situ aircraft profiles, Atmospheric Measurement Techniques, 3, 947–958, doi:10.5194/amt-3-947-2010, URL http://www.atmos-meas-tech.net/3/947/2010/, 2010.

Dlugokencky, E. J., Bruhwiler, L., White, J. W. C., Emmons, L. K., Novelli, P. C., Montzka, S. A., Masarie, K. A., Lang, P. M., Crotwell, A. M., Miller, J. B., and Gatti, L. V.: Observational constraints on recent increases in the atmospheric CH_4 burden,

Geophysical Research Letters, 36, L18 803, doi:10.1029/2009GL039780, URL http://dx.doi.org/10.1029/2009GL039780, 2009.

Dohe, S., Sherlock, V., Hase, F., Gisi, M., Robinson, J., Sepúlveda, E., Schneider, M., and Blumenstock, T.: A method to correct sampling ghosts in historic near-infrared Fourier transform spectrometer (FTS) measurements, Atmospheric Measurement Techniques, 6, 1981–1992, doi:10.5194/amt-6-1981-2013, URL http://www.atmos-meas-tech.net/6/1981/2013/, 2013.

Fabian, P.: Leben im Treibhaus: unser Klimasystem - und was wir daraus machen, Springer, Berlin, Heidelberg, 2002.

Flückiger, J., Monnin, E., Stauffer, B., Schwander, J., Stocker, T. F., Chappellaz, J., Raynaud, D., and Barnola, J.-M.: High-resolution Holocene N_2O ice core record and its relationship with CH_4 and CO_2, Global Biogeochemical Cycles, 16, 10–1–10–8, doi:10.1029/2001GB001417, URL http://dx.doi.org/10.1029/2001GB001417, 2002.

Gerlach, T.: Volcanic versus anthropogenic carbon dioxide, EOS, Transactions, American Geophysical Union, 92, 201–202, doi:10.1029/2011EO240001, URL http://dx.doi.org/10.1029/2011EO240001, 2011.

Gisi, M.: Setup of precise camera based solar tracker systems and greenhouse gas measurements using a modified portable spectrometer, Ph.D. thesis, Karlsruher Institut für Technologie, 2012.

Gisi, M., Hase, F., Dohe, S., and Blumenstock, T.: Camtracker: a new camera controlled high precision solar tracker system for FTIR-spectrometers, Atmospheric Measurement Techniques, 4, 47–54, doi:10.5194/amt-4-47-2011, URL http://www.atmos-meas-tech.net/4/47/2011/, 2011.

Gomez-Pelaez, A. J., Ramos, R., and Cuevas, E., eds.: 25 years of contiuous CO_2 and CH_4 measurements at Izaña Global GAW mountain station: annual cycles and interannual trends, ACP Symposium 2010.

Gordon, I. E., Kassi, S., Campargue, A., and Toon, G. C.: First identification of the electric quadrupole transitions of oxygen in solar and laboratory spectra, Journal of Quantitative Spectroscopy and Radiative Transfer, 111, 1174–1183, doi:http://dx.doi.org/10.1016/j.jqsrt.2010.01.008, URL http://www.sciencedirect.com/science/article/pii/S0022407310000191, 2010.

Griffiths, P. and de Haseth, J. A.: Fourier Transform Infrared Spectrometry, Chemical Analysis: A Series of Monographs on Analytical Chemistry and Its Applications, Wiley&Sons, New York, 2007.

Guelachvili, G.: Spectrometric Techniques, chap. Distortions in Fourier spectra and diagnosis, pp. 1–61, Academic Press, 1981.

Häckel, H.: Meteorologie, Ulmer, Stuttgart, 1999.

Hannigan, J. W.: NDACC IRWG: Evolution of Ground-Based Global Trace Gas Infrared Remote Sensing, in: Imaging and Applied Optics, Optical Society of America, doi:10.1364/FTS.2011.FMC1, URL `http://www.opticsinfobase.org/abstract.cfm?URI=FTS-2011-FMC1`, 2011.

Hartmann, J.-M., Tran, H., and Toon, G. C.: Influence of line mixing on the retrievals of atmospheric CO_2 from spectra in the 1.6 and 2.1 μm regions, Atmospheric Chemistry and Physics, 9, 7303–7312, doi:10.5194/acp-9-7303-2009, URL `http://www.atmos-chem-phys.net/9/7303/2009/`, 2009.

Hase, F.: Inversion von Spurengasprofilen aus hochaufgelösten bodengebundenen FTIR-Messungen in Absorption, Ph.D. thesis, Forschungszentrum Karlsruhe, 2000.

Hase, F.: Improved instrumental line shape monitoring for the ground-based, high-resolution FTIR spectrometers of the Network for the Detection of Atmospheric Composition Change, Atmospheric Measurement Techniques, 5, 603–610, doi:10.5194/amt-5-603-2012, URL `http://www.atmos-meas-tech.net/5/603/2012/`, 2012a.

Hase, F.: PROFFIT Update, TCCON Meeting Wengen, 2012b.

Hase, F., Blumenstock, T., and Paton-Walsh, C.: Analysis of the Instrumental Line Shape of High-Resolution Fourier Transform IR Spectrometers with Gas Cell Measurements and New Retrieval Software, Applied Optics, 38, 3417–3422, doi:10.1364/AO.38.003417, URL `http://ao.osa.org/abstract.cfm?URI=ao-38-15-3417`, 1999.

Hase, F., Hannigan, J., Coffey, M., Goldman, A., Höpfner, M., Jones, N., Rinsland, C., and Wood, S.: Intercomparison of retrieval codes used for the analysis of high-resolution, ground-based FTIR measurements, Journal of Quantitative Spectroscopy and Radiative Transfer, 87, 25–52, doi:http://dx.doi.org/10.1016/j.

jqsrt.2003.12.008, URL http://www.sciencedirect.com/science/article/pii/S0022407303003765, 2004.

Hase, F., Drouin, B. J., Roehl, C. M., Toon, G. C., Wennberg, P. O., Wunch, D., Blumenstock, T., Desmet, F., Feist, D. G., Heikkinen, P., De Mazière, M., Rettinger, M., Robinson, J., Schneider, M., Sherlock, V., Sussmann, R., Té, Y., Warneke, T., and Weinzierl, C.: Calibration of sealed HCl cells used for TCCON instrumental line shape monitoring, Atmospheric Measurement Techniques Discussions, 6, 7185–7215, doi:10.5194/amtd-6-7185-2013, URL http://www.atmos-meas-tech-discuss.net/6/7185/2013/, 2013.

IPCC: Climate Change 2001: Synthesis Report. A Contribution of Working Groups I, II and III to the Third Assessment Report of the Intergovernmental Panel on Climate Change, Cambridge University Press, Cambridge and , New York, 2001.

IPCC: Climate Change 2007: Synthesis Report. A Contribution of Working Groups I, II and III to the Fourth Assessment Report of the Intergovernmental Panel on Climate Change, IPCC, Geneva, 2007.

Keeling, C. D., Piper, S. C., Bacastow, R. B., Wahlen, M., Whorf, T. P., Heimann, M., and Meijer, H. A.: Atmospheric CO_2 and $^{13}CO_2$ Exchange with the Terrestrial Biosphere and Oceans from 1978 to 2000: Observations and Carbon Cycle Implications, in: A History of Atmospheric CO_2 and Its Effects on Plants, Animals, and Ecosystems, edited by Baldwin, I. T., Caldwell, M. M., Heldmaier, G., Jackson, R. B., Lange, O. L., Mooney, H. A., Schulze, E.-D., Sommer, U., Ehleringer, J. R., Dearing, D. M., and Cerling, T. E., vol. 177 of *Ecological Studies*, pp. 83–113, Springer, doi:10.1007/0-387-27048-5_5, URL http://dx.doi.org/10.1007/0-387-27048-5_5, 2005.

Keppel-Aleks, G., Toon, G. C., Wennberg, P. O., and Deutscher, N. M.: Reducing the impact of source brightness fluctuations on spectra obtained by Fourier-transform spectrometry, Applied Optics, 46, 4774–4779, doi:10.1364/AO.46.004774, URL http://ao.osa.org/abstract.cfm?URI=ao-46-21-4774, 2007.

Keppel-Aleks, G., Wennberg, P. O., and Schneider, T.: Sources of variations in total column carbon dioxide, Atmospheric Chemistry and Physics, 11, 3581–3593, doi:10.5194/acp-11-3581-2011, URL http://www.atmos-chem-phys.net/11/3581/2011/, 2011.

Kramer, I.: Zeitreihen troposphärischer Spurengase abgeleitet aus bodengebundenen FTIR-Messungen, Ph.D. thesis, Forschungszentrum Karlsruhe, 2007.

Kraus, H.: Die Atmosphäre Der Erde: Eine Einführung in Die Meteorologie, Springer, Berlin, Heidelberg, 2006.

Le Quéré, C., Andres, R. J., Boden, T., Conway, T., Houghton, R. A., House, J. I., Marland, G., Peters, G. P., van der Werf, G., Ahlström, A., Andrew, R. M., Bopp, L., Canadell, J. G., Ciais, P., Doney, S. C., Enright, C., Friedlingstein, P., Huntingford, C., Jain, A. K., Jourdain, C., Kato, E., Keeling, R. F., Klein Goldewijk, K., Levis, S., Levy, P., Lomas, M., Poulter, B., Raupach, M. R., Schwinger, J., Sitch, S., Stocker, B. D., Viovy, N., Zaehle, S., and Zeng, N.: The global carbon budget 1959–2011, Earth System Science Data Discussions, 5, 1107–1157, doi:10.5194/essdd-5-1107-2012, URL `http://www.earth-syst-sci-data-discuss.net/5/1107/2012/`, 2012.

Messerschmidt, J., Macatangay, R., Notholt, J., Petri, C., Warneke, T., and Weinzierl, C.: Side by side measurements of CO_2 by ground-based Fourier transform spectrometry (FTS), Tellus B, 62, 749–758, doi:10.1111/j.1600-0889.2010.00491.x, URL `http://dx.doi.org/10.1111/j.1600-0889.2010.00491.x`, 2010.

Messerschmidt, J., Geibel, M. C., Blumenstock, T., Chen, H., Deutscher, N. M., Engel, A., Feist, D. G., Gerbig, C., Gisi, M., Hase, F., Katrynski, K., Kolle, O., Lavrič, J. V., Notholt, J., Palm, M., Ramonet, M., Rettinger, M., Schmidt, M., Sussmann, R., Toon, G. C., Truong, F., Warneke, T., Wennberg, P. O., Wunch, D., and Xueref-Remy, I.: Calibration of TCCON column-averaged CO_2: the first aircraft campaign over European TCCON sites, Atmospheric Chemistry and Physics, 11, 10 765–10 777, doi:10.5194/acp-11-10765-2011, URL `http://www.atmos-chem-phys.net/11/10765/2011/`, 2011.

Miller, C. E., Crisp, D., DeCola, P. L., Olsen, S. C., Randerson, J. T., Michalak, A. M., Alkhaled, A., Rayner, P., Jacob, D. J., Suntharalingam, P., Jones, D. B. A., Denning, A. S., Nicholls, M. E., Doney, S. C., Pawson, S., Boesch, H., Connor, B. J., Fung, I. Y., O'Brien, D., Salawitch, R. J., Sander, S. P., Sen, B., Tans, P., Toon, G. C., Wennberg, P. O., Wofsy, S. C., Yung, Y. L., and Law, R. M.: Precision requirements for space-based data, Journal of Geophysical Research: Atmospheres, 112, D10 314, doi:10.1029/2006JD007659, URL `http://dx.doi.org/10.1029/2006JD007659`, 2007.

Morino, I., Uchino, O., Inoue, M., Yoshida, Y., Yokota, T., Wennberg, P. O., Toon, G. C., Wunch, D., Roehl, C. M., Notholt, J., Warneke, T., Messerschmidt, J., Griffith, D. W. T., Deutscher, N. M., Sherlock, V., Connor, B., Robinson, J., Sussmann, R., and Rettinger, M.: Preliminary validation of column-averaged volume mixing ratios of carbon dioxide and methane retrieved from GOSAT short-wavelength infrared spectra, Atmospheric Measurement Techniques, 4, 1061–1076, doi:10.5194/amt-4-1061-2011, URL `http://www.atmos-meas-tech.net/4/1061/2011/`, 2011.

Newman, S. M., Lane, I. C., Orr-Ewing, A. J., Newnham, D. A., and Ballard, J.: Integrated absorption intensity and Einstein coefficients for the O_2 $a^1\Delta_g$–$X^3\Sigma_g^-$(0,0) transition: A comparison of cavity ringdown and high resolution Fourier transform spectroscopy with a long-path absorption cell, The Journal of Chemical Physics, 110, 10 749–10 757, doi:10.1063/1.479018, URL `http://link.aip.org/link/?JCP/110/10749/1`, 1999.

Olsen, S. C. and Randerson, J. T.: Differences between surface and column atmospheric CO_2 and implications for carbon cycle research, Journal of Geophysical Research: Atmospheres, 109, D023 012, doi:10.1029/2003JD003968, URL `http://dx.doi.org/10.1029/2003JD003968`, 2004.

Oshchepkov, S., Bril, A., Yokota, T., Yoshida, Y., Blumenstock, T., Deutscher, N. M., Dohe, S., Macatangay, R., Morino, I., Notholt, J., Rettinger, M., Petri, C., Schneider, M., Sussmann, R., Uchino, O., Velazco, V., Wunch, D., and Belikov, D.: Simultaneous retrieval of atmospheric CO_2 and light path modification from space-based spectroscopic observations of greenhouse gases: methodology and application to GOSAT measurements over TCCON sites, Applied Optics, 52, 1339–1350, doi:10.1364/AO.52.001339, URL `http://ao.osa.org/abstract.cfm?URI=ao-52-6-1339`, 2013.

Phillips, D. L.: A Technique for the Numerical Solution of Certain Integral Equations of the First Kind, Journal of the ACM, 9, 84–97, doi:10.1145/321105.321114, URL `http://doi.acm.org/10.1145/321105.321114`, 1962.

Riebeek, H.: The Carbon Cycle, URL `http://earthobservatory.nasa.gov/Features/CarbonCycle/`, 2011.

Rinsland, C. P., Jones, N. B., Connor, B. J., Logan, J. A., Pougatchev, N. S., Goldman, A., Murcray, F. J., Stephen, T. M., Pine, A. S., Zander, R., Mahieu, E., and

Demoulin, P.: Northern and southern hemisphere ground-based infrared spectroscopic measurements of tropospheric carbon monoxide and ethane, Journal of Geophysical Research: Atmospheres, 103, 28 197–28 217, doi:10.1029/98JD02515, URL http://dx.doi.org/10.1029/98JD02515, 1998.

Rodgers, C. D.: Retrieval of atmospheric temperature and composition from remote measurements of thermal radiation, Reviews of Geophysics, 14, 609–624, doi:10.1029/RG014i004p00609, URL http://dx.doi.org/10.1029/RG014i004p00609, 1976.

Rodgers, C. D.: Inverse Methods for Atmospheric Sounding: Theory and Practice, World Scientific Publishing Co, Singapur, 2000.

Rothman, L. S., Gordon, I. E., Barbe, A., Benner, D. C., Bernath, P. F., Birk, M., Boudon, V., Brown, L. R., Campargue, A., Champion, J.-P., Chance, K., Coudert, L. H., Dana, V., Devi, V. M., Fally, S., Flaud, J.-M., Gamache, R. R., Goldman, A., Jacquemart, D., Kleiner, I., Lacome, N., Lafferty, W. J., Mandin, J.-Y., Massie, S. T., Mikhailenko, S. N., Miller, C. E., Moazzen-Ahmadi, N., Naumenko, O. V., Nikitin, A. V., Orphal, J., Perevalov, V. I., Perrin, A., Predoi-Cross, A., Rinsland, C. P., Rotger, M., Šimečová, M., Smith, M. A. H., Sung, K., Tashkun, S. A., Tennyson, J., Toth, R. A., Vandaele, A. C., and Vander Auwera, J.: The HITRAN 2008 molecular spectroscopic database, Journal of Quantitative Spectroscopy and Radiative Transfer, 110, 533–572, doi:http://dx.doi.org/10.1016/j.jqsrt.2009.02.013, URL http://www.sciencedirect.com/science/article/pii/S0022407309000727, 2009.

Schmidt, G. A., Ruedy, R. A., Miller, R. L., and Lacis, A. A.: Attribution of the present-day total greenhouse effect, Journal of Geophysical Research: Atmospheres, 115, D20 106, doi:10.1029/2010JD014287, URL http://dx.doi.org/10.1029/2010JD014287, 2010.

Seifritz, W.: Der Treibhauseffekt. Technische Maßnahmen zur CO_2-Entsorgung, Hanser, München, 1991.

Sepúlveda, E., Schneider, M., Hase, F., García, O. E., Gomez-Pelaez, A., Dohe, S., Blumenstock, T., and Guerra, J. C.: Long-term validation of tropospheric column-averaged CH_4 mole fractions obtained by mid-infrared ground-based FTIR spectrometry, Atmospheric Measurement Techniques, 5, 1425–1441, doi:10.5194/amt-5-1425-2012, URL http://www.atmos-meas-tech.net/5/1425/2012/, 2012.

Smith, K. M. and Newnham, D. A.: Near-infrared absorption cross sections and integrated absorption intensities of molecular oxygen (O_2, O_2-O_2, and O_2-N_2), Journal of Geophysical Research: Atmospheres, 105, 7383–7396, doi:10.1029/1999JD901171, URL `http://dx.doi.org/10.1029/1999JD901171`, 2000.

Spiering, F. R. and van der Zande, W. J.: Collision induced absorption in the $a^1\Delta$(v=2)$\leftarrow X^3\Sigma_g^-$(v=0) band of molecular oxygen, Physical Chemistry Chemical Physics, 14, 9923–9928, doi:10.1039/C2CP40961E, URL `http://dx.doi.org/10.1039/C2CP40961E`, 2012.

Sussmann, R., Rettinger, M., and Keens, A.: Personal communication, 2011.

Tikhonov, A. N.: On the solution of ill-posed problems and the method of regularization, Doklady Akademii Nauk SSSR, 151, 501–504, 1963.

Tipler, P. A.: Physik, Spektrum, Berlin, Heidelberg, 1994.

Toon, G. C., Blavier, J.-F., Washenfelder, R., Wunch, D., Keppel-Aleks, G., Wennberg, P. O., Connor, B., Sherlock, V., Griffith, D., Deutscher, N. M., and Notholt, J.: Total Column Carbon Observing Network (TCCON), in: Advances in Imaging, Optical Society of America, doi:10.1364/FTS.2009.JMA3, URL `http://www.opticsinfobase.org/abstract.cfm?URI=FTS-2009-JMA3`, 2009.

Toth, R. A., Brown, L. R., Miller, C. E., Devi, M., and Benner, D. C.: Spectroscopic database of CO_2 line parameters: 4300–7000 cm^{-1}, Journal of Quantitative Spectroscopy and Radiative Transfer, 109, 906–921, doi:http://dx.doi.org/10.1016/j.jqsrt.2007.12.004, URL `http://www.sciencedirect.com/science/article/pii/S0022407307003512`, 2008.

Velders, G. J. M., Ravishankara, A. R., Miller, M. K., Molina, M. J., Alcamo, J., Daniel, J. S., Fahey, D. W., Montzka, S. A., and Reimann, S.: Preserving Montreal Protocol Climate Benefits by Limiting HFCs, Science, 335, 922–923, doi:10.1126/science.1216414, URL `http://www.sciencemag.org/content/335/6071/922.short`, 2012.

von Clarmann, T.: Zur Fernerkundung der Erdatmosphäre mittels Infrarotspektrometrie: Rekonstruktionstheorie und Anwendung, Forschungszentrum Karlsruhe, Habilitation, 2003.

Washenfelder, R. A., Toon, G. C., Blavier, J.-F., Yang, Z., Allen, N. T., Wennberg, P. O., Vay, S. A., Matross, D. M., and Daube, B. C.: Carbon dioxide column abundances at the Wisconsin Tall Tower site, Journal of Geophysical Research: Atmospheres, 111, D22 305, doi:10.1029/2006JD007154, URL `http://dx.doi.org/10.1029/2006JD007154`, 2006.

Wofsy, S. C.: HIAPER Pole-to-Pole Observations (HIPPO): fine-grained, global-scale measurements of climatically important atmospheric gases and aerosols, Philosophical Transactions of the Royal Society A: Mathematical, Physical and Engineering Sciences, 369, 2073–2086, doi:10.1098/rsta.2010.0313, URL `http://rsta.royalsocietypublishing.org/content/369/1943/2073.abstract`, 2011.

Wunch, D., Toon, G. C., Wennberg, P. O., Wofsy, S. C., Stephens, B. B., Fischer, M. L., Uchino, O., Abshire, J. B., Bernath, P., Biraud, S. C., Blavier, J.-F. L., Boone, C., Bowman, K. P., Browell, E. V., Campos, T., Connor, B. J., Daube, B. C., Deutscher, N. M., Diao, M., Elkins, J. W., Gerbig, C., Gottlieb, E., Griffith, D. W. T., Hurst, D. F., Jiménez, R., Keppel-Aleks, G., Kort, E. A., Macatangay, R., Machida, T., Matsueda, H., Moore, F., Morino, I., Park, S., Robinson, J., Roehl, C. M., Sawa, Y., Sherlock, V., Sweeney, C., Tanaka, T., and Zondlo, M. A.: Calibration of the Total Carbon Column Observing Network using aircraft profile data, Atmospheric Measurement Techniques, 3, 1351–1362, doi:10.5194/amt-3-1351-2010, URL `http://www.atmos-meas-tech.net/3/1351/2010/`, 2010.

Wunch, D., Toon, G. C., Blavier, J.-F. L., Washenfelder, R. A., Notholt, J., Connor, B. J., Griffith, D. W. T., Sherlock, V., and Wennberg, P. O.: The Total Carbon Column Observing Network, Philosophical Transactions of the Royal Society A: Mathematical, Physical and Engineering Sciences, 369, 2087–2112, doi:10.1098/rsta.2010.0240, URL `http://rsta.royalsocietypublishing.org/content/369/1943/2087.abstract`, 2011.

Yang, Z., Wennberg, P. O., Cageao, R. P., Pongetti, T. J., Toon, G. C., and Sander, S. P.: Ground-based photon path measurements from solar absorption spectra of the O_2 A-band, Journal of Quantitative Spectroscopy and Radiative Transfer, 90, 309–321, doi:http://dx.doi.org/10.1016/j.jqsrt.2004.03.020, URL `http://www.sciencedirect.com/science/article/pii/S002240730400072X`, 2005.

List of Figures

1.1 The atmosphere can be divided into four parts (troposphere, stratosphere, mesosphere and thermosphere) where the structure is specified through the vertical temperature profile depending on the amount of absorbed radiation (based on Häckel [1999]). 4

1.2 A schematic overview of the carbon cycle of the 1990's with main annual fluxes in GtC/year. Pre-industrial fluxes are displayed in black arrows whereas anthropogenic fluxes are shown as red arrows. (Taken from IPCC [2007]) 6

1.3 A schematic illustration of the annual cycle of CO_2 for the northern hemisphere (NH, blue) and the southern hemisphere (SH, red) with increasing CO_2 values in winter and a maximum in spring. Plants begin to grow, causing a CO_2 decrease with a minimum in autumn, where the cycle starts again. Atmospheric CO_2 fluctuations are more pronounced in the northern hemisphere. 8

1.4 Time series of atmospheric CO_2 measurements at Mauna Loa (Hawaii). Since the start of recording in 1958 until 2010, the CO_2 concentration increased by about 75 ppm. (Taken from NOAA/ESRL[3]) 9

1.5 The natural greenhouse effect, where infrared radiation from the Earth's surface is absorbed by GHGs, leading to an increase in surface and low tropospheric temperatures. (Taken from IPCC [2007]) 12

1.6 A spectrum of the solar radiation emitted from the Earth (blue) compared to the one which can be detected at top of the atmosphere (red). The reduction of outgoing radiation is due to the absorption of GHGs in the corresponding region. 12

2.1 Comparison between harmonic and anharmonic oscillation (Morse potential), where the latter one is wider for higher energy levels with smaller distances between vibrational states. (Taken from Wikipedia) . 19

2.2 Possible transitions between v and $v+1$ causing P-, R- and Q-branch. Transitions with $\Delta J = -1$ build the P-branch, whereas $\Delta J = +1$ transitions build the R-branch. The Q-branch in between is due to pure vibrational transitions and only allowed for molecules with angular momentums in parallel to their symmetry axis. 21

2.3 Transmittance spectrum of HBr recorded with a Bruker 120HR at Kiruna (Sweden), where P- and R-branches are clearly visible. 22

2.4 IR absorption spectrum of CO_2 recorded with the Bruker 125HR at Karlsruhe. Spectral lines are due to combinations of different vibrational modes: $2\tilde{\nu}_1+2\tilde{\nu}_2+\tilde{\nu}_3$ (see Figure 2.5). 23

2.5 The four vibrational modes of a linear triatomic molecule like CO_2, where the symmetric stretching vibration (a) is IR inactive. The corresponding spectral lines are $\tilde{\nu}_1$=1388 cm^{-1} (a, symmetric stretching), $\tilde{\nu}_2$=667 cm^{-1} (b, bending) and $\tilde{\nu}_3$=2349 cm^{-1} (c, asymmetric stretching)[Atkins, 2001]. 23

3.1 Schematic illustration of the FTIR spectrometer (top view) used within this work. (Taken from Gisi et al. [2011]) 28

3.2 An Overview of different apodization functions: a) boxcar b) trapezoidal c) triangular and d) triangular^2. (Taken from Griffiths and de Haseth [2007]) 32

3.3 Map of worldwide NDACC stations, where IRWG sites are shown as green stars (red: all sites; image was taken from the NDACC web page. 33

3.4 Map of worldwide TCCON stations. Operational sites are shown with red dots whereas blue squares belong to future sites. (Taken from the TCCON web page) 34

3.5 Pictures of the spectrometer (Karlsruhe) and the measurement container (Izaña). 36

4.1 One of the CO_2 microwindows (6310–6380 cm^{-1}) used for TCCON data analysis. The measured spectrum is shown in black, the fitted spectrum in red and the residual in blue. 40

4.2 Second TCCON microwindow (6180–6260 cm^{-1}) of CO_2 used within this work. The measured spectrum is shown in black, the fitted spectrum in red and the residual in blue. 41

4.3 O_2 microwindow (7765–8005 cm^{-1}) used within TCCON as an internal network standard. the measured spectrum is shown in black, the fitted spectrum in red and the residual in blue. 42

4.4 An interferogram of the reference laser. The zero crossings are taken as reference for the measurement-sampling which is ideally symmetric (black arrows). Due to an erroneous determination of the mean intensity level, a zero offset occurs, which gives rise to an asymmetric sampling (red arrows). As a consequence phase ghosts arise, which are superimposed to the spectrum. (Taken from Dohe et al. [2013]) 46

4.5 Schematic illustration of the ghost effect. Occurent ghosts (red) are folded around 15798 cm^{-1}, leading to a ghost spectrum which is the sum of the folded ghosts (blue) and the true spectrum (black). (Taken from Gisi [2012]) 47

5.1 Izaña 125HR time series of daily mean C_{O_2}/p_{gr} from 2007 to 2011 for uncorrected measurements. The beginning of new sub-periods due to instrumental interventions or breakdowns (see Table 5.1) are indicated with red vertical dashed lines. 52

5.2 Izaña 125HR time series of daily mean C_{O_2}/p_{gr} from 2007 to 2011 for uncorrected (black rings) and corrected (red dots) data. After correction, the time series is nearly constant, where C_{O_2}/p_{gr} increased by up to 0.5%. 53

5.3 The opaque region of the solar spectrum between 7290 and 7360 cm^{-1} used in the resampling analysis. The mean intensity in the modulus spectrum is reduced when the ghost correction is applied (black: uncorrected, red: corrected). (Taken from Dohe et al. [2013]) 54

5.4 The mean flux in the (near) opaque spectral region for the spectral window 7290-7360 cm^{-1} as a function of LSE. The scanner velocity of v=40 kHz introduces a significant missampling for forward and reverse scans. (Taken from Dohe et al. [2013]) 55

5.5 Izaña LSE time series from 2008–2011 analyzed using the regions 7290–7360 cm^{-1}(triangles) and 10900-11300 cm^{-1}(squares). Forward (black) and reverse scans (red) vary in magnitude and sign. The beginning of new sub-periods with different LSEs due to instrumental interventions or breakdowns (see Table 5.1) are indicated with vertical dashed lines. (Taken from Dohe et al. [2013]) 58

5.6 Izaña 125HR time series of daily mean X_{air} from 2008 to 2011 for original and resampled measurements. The beginning of new sub-periods with different X_{air} due to instrumental interventions or breakdowns (see Table 5.1) are indicated with vertical dashed lines. (Taken from Dohe et al. [2013]) 59

5.7 Izaña 125HR time series of daily mean X_{CO_2} from 2008 to 2011 for original and resampled measurements. The beginning of new sub-periods due to instrumental interventions or breakdowns (see Table 5.1) are indicated with vertical dashed lines. (Taken from Dohe et al. [2013]) . . . 60

5.8 Lauder 125HR LSE time series determined from resampling analysis of solar interferograms using the 7290-7360 cm^{-1} interval. Instrument changes relevant to the LSE and/or its determination are shown with dashed lines: change from 10 to 20 kHz sample rate for routine acquisition (February 2010), increased phase resolution (April 2010), laser board and diodes exchange (January 2011) and reminimization of laser sampling error at 20 kHz after beam splitter exchange (March 2011). Instrument realignments are shown with dotted lines. (Taken from Dohe et al. [2013]) 62

6.1 Izaña daily mean FTIR X_{CO_2} data (uncorrected: blue, corrected: red) and co-located in situ CO_2 measurements (black) from May 2007 to May 2012. 64

6.2 Correlation plot between daily mean FTIR X_{CO_2} data (uncorrected) and co-located in situ CO_2 measurements at Izaña, where the slope of the regression line represents the bias between FTIR and in situ results. . . 65

6.3 Detrended time series of daily mean FTIR X_{CO_2} data (red) and co-located in situ CO_2 measurements (black) for Izaña from May 2007 to May 2012. 66

6.4 Karlsruhe daily mean FTIR X_{CO_2} data (uncorrected: blue, corrected: red) and simultaneous Schauinsland in situ CO_2 measurements (black) from April 2010 to August 2012. Black rings show CO_2 measurements with coincident large CO concentrations. Common events with unusually large CO_2 amounts are marked green. 67

6.5 Correlation plot between Karlsruhe daily mean FTIR X_{CO_2} data and simultaneous Schauinsland in situ CO_2 measurements, where the slope of the regression line represents the bias between FTIR and in situ results. Black rings represent CO_2 measurements with simultaneously large CO concentrations. 68

6.6 Daily mean FTIR X_{CO_2} data of four European TCCON sites: Bremen (blue), Garmisch (black), Karlsruhe (red) and Orleans (dark cyan) from April 2010 to August 2012 69

7.1 CO_2 total column results for June 4th, 2010 at the Karlsruhe site (7:30 AM to 6:00 PM, SZAs between 27° (noon) and 80°). Original results are illustrated with black dots, whereas results for different applied air-broadening correction factors are shown in different colors. Results determined with the recommended correction factor of 0.97 are illustrated in dark cyan. 72

7.2 CO_2 total column results for June 11th, 2011 at the Izaña site (11:30 AM to 3:30 PM, SZAs between 5° (noon) and 33°). Original results are illustrated with black dots, whereas results determined with the applied air-broadening correction factor of 0.97 are shown in dark cyan. 73

7.3 O_2 total column results for June 4th, 2010 at the Karlsruhe site (7:30 AM to 6:00 PM, SZAs between 27° (noon) and 80°). Original results are illustrated with black dots, whereas results determined with the different applied air-broadening correction factors 1.005 and 0.995 are shown in red and blue. Green dots represent results retrieved with the use of the original GFIT O_2 line list. 74

7.4 O_2 total column results for June 11th, 2011 at the Izaña site (11:30 AM to 3:30 PM, SZAs between 5° (noon) and 33°). Original results are illustrated with black dots, whereas results determined with the different applied air-broadening correction factors 1.005 and 0.995 are shown in red and blue. 75

7.5 Residuals between fit and measurement for the 6310–6380 cm^{-1} microwindow after implementation of line mixing are shown in black for a measurement at Karlsruhe. The red curve represents the difference between fit with LM and fit without LM. 76
7.6 CO_2 total column amounts for June 4th, 2010 at Karlsruhe (7:30 AM–6:30 PM). Results where LM is neglected are shown as red rings, whereas black squares represent results with implemented LM. 77
7.7 O_2 microwindow (7765–8005 cm^{-1}) analyzed with different setups for a measurement at Karlsruhe, where the measured spectrum is shown in black, the fitted spectrum in red and the residual in blue. 79
7.8 O_2 microwindow (7765–8005 cm^{-1}) analyzed with different setups for a measurement at Karlsruhe, where the measured spectrum is shown in black, the fitted spectrum in red and the residual in blue. 80
7.9 Correlation plots between total columns of O_2 including the CIA feature and O_2 total columns without the implementation of CIA for Karlsruhe and Izaña. 81
7.10 Ratio between $Q(T)$ from HITRAN and $Q(T)$ used by PROFFIT against the temperature. The comparison with KOPRA $Q(T)$ is shown in blue, with the more precise 4 parameters setup in red and with the 5 parameters setup in black. 82
7.11 Karlsruhe time series of daily mean X_{CO_2} from April 2010 to March 2011 analyzed with PROFFIT using the KOPRA parametrization of $Q(T)$ (red) and the new 5 parameters setup (blue). Data analyzed with GFIT is illustrated in black. 83
7.12 Correlation diagram between Karlsruhe X_{CO_2} data analyzed with PROFFIT and GFIT. PROFFIT results retrieved with the KOPRA parametrization are shown in red, while results using the new 5 parameters setup are illustrated in black. 84
7.13 Time series of daily mean X_{CO_2} for Karlsruhe from April 2010 to May 2011, where retrievals of PROFFIT using the former PROFFIT a priori profile are shown in red, results of PROFFIT with implemented GFIT a priori profiles in blue and results of GFIT in black. 85
7.14 Correlation diagram between Karlsruhe X_{CO_2} of PROFFIT and GFIT. PROFFIT results retrieved with the former PROFFIT a priori profile are shown in red, while results using GFIT a priori profiles are illustrated in black. 86

7.15 Time series of daily mean X_{CO_2} for Karlsruhe from April 2010 to May 2011, where PROFFIT results using the PROFFIT pT profiles are shown in red, results of the new PROFFIT setup (GFIT pT profiles) in blue and GFIT results in black. 87

7.16 Correlation diagram between Karlsruhe X_{CO_2} of PROFFIT and GFIT. PROFFIT results using the PROFFIT pT profiles are shown in red, while results using the new setup with implemented GFIT pT profiles are illustrated in black. 88

7.17 Karlsruhe time series of daily mean X_{CO_2} from April 2010 to May 2011. PROFFIT retrieval results with the use of the improved solar line list (SL) are shown in blue, results with the use of old line data are shown in red and GFIT results are illustrated in black. 89

7.18 Correlation plot between X_{CO2} values of PROFFIT and GFIT. Retrievals using the old solar line list are shown in red, while results using the improved solar line list are illustrated in black. 90

7.19 Karlsruhe time series of daily mean X_{CO_2} from April 2010 to May 2011. PROFFIT retrieval results including the GFIT O_2 line list (LL) are shown in blue, PROFFIT results using the PROFFIT O_2 line list are shown in red and GFIT results are illustrated in black. 91

7.20 Correlation plot between X_{CO2} values of PROFFIT and GFIT. PROFFIT results using the PROFFIT line list are shown in red, while results using the GFIT O_2 line list are illustrated in black. 92

7.21 Left: Karlsruhe time series of daily mean X_{CO_2} from April 2010 to March 2011 analyzed with PROFFIT and GFIT using the setups of 2011. Right: Correlation plot between X_{CO_2} values of PROFFIT and GFIT (initial status of 2011). 94

7.22 Left: Karlsruhe time series of daily mean X_{CO_2} from April 2010 to May 2012 analyzed with PROFFIT and GFIT using the final setups of 2013. Right: Correlation plot between X_{CO_2} values of PROFFIT and GFIT (status of 2013). 95

7.23 X_{CO_2} total column results for October 10th, 2010 at Karlsruhe (7:30 AM to 4:00 PM). PROFFIT results are illustrated in blue, GFIT results without post processing in red and original GFIT retrievals including post processing in black. 96

7.24 X_{CO_2} total column results for March 22nd, 2011 at Karlsruhe (7:00 AM to 5:00 PM). PROFFIT results are illustrated in blue, GFIT results without post processing in red and original GFIT retrievals including post processing in black. 97

8.1 CO_2 microwindow (4833–4880 cm^{-1}), which is used to retrieve vertical profiles of CO_2 by means of the PROFFIT code. The measured spectrum is shown in black, the fitted spectrum in red and the residual between fit and measurement in blue. 102

8.2 A priori profile of CO_2 which is used within PROFFIT profile retrievals for all measurements. 103

8.3 Typical sensitivities resulting from a measurement analyzed with the described PROFFIT profile retrieval setup. 104

8.4 Daily mean vertical profiles of CO_2 at Izaña from May 2007 to May 2012, determined by use of the described PROFFIT analysis procedure, where the altitude is plotted against the number of measurements since May 2007 and different colors indicate the different CO_2 concentrations. CO_2 minima at the ground in September are labeled with the corresponding years. 105

8.5 Correlation plot between FTIR CO_2 values (ground level) and in situ CO_2 results (black) for Izaña. Additionally the comparison between FTIR X_{CO_2} and in situ CO_2 is shown in red, where the calibration factor of 0.989 is already implemented. 106

8.6 Izaña time series (2007–2012) of daily mean CO_2 from GFIT (X_{CO_2}, red), PROFFIT profile retrieval ground values (black) and in situ measurements (grey). Calibration factors for X_{CO_2} and FTIR CO_2 ground values are already implemented. 107

8.7 Vertical CO_2 profiles for altitudes of 1 to 20 km determined from TCCON spectra (solid lines) and retrieved from aircraft measurements (dashed lines) for five different days (different colors) at Lamont. 108

8.8 Comparison of vertical CO_2 profiles for altitudes of 1 to 20 km from TCCON spectra (solid lines) and smoothed aircraft profiles (dashed lines) for five different days (different colors) at Lamont, where the calibration factor of 1.022 is already implemented in TCCON measurements. . . . 110

8.9 TCCON CO_2 profiles (without calibration factor) for January 30th, 2009 (090130) at Lamont, where the color gradient represents the time of measurement (red=13:45, blue=14:45). The corresponding aircraft measurement is illustrated in black. 111

8.10 CO_2 profiles for 090130 at Lamont retrieved with different ILS settings. The red profile represents the standard setup. Whereas for orange and magenta colored profiles a 5% error in modulation efficiency was induced, the green and blue profiles were retrieved by using a 0.01 rad phase error. The black profile shows the corresponding aircraft measurement. 112

8.11 CO_2 profiles from 090130 at Lamont, analyzed with different deviations ($\pm$1 hPa, $\pm$5 hPa.) from the original NCEP ground pressure value (red). The black profile illustrates the aircraft measurement. 113

8.12 CO_2 profiles from 090130 at Lamont, analyzed with the use of different temperature profiles. The black profile illustrates the aircraft measurement. 114

List of Tables

5.1 The Izaña instrument history with important interventions from January 2005 to November 2010. 51

7.1 The influence of each modification within the PROFFIT setup on the bias and standard deviation between PROFFIT and GFIT X_{CO_2} results. 99

8.1 Number and local times of TCCON measurements which were taken during the corresponding flights. 109

Nomenclature

AEMET Meteorological State Agency of Spain

CarbonSat Carbon Monitoring Satellite

CFCs Chlorofluorocarbons

CIA Collision induced absorption

DFT Discrete Fourier transformation

DIC Dissolved inorganic compounds

DMF Dry air mole fraction

DOF Degree of freedom

FFT Fast Fourier transform

FT Fourier transform

FTIR Fourier transform infrared

FTS Fourier transform spectrometer

FWHM Full width at half maximum

GAW Global Atmospheric Watch

GFIT Software for determination of trace gases out of solar absorption spectra

GHG Greenhouse gas

GOSAT Greenhouse gases Observing Satellite

GPR Ghost-to-parent intensity ratio

HCFCs Hydrochlorofluorocarbons

HeNe Helium-Neon

HFCs Hydrofluorocarbons

HFL High folding limit

HIPPO HIAPER Pole-to-Pole Observations

HITRAN High Resolution Transmission Molecular Absorption Database

ILS Instrumental line shape

IMECC Infrastructure for Measurement of the European Carbon Cycle

IMK Institute of Meteorology and Climate Research

InGaAs Indium Gallium Arsenide

InSb Indium Antimonide

IPCC Intergovernmental Panel on Climate Change

IR Infrared

IRWG Infrared Working Group

KIT Karlsruhe Institute of Technology

KOPRA Karlsruhe Optimized and Precise Radiative transfer Algorithm

LFL Low folding limit

LINEFIT Software for determination of ILS out of gas cell measurements

LM Line mixing

LOS Line-of-sight

LSE Laser sampling error

MIR Mid-infrared

NCEP National Center for Environmental Prediction

NDACC Network for the Detection of Atmospheric Composition Change

NH Northern hemisphere

NIR Near-infrared

NOAA National Oceanic & Atmospheric Administration

OCO II Orbiting Carbon Observatory II

OPD Optical path difference

OPUS Optics User Software

PROFFIT Software for determination of trace gases out of solar absorption spectra

SD Standard deviation

SFIT2 Software for determination of trace gases out of solar absorption spectra

SH Southern hemisphere

SL Solar line list

SZA Solar zenith angle

TCCON Total Carbon Column Observing Network

UV Ultraviolet

VMR Volume mixing ratio

WACCM Whole Atmosphere Community Climate Model

WMO World Meteorological Organization

ZPD Zero path difference

Acknowledgement

Diese Arbeit entstand am Institut für Meteorologie und Klimaforschung des Karlsruher Instituts für Technologie. Ich möchte mich bei allen bedanken, die zum Gelingen dieser Arbeit beigetragen haben.
In erster Linie bedanke ich mich bei Prof. Dr. Matthias Olzmann für die Übernahme des Referats am Institut für Physikalische Chemie und die Unterstützung bei der Anfertigung dieser Arbeit. In gleicher Weise danke ich Prof. Dr. Johannes Orphal für die Übernahme des Korreferats, die fachliche Unterstützung und die interessante Themenstellung.
Mein besonderer Dank gilt Dr. Frank Hase für die engagierte Betreuung, die Bereitschaft Fragen jederzeit geduldig zu beantworten und für die hilfreichen Anmerkungen, die wesentlich zur Fertigstellung dieser Arbeit beigetragen haben. Ich danke Dr. Thomas Blumenstock für die umfassende Unterstützung während der gesamten Promotionszeit und die kritische Durchsicht dieser Arbeit.
Dank gilt der gesamten Boden-Gruppe des IMK für die gute Zusammenarbeit, die angenehme Arbeitsatmosphäre und die interessanten Diskussionen. Besonders danke ich meinen Zimmernachbarn für die netten Gespräche und die tolle Arbeitsatmosphäre.
I also would like to thank my collegues and friends from Tenerife, Eliezer and Omaira for the enriching collaboration and the great time we spent together during conferences and holidays.
I am greatful to the members of the TCCON for their good collaboration. Special thanks to Dr. Vanessa Sherlock for the good collaboration and many helpful discussions concerning the ghost topic. I also would like to acknowledge Dr. Debra Wunch, Prof. Dr. Paul Wennberg, Dr. James Abshire and Prof. Dr. Steven C. Wofsy for providing FTIR spectra and aircraft data from Lamont. Thanks to Martin Kohler for providing tall-tower meteorological data, to Angel J. Gomez-Pelaez, and the team of the station Schauinsland for providing in situ data and to the FTIR groups of the TCCON stations Bremen, Garmisch and Orleans for providing TCCON

data. I would also like to thank the team of the NASA Goddard Automailer for providing temperature and pressure profiles.
Zu guter Letzt danke ich meiner Familie und besonders meinem Freund Bastian für die Unterstützung und Förderung während des gesamten Studiums.